UNCLASSIFIED

SECURITY CLASSIFICATION OF THIS PAGE

REPORT DOCUMENTATION PAGE

AD-A208 664 DTIC ELECTE JUN 06 1989 D

1b. RESTRICTIVE MARKINGS: File Copy (2)

3. DISTRIBUTION/AVAILABILITY OF REPORT: Approved for public release; distribution is unlimited.

4. PERFORMING ORGANIZATION REPORT NUMBER(S)

5. MONITORING ORGANIZATION REPORT NUMBER(S): AFOSR-TR- 89-0710

6a. NAME OF PERFORMING ORGANIZATION	6b. OFFICE SYMBOL (If applicable)	7a. NAME OF MONITORING ORGANIZATION
Univ of Maryland		AFOSR/NP

6c. ADDRESS (City, State, and ZIP Code)	7b. ADDRESS (City, State, and ZIP Code)
College Park, MD 20742	Building 410, Bolling AFB DC 20332-6448

8a. NAME OF FUNDING/SPONSORING ORGANIZATION	8b. OFFICE SYMBOL (If applicable)	9. PROCUREMENT INSTRUMENT IDENTIFICATION NUMBER
AFOSR	NP	AFOSR-86-0046

8c. ADDRESS (City, State, and ZIP Code)	10. SOURCE OF FUNDING NUMBERS			
	PROGRAM ELEMENT NO.	PROJECT NO.	TASK NO.	WORK UNIT ACCESSION NO.
Building 410, Bolling AFB DC 20332-6448	61102F	2301	A8	

11. TITLE (Include Security Classification)
(U) PROPAGATION OF SHORT DURATION, HIGH POWER MICROWAVE PULSES IN NEUTRAL AND IONIZED MEDIA

12. PERSONAL AUTHOR(S)
Dr Destler (William W.) & Dr Striffler (Charles D.)

13a. TYPE OF REPORT	13b. TIME COVERED	14. DATE OF REPORT (Year, Month, Day)	15. PAGE COUNT
Final	FROM 1 Dec 85 TO 30 Nov 88	March 1989	45

16. SUPPLEMENTARY NOTATION

17. COSATI CODES			18. SUBJECT TERMS (Continue on reverse if necessary and identify by block number)
FIELD	GROUP	SUB-GROUP	
	20:03		that

19. ABSTRACT (Continue on reverse if necessary and identify by block number)

Experiments were completed on the propagation of very high power (500 kw/cmsq), short burst (3-30 ms) microwaves through a neutral media. Results indicate the breakdown field strengths are about a factor of two higher when the test cell is shielded from x-rays generated by the microwave source. Standard theoretical models were shown to give very accurate predictions of actual observations for all cases except when the RF frequency was near the plasma frequency. Keywords: Earth Atmosphere; Microwave transmission; Burst transmission; Breakdown electronic threshold; Electromagnetic shielding; Microwave pulses; Large orbit gyrotrons; Plasma physics; Air; (edc)

20. DISTRIBUTION/AVAILABILITY OF ABSTRACT	21. ABSTRACT SECURITY CLASSIFICATION
X ☐ UNCLASSIFIED/UNLIMITED X ☐ SAME AS RPT. ☐ DTIC USERS	UNCLASSIFIED

22a. NAME OF RESPONSIBLE INDIVIDUAL	22b. TELEPHONE (Include Area Code)	22c. OFFICE SYMBOL
R J BARKER	(202) 767-5011	AFOSR/NP

DD FORM 1473, 84 MAR — 83 APR edition may be used until exhausted. All other editions are obsolete.

SECURITY CLASSIFICATION OF THIS PAGE

UNCLASSIFIED

89 6 06 078

Final Technical Report

STUDIES OF THE PROPAGATION OF SHORT BURST, HIGH POWER MICROWAVE RADIATION THROUGH NEUTRAL AND IONIZED MEDIA

Grant No. AFOSR-86-0046

For the Period December 1, 1985 to November 30, 1988

Submitted to

Air Force Office of Scientific Research

Prepared by

Electrical Engineering Department

University of Maryland, College Park, MD 20742

UNIVERSITY OF MARYLAND

LABORATORY FOR PLASMA RESEARCH
COLLEGE PARK, MARYLAND
20742-3511

Final Technical Report

STUDIES OF THE PROPAGATION OF SHORT BURST, HIGH POWER MICROWAVE RADIATION THROUGH NEUTRAL AND IONIZED MEDIA

Grant No. AFOSR-86-0046

For the Period December 1, 1987 to November 30, 1988

Submitted to

Air Force Office of Scientific Research

Prepared by

Electrical Engineering Department

University of Maryland, College Park, MD 20742

Annual Technical Report

Submitted to:	Air Force Office of Scientific Research
Submitted by:	Electrical Engineering Department University of Maryland College Park, Maryland 20742
Grant Number:	AFOSR-86-0046
Period:	December 1, 1987 to November 30, 1988
Principal Investigators:	William W. Destler, Professor Charles D. Striffler, Professor
Title of Research Project:	"Studies of the Propagation of Short Burst, High Power Microwave Radiation through Neutral and Ionized Media."

I. INTRODUCTION

This Technical Report contains a summary of progress made in AFOSR funded studies of short burst microwave propagation through neutral and ionized media over the time period December 1, 1987 to November 30, 1988. Work under this program commenced in December 1985.

The preliminary focus of this work has been the experimental and theoretical study of the ability of very short duration microwave pulses to propagate through the atmosphere without inducing breakdown. Significant progress has been made in this area both in our theoretical understanding of the breakdown process and in actual experimental studies of air breakdown due to short pulse microwaves.

A second project supported under a supplementary grant involves the study of energy recovery in Large Orbit Gyrotrons. In this study, attempts are underway to recover a significant fraction of the energy of the electrons in a Large Orbit Gyrotron after the radiation producing interaction is complete. In this manner, the overall efficiency of such devices could be dramatically increased. Significant new experimental studies of such systems have been completed during the past grant period.

This report is organized as follows: A brief summary of the highlights of these research programs is contained in section II. Copies of papers published during this period are contained in the Appendix.

II. Progress Report for the Period December 1, 1987 to November 30, 1988

A. Experimental Studies of the Propagation of High Power, Short Burst Microwaves Through the Atmosphere

Initial experimental results of the propagation of very high power (1-500 kW/cm^2), short burst (3-30 ns) microwaves through a neutral media were published in the Journal of Applied Physics in a paper ("Short-Pulse, High Power Microwave Propagation in the Atmosphere") enclosed in the Appendix. During the past year, we have conducted additional experiments to determine whether x-rays from the microwave source could be a source of significant free electrons in the test cell and thus result in artificially low breakdown limits. These experiments, in which the test cell was carefully shielded from the microwave source by a concrete and lead shield wall, are summarized in a second paper ("Shielded Source, Short-Pulse Microwave Propagation Experiments") submitted to the Journal of Applied Physics for publication and enclosed in the Appendix. Results indicate that breakdown field strengths are about a factor of two higher when the test cell is shielded from x-rays generated by the microwave source.

B. Theoretical Studies of Short Burst, High Power Microwave Propagation

We have enclosed in the Appendix a copy of the poster presentation at the 1988 APS Plasma Physics Meeting. This work is a summary of the theoretical models and calculations that have been studied under the existing contract. In our initial studies we considered a parameter regime where the ionization of the background gas by the RF is so slow that the ionization rate and RF propagation time scales are very different. In this case we can solve for the electric field via the wave equation for an inhomogeneous time-independent plasma density profile and impose self-consistency with the ionizing electric field. We include besides the ionization process, the attachment and elastic scattering processes for air. The buildup of plasma in a gas cell is calculated along with reflection, absorption, and transmission properties of the incident RF wave. A criteria for defining "breakdown" is presented and results are compared with experiments. The agreement is found to be satisfactory for regimes where the rates of ionization, etc. are valid. These

results have been summarized in previous progress reports.

This past year we have developed a "Medium Ionization Rate Model" for RF propagation through a plasma. In the model we still assume the ionization rate is low compared to the RF frequency but do not require the EM response time of the plasma to be small. That is, finite EM transient time effects are taken into account. For the case when the RF frequency is near the plasma frequency standard methods of calculation are no longer valid. We have developed a power series method about the critical density point. Detailed convergence criteria have been checked and initial results applied to experimental cases are in progress.

C. Studies of Energy Recovery in Large Orbit Gyrotrons

These studies, funded under a supplementary grant from AFOSR, are summarized in two papers enclosed in the Appendix ("Beam Conditioning for Electron Energy Recovery Systems in Devices Employing Axis-Encircling Beams," published in the International Journal of Electronics, and "Study of an Energy Recovery System for a Large Orbit Gyrotron," presented at the 1988 International Electron Devices Meeting). These studies contain the first experimental demonstration of depressed potential collection of rotating beam electrons after their energy has been reconverted to axial motion. The potential of such recovery systems to recover 70–80% of the energy remaining in the electron beam after the rf interaction has been clearly demonstrated in these studies.

APPENDIX

INT. J. ELECTRONICS, 1988, VOL. 65, NO. 3, 351–368

Beam conditioning for electron energy recovery systems in devices employing axis-encircling beams

A. SINGH†, W. LAWSON†, D. GOUTOS†, W. R. HIX†,
C. D. STRIFFLER†, V. L. GRANATSTEIN†
and W. W. DESTLER†

Depressed collectors are extensively used in linear-beam devices. In spiralling beam devices, the motion of the spent beam needs to be converted into axial motion before it can deliver energy to the retarding axial electrostatic field produced by depressed collectors. A method of doing so is presented here, along with simulation results. A large-orbit gyrotron is chosen as an illustrative example in which the axis-encircling beam is generated by passing an axially streaming beam through a magnetic cusp. After rf interaction, an 'unwinding' of the beam is done by a second magnetic cusp with a reversed magnetic field. The trajectories of electrons going through the two cusps have been simulated in order to evaluate the effects of finite cusp width and finite width of emitting surface. Also studied are the effects of variations of the magnetic field, the accelerating voltage of the beam, and the distance between cusps. These simulations show that the rotational energy of electrons is largely converted into axial energy after passage through the second cusp. An initial geometry has been chosen for three collectors, of which two are at depressed potentials. Changes in the energies of the particles are introduced between the two cusps as an approximation of the effect of rf interaction. Simulation of trajectories in the region of the depressed collectors has demonstrated energy sorting of the beamlets to different depressed collectors.

1. Introduction

Gyrotron oscillators operating at the fundamental cyclotron frequency have made great strides in achieving high rf power levels at high frequencies with appreciable efficiencies of operation (Granatstein 1984, 1987, Fix *et al.* 1984, Rager 1986). Other device configurations using spiralling electron beams have unfortunately suffered from significantly lower electronic efficiencies.

Among such devices are those that use axis-encircling beams. These include large-orbit gyrotrons (Lawson *et al.* 1985) and circular geometry free-electron lasers (Befeki *et al.* 1985). Those of the former category of devices, in which the axis-encircling beam is generated by a magnetic cusp, have been referred to as cusptrons (Uhm *et al.* 1984). Those in which the electromagnetic field is supported by a magnetron-like structure have also been called gyromagnetrons (Lau and Barnett 1982, Grow and Shrivastava 1982). The nature of the beam and the rf structure favours the production of coherent radiation at a chosen high harmonic of the cyclotron frequency. As the value of the magnetic field required for any given frequency is reduced in the ratio of the harmonic number, this would be a significant advantage for operation at millimetre wavelengths (Chojnacki *et al.* 1987). However, efficiency usually falls as the harmonic number rises, and this implies that a con-

Received 21 October 1987; accepted 21 December 1987.

† Laboratory for Plasma and Fusion Energy Studies, University of Maryland, College Park, MD 20742-3511, USA.

siderable proportion of the initial kinetic energy of the beam would be carried by the spent beam.

One possibility for improving the overall efficiency of such devices is to recover energy from the spent beam. In the case of linear beam tubes, such as travelling wave tubes, this is a well-accepted approach (Kosmahl 1982, True 1987). The spent beam is sorted into groups energy-wise, and is collected on electrodes at depressed potentials. The geometry and the potentials of the collectors are chosen to make for as soft a landing as possible for each group. Thus, a good fraction of the energy of the beam is transferred back to the power supply system. This has the additional advantage of reducing the bulk and cost of the power supply.

The overall efficiency of the device η_T is related to the intrinsic efficiency η_e and the efficiency of energy recovery η_R by the relationship (Arnush *et al.* 1982)

$$\eta_T = \frac{\eta_e}{1 - \eta_R(1 - \eta_e)}. \tag{1}$$

Thus, if a device of 10% intrinsic efficiency is operated in tandem with depressed collectors at 75% efficiency, the overall efficiency would be 31%.

In the case of devices where the spent beam has most of its energy in rotational motion, the electrons cannot work effectively against the electrostatic field of the depressed collectors. Thus, it is necessary to convert the rotational motion largely into axial motion before leading the beam toward depressed collectors. In linear-beam tubes, transverse motion in the spent beam arising out of the effects of the focusing magnetic field and rf interaction is partially converted into axial motion by an adiabatic expansion of the beam (Kosmahl 1982). In the case of axis-encircling beams, the Larmor radius of the beam electrons is usually large, and would be further increased by adiabatic expansion before the process of energy sorting starts. The latter process itself involves further radial expansion and an increase of the aperture of each of successive depressed collectors. Thus, adiabatic expansion, apart from requiring a slow change of magnetic field over a distance, involves considerable enlargement of the dimensions of axis-encircling beam devices.

We have proposed 'unwinding' the beam by passing it through a second cusp with a reversed magnetic field. Its radial magnetic field component acts on the azimuthal component of velocity and converts it largely into axial velocity; this is a non-adiabatic process. As shown by these studies, a substantial fraction of the energy in the rotational motion of the electrons is reconverted into axial motion in a distance that is small compared with the pitch of the spiralling motion and with little change in the diameter of a hollow beam.

The extent of this reconversion is dependent upon various parameters. We have studied the reconversion phenomenon as a function of the transition widths of two cusps, the distance been them, the radial width of the beam, the magnetic field amplitude, and the accelerating voltage of the beam. A single particle code was used to plot the trajectories. The results of these simulations are presented here. They verify the applicability of the basic approach in that the fraction of energy converted into axial motion is close to 90% even with a non-optimum combination of parameters.

We have also simulated the trajectories of particles with different energies in the region of the depressed collectors. For this purpose a system of three collectors, two of which are at depressed potentials, is chosen as an initial example. Energy sorting under the combined action of the magnetic and electrostatic fields is demonstrated.

In §2, the results of computer simulations relating to the unwinding of a spiralling, large-orbit beam by a second cusp under various conditions are reported. Section 3 presents the trajectories in the collector region and verifies energy sorting. Section 4 outlines the design considerations in the planned experiment, and conclusions are drawn in §5.

2. Generation and unwinding of spiralling electron beams

An axis-encircling beam for a large orbit gyrotron can be generated by passing an axially streaming beam through a magnetic cusp, which has a sharp reversal of magnetic field (Rhee and Destler 1974). The behaviour of an electron beam passing through such a cusp has been studied in the cases of an ideal cusp as well as a cusp with a finite transition width (Scheitrum and True 1981, Rhee and Destler 1974). The cases studied include a balanced cusp, which implies an exact reversal of the field on the two sides of the cusp, as well as more generalized changes of field across the cusp (Destler and Rhee 1977).

A solution of the equations of motion shows that for a spiralling electron passing through an ideal cusp, the guiding centre radius upstream equals the Larmor radius downstream (Rhee and Destler 1974). As a special case we note that an electron travelling axially at a radius r_0 through an ideal and balanced cusp acquires a spiralling motion, whose guiding centre lies on the axis and whose Larmor radius equals r_0. An annular sheet beam of radius r_0 correspondingly emerges as a uniform rotating cylinder. Considering the case of two ideal cusps separated by a certain distance, the electron would have a zero Larmor radius beyond the second cusp and a guiding centre radius of r_0, i.e., an axially-streaming beam.

A schematic diagram of a configuration which is the subject of study here is shown in Fig. 1. A stream of electrons starts from a ring cathode and is formed by a Pierce gun into an axially-streaming annular beam. After passing the first cusp, the beam passes through a region which has an rf structure. The beam then goes through the second cusp (that has a reversed field), which tends to unwind the spiralling motion before the beam proceeds toward the depressed collectors.

In practice, the transition region in the cusps has a finite width. An approximation to the field variation across the cusp which has been used with success is as follows (Destler *et al.* 1988, Lawson and Latham 1987):

$$B_z(r_0, z) = B_0 \tanh \frac{z}{\zeta} \tag{2}$$

where B_0 is the asymptotic magnitude of the axial magnetic field on the two sides of a balanced cusp, and ζ is a parameter that is the measure of the transition width along the z-axis. In this case, the guiding centre downstream of the cusp no longer lies on the axis. Considering all electrons in a thin hollow beam starting at a given radius, the finite cusp width gives rise to a scalloping of the post cusp beam envelope. The scalloping wavelength to zeroth-order is given by

$$\lambda = 2\pi r_0(\eta^2 - 1)^{1/2} \tag{3}$$

which is the electron axial pitch distance for an ideal cusp; and where $\eta \triangleq v_{z_i}/r_0\Omega$; v_{z_i} is the axial velocity upstream of the cusp, $\Omega = eB_0/m\gamma$ is the relativistic cyclotron frequency, and γ is the relativistic mass factor.

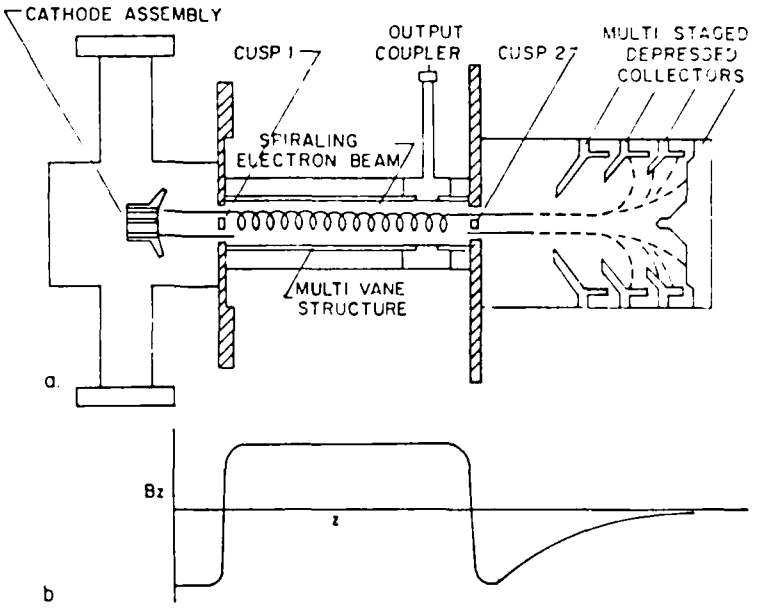

Figure 1. Schematic diagram of a configuration which is the subject of study here. A stream of electrons starts from a ring cathode and is formed by a Pierce gun into an axially-streaming annular beam. After passing the first cusp, which causes the beam to spiral, the beam passes through a region which has an rf structure. The beam then goes through the second cusp (that has a reversed field), which tends to unwind the spiralling motion before the beam proceeds towards the depressed collectors.

For this study, a parameter which acts as a useful index of the effects of the two cusps is α, defined as the ratio of the transverse to the axial component of velocity, i.e.,

$$\alpha \triangleq \frac{v_\perp}{v_\parallel} \tag{4}$$

In order to obtain some figures for a typical set of operating parameters and to gain a better insight into their interrelationships, trajectories were simulated under different conditions. A single particle code was used for tracing the path of the electrons through the cusped magnetic fields. The code numerically integrates particle orbits through the cusp fields. The code uses, as a model for the cusp, the axial component of the magnetic field as given in eqn. (2). A gaussian profile is used for the radial component of the field and a Taylor expansion of the fields about $r = r_0$ is performed. See Destler *et al.* (1988) and Lawson and Latham (1987) for more details on the code. The initial values of the static parameters were close to the experimental values for the low energy cusptron operated earlier at the University of Maryland. These were: $B_0 = 328{\cdot}8$ gauss, $r_0 = 1{\cdot}5$ cm, accelerating voltage $V_0 = 26$ kV, and $\zeta = 4$ mm.

From such a simulation, an illustrative example of the variation of α with the axial position is shown in Fig. 2. The value of α goes from zero upstream of the cusp to a finite value in the region between the cusps, denoted by α_{midrange}. It falls to a low value as the beam passes through the second cusp, denoted by α_{residual}. As the

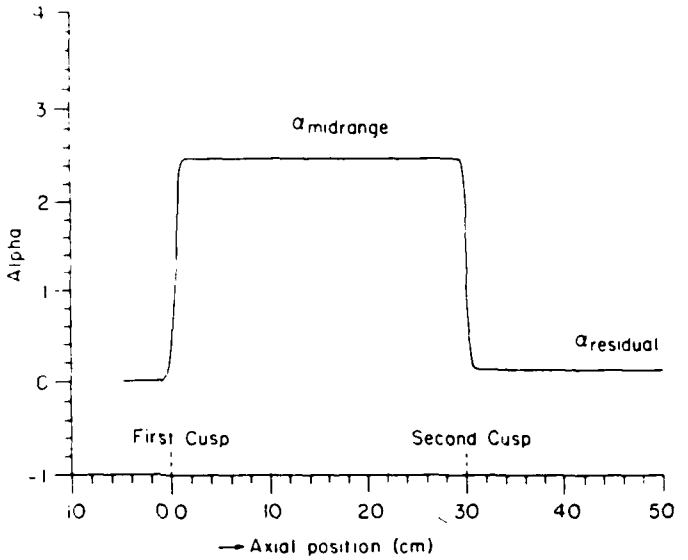

Figure 2. Illustrative example of the variation of $\alpha = v_\perp/v_\parallel$ along the axial coordinate. It rises from zero to a value called $\alpha_{midrange}$ as the electrons pass the first cusp, located at 0 cm, and falls again to a low value called $\alpha_{residual}$ after the electrons pass the second cusp, located at 30 cm: $B_0 = 340$ gauss, $r_{start} = 1{\cdot}5$ cm, $\zeta_{1,2} = 4$ mm, and $V_0 = 26$ kV.

cusps have a finite width, the value of $\alpha_{residual}$ turns out to be finite rather than zero as in the ideal cusp limit.

Various geometric and electrical parameters influence the trajectories, $\alpha_{midrange}$ as well as $\alpha_{residual}$. These were studied by varying the parameters one by one. The results are reported in the following subsections.

2.1. *Variation of* α *with* $\mathbf{B}_0$

For the case of the ideal cusp where the transverse velocity component is purely azimuthal, the value of $\alpha_{midrange}$ is given by:

$$\alpha_{midrange} = \frac{r_0 \Omega}{[v_{z_1}^2 - (r_0 \Omega)^2]^{1/2}} \tag{5}$$

The results of particle code simulations performed to determine the effect of variations of B_0 are summarized in Fig. 3(*a*). As seen from eqn. (5), $\alpha_{midrange}$ is a monotonically rising function of B_0. It is also seen that $\alpha_{residual}$ goes through a cyclic variation. This variation is associated with the radial scalloping of the electrons between the two cusps and the resulting variation in particle angle as it enters the second cusp. The physical explanation of this and cyclic variations with other parameters are discussed in §2.6. Here it may be noted that as B_0 increases, the cyclic variation occurs at shorter intervals, due to a progressive decrease in the scalloping wavelength.

As a general trend, the value of $\alpha_{residual}$ is less than $\alpha_{midrange}$ by a factor of ten or more. The maximum value of $\alpha_{residual}$ is mostly below 0·3. Consequently, the energy in rotational motion is less than 10% of the energy in axial motion.

For most of the other simulation runs, the distance between the two cusps, z_{c_2},

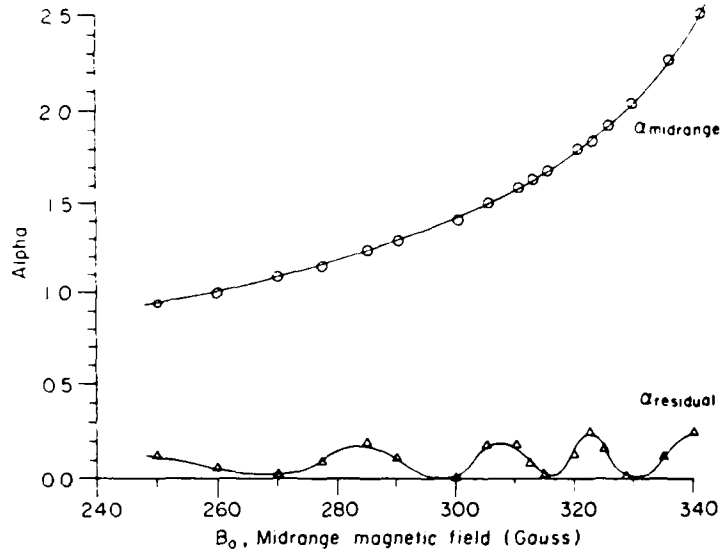
2.5
2.0
1.5
1.0
0.5
0.0
Alpha
$\alpha_{midrange}$
$\alpha_{residual}$
240
260
280
300
320
340
B_0, Midrange magnetic field (Gauss)

(*a*)

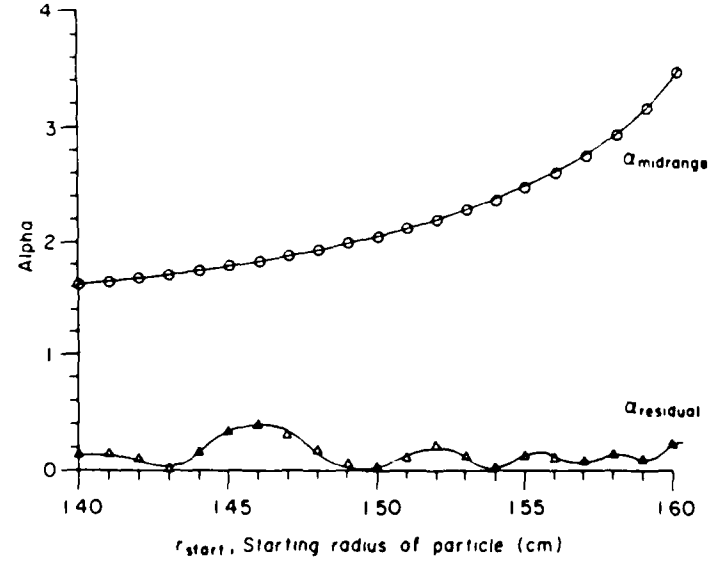
4
3
2
1
0
Alpha
$\alpha_{midrange}$
$\alpha_{residual}$
140
145
150
155
160
r_{start}, Starting radius of particle (cm)

(*b*)

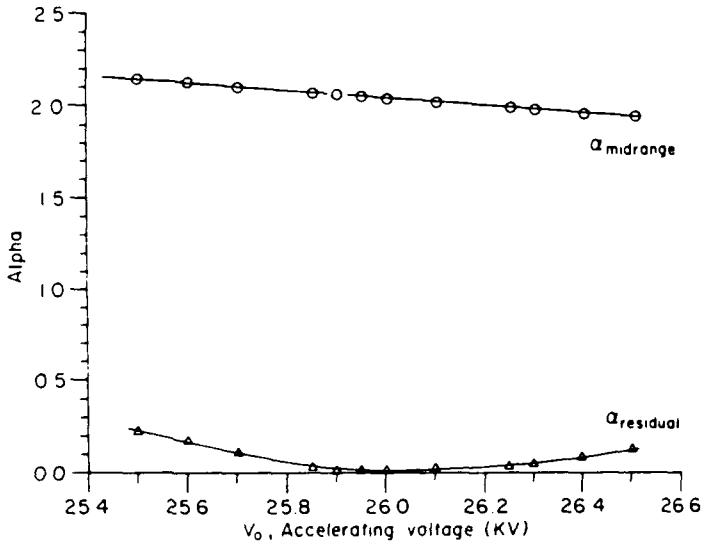

(*c*)

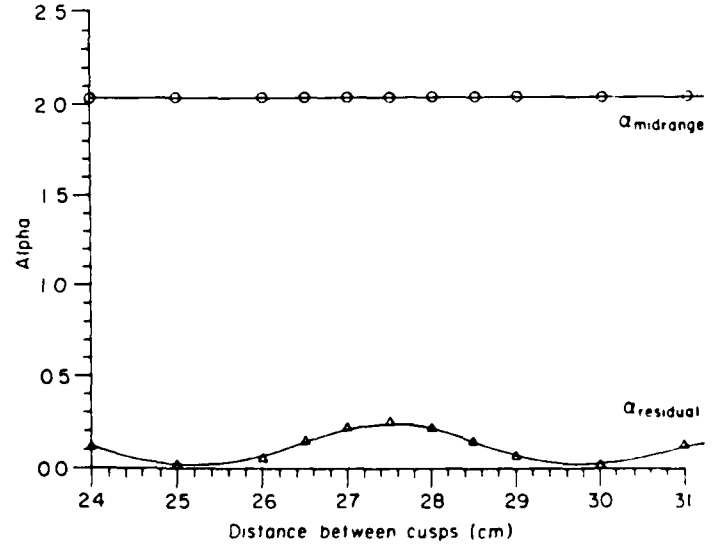

(*d*)

Figure 3. Results of particle code simulations relating to the effect of variations in different parameters on $\alpha_{midrange}$ and $\alpha_{residual}$. Median values of the parameters are: $V_0 = 26\,kV$, second cusp at 30 cm, $r_{start} = 1{\cdot}5\,cm$, $\zeta_{1,2} = 4\,mm$, and $B_0 = 328{\cdot}8$ gauss. (*a*) Effect of variation of B_0; (*b*) effect of variation of r_{start}, the starting radius of the particle; (*c*) effect of variation of V_0, the accelerating voltage; and (*d*) effect of variation of distance between cusps.

was chosen as 30 cm. For this value of separation and $B_0 = 328{\cdot}8$ gauss, the value of $\alpha_{residual}$ was 0·014. Clearly, this is the optimum position to produce low transverse energy, and thus increased depressed collector efficiency. This is subject to a narrow range of variation of the starting radius, as discussed in the next section.

2.2. *Variation of α's with starting position of electrons*

For a given value of B_0, the radius at which the electron starts, denoted by r_{start}, influences $v_\perp$, $v_\parallel$, and α. For an annular cathode with finite width, the value of $\alpha_{midrange}$ would thus depend upon the starting position of the electron (substitution of r_{start} for r_0 in eqn. (5)). For this reason, it is advisable to limit the percentage of variation in r_{start} to a small value. Also, the choice of value of B_0 should not be too close to the threshold value of the magnetic field for which the particles reflect (Rhee and Destler 1974), for otherwise the variations in α due to the variation in r_{start} will be too large.

Figure 3(*b*) shows the variations of $\alpha_{midrange}$ and $\alpha_{residual}$ with the starting positions of the particle. As expected, $\alpha_{midrange}$ rises monotonically with r_{start}. Furthermore, the value of $\alpha_{residual}$ varies cyclically with r_{start}. Recall that as $\alpha_{midrange}$ changes, the number of gyrations completed between the two cusps changes. Because of the finite width of the cusps, the beam would have a scalloping motion whose phase of arrival at the second cusp would depend upon r_{start}, resulting in the cyclic variation of $\alpha_{residual}$.

The highest value of $\alpha_{residual}$, corresponding to $r_{start} = 1{\cdot}46$ cm, is 0·37. For the range of values of r_{start} for the actual cathode, from 1·4–1·6 cm, the $\alpha_{residual}$ lies for the most part between 0·01 and 0·2, indicating a good percentage of energy conversion from rotational to axial motion. It is observed that if the distance between the cusps is changed, the value of r_{start} for the maximum value of $\alpha_{residual}$ is also altered.

2.3. *Variations of α's with accelerating voltage*

Trajectory simulations were done for a narrow range of accelerating voltages, V_0, from 25·5–26·5 kV. As seen in Fig. 3(*c*), $\alpha_{midrange}$ decreases slowly from 2·15 to 1·94, while $\alpha_{residual}$ rises from 0·005 at the median value of V_0 to 0·225 and 0·122 at the two extremes. These changes are due to variation from optimum in the phase of scalloping at the second cusp.

2.4. *Variation of $\alpha_{residual}$ with distance between the cusps*

As expected, the $\alpha_{midrange}$ is dependent upon the electrical parameters and those of the first cusp only. Figure 3(*d*) shows the variation of $\alpha_{residual}$ with the location of the second cusp with respect to the first one. It is seen that the variation is cyclic between the values 0·014 and 0·250. These values are satisfactory from the point of view of energy conversion. The cyclic nature of the variation is discussed in section 2.6.

2.5. *Variation of $\alpha_{residual}$ with transition width of the cusps*

As the cusp half-width, ζ, was varied from 2·0–5·0 mm for both cusps, the $\alpha_{midrange}$ simultaneously increased slowly from 2·02–2·06, and the $\alpha_{residual}$ decreased

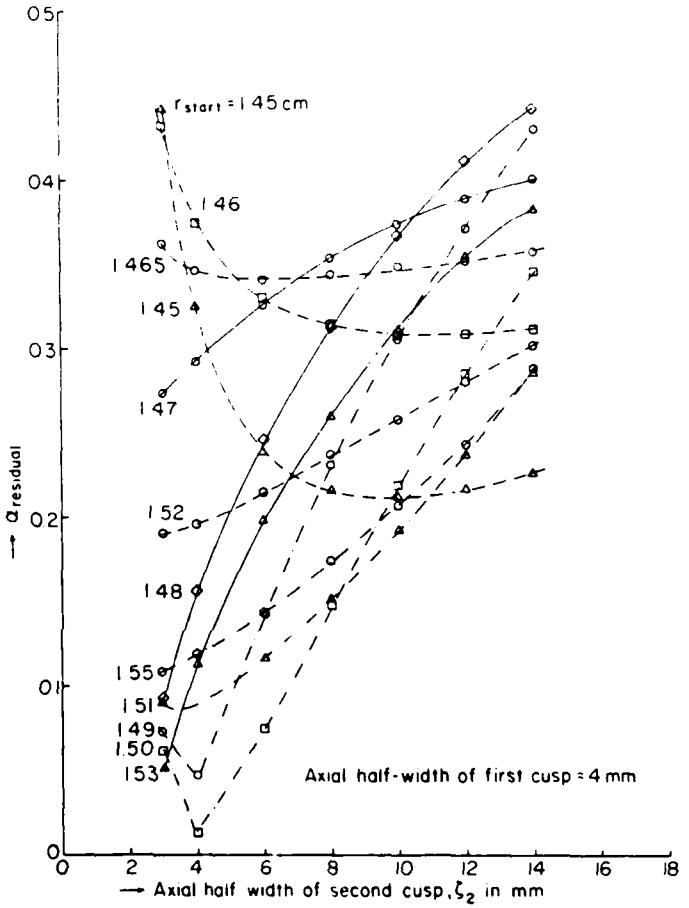

Figure 4. Plots showing variations of $\alpha_{residual}$ with ζ_2 the half-width of the second cusp going from 3–14 mm. The parameter ζ_1, the half-width of the first cusp, equals 4 mm.

slowly from 0·029–0·006. Thus, although an increase in the cusp width increases the shift of the guiding centre from the axis, thus increasing the scalloping; the changes in α are small. The values of $v_\perp$ and $v_{||}$ depend essentially on B_0. The trajectories, however, are influenced by the modelling of the field in the transition region. The model tends to be less accurate as one moves away from the median value of r_{start} and near to the corners of the iron cusp material.

Furthermore, the value of $\alpha_{residual}$ was determined for r_{start} = 1·46 cm (the worst case defined in §2.2), as well as for other values of r_{start} for a variation of ζ of the second cusp from 3–14 mm, keeping ζ for the first cusp equal to 4 mm, as shown in Fig. 4.

It is seen that for starting radii such as 1·45 cm, which give a relatively high $\alpha_{residual}$ at ζ_2 = 3 mm, the $\alpha_{residual}$ diminishes as ζ_2 increases and goes through a broad minimum near ζ_2 = 10 mm. For starting radii such as 1·50 cm, which gives a very low value of $\alpha_{residual}$ for ζ_2 = 3 mm, the $\alpha_{residual}$ has a sharp minimum at ζ_2 = 4 mm and progressively rises as ζ_2 increases further to 14 mm.

The maximum swing in $\alpha_{residual}$ with variation in r_{start} is by a factor of nearly 40,

when both ζ_1 and ζ_2 are 4 mm. However, this factor is only two when ζ_2 has risen to 14 mm. Broadly speaking, this phenomenon can be understood as follows. Changes in $\alpha_{residual}$ occur due to variations in r_{start}, because the latter changes the phase of scalloping in which the particle enters the second cusp. If the second cusp is narrow, the phase relationship is sharply defined, resulting in clear-cut reinforcement or cancellation of the radial component of velocity due to the two cusps. When the two cusps are narrow and of equal width, the cancellation can be nearly complete, at a favourable phase relationship. However, when the second cusp is broad, there is a correspondingly large change in the phase of scalloping during transit through the cusp. Consequently, reinforcement or cancellation is not very sharply defined. The general trend is for $\alpha_{residual}$ to increase as ζ_2 rises.

2.6. *Cause of cyclic variations in* $\alpha_{residual}$

The solution of the equations of motion shows that for the case of a finite transition width of a cusp, the charged particle acquires a positive radial component of velocity as it passes through the cusp. This, in fact, causes a shift in the positions of the guiding centre away from the axis and results in scalloping.

When the particle approaches the second cusp, its scalloping motion may have given it a positive or negative component of radial velocity, depending on its phase in the scalloping cycle. If the particle is moving outward as it approaches the second cusp, the radial motion is accentuated, thus giving rise to a relatively larger value of $\alpha_{residual}$. The reverse is true for the case of the particle approaching the second cusp with an inward motion, which then wholly or partly is compensated for by the effect of the second cusp.

In this connection, it is relevant to look at the trajectories of the particles from an end on position. Figure 5 shows such a projection in the x-y plane for two

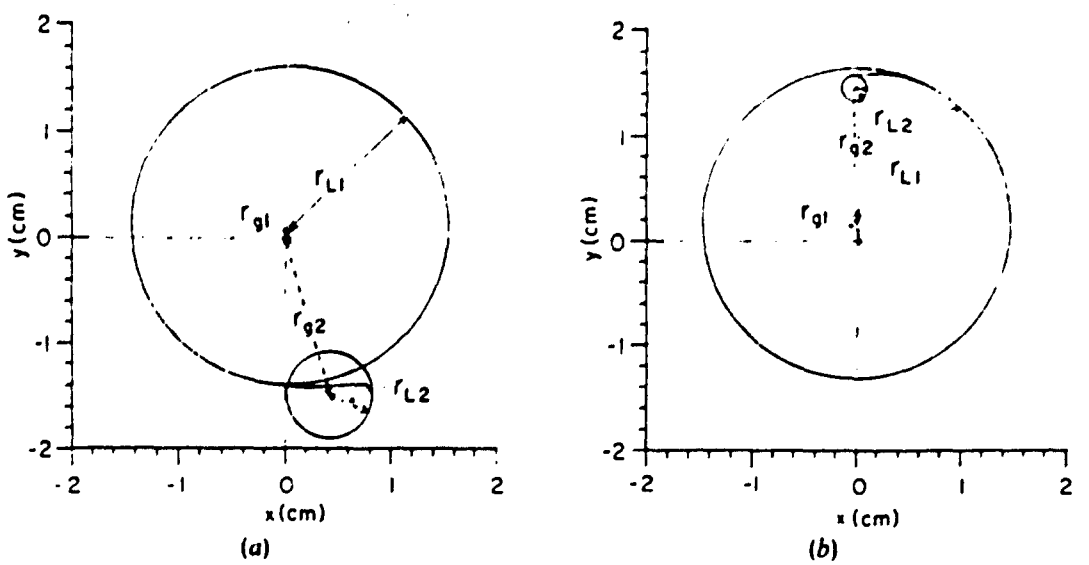

Figure 5. Trajectories of the particles as seen from an end-on position showing a projection in the transverse (x-y) plane for two particles. In each case, the larger circle represents an end-on view of the spiralling motion in the midrange region (subscript 1), and the smaller circle represents the residual spiralling motion beyond the second cusp (subscript 2). In (*a*) the particle is going outward as it goes through the second cusp, and the circle showing residual motion is larger than the case (*b*) where the particle is going inward as it enters the second cusp.

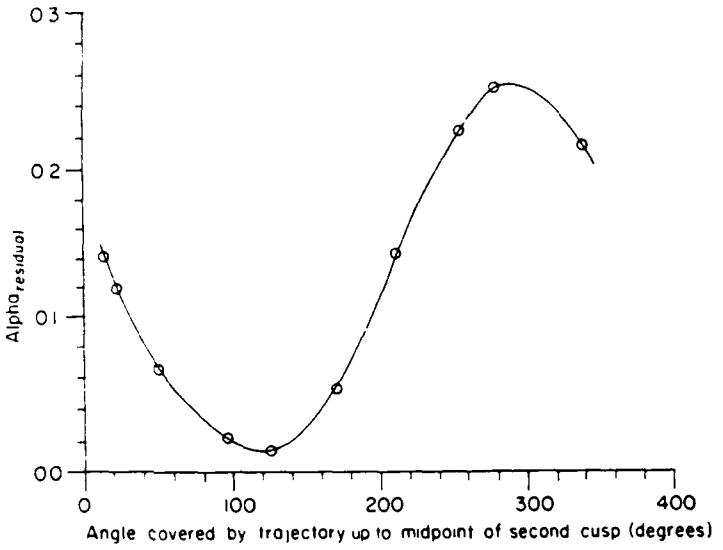

Figure 6. Plots of the value of the $\alpha_{residual}$ versus the transit angle, over and above complete cycles for the case where the change in the transit angle is due to the change in location of the second cusp. The points represent snapshots which do not all belong to one and the same cycle. $V_0 = 26\,kV$, second cusp at 30 cm, $r_{start} = 1{\cdot}5\,cm$, $\zeta_{1,2} = 4\,mm$, and $B_0 = 328{\cdot}8$ gauss.

particles. In each case, the larger circle represents an end-on view of the spiralling motion in the midrange region with a larger Larmor radius. The smaller circle represents the residual spiralling motion beyond the second cusp, which has a smaller Larmor radius. This second circle is seen to have a larger diameter in Fig. 5(*a*) when the particle is moving outward from the larger to the smaller circle than in Fig. 5(*b*), where the trace connecting the two is moving inward. The off-axis locations of the guiding centre are clearly seen.

The value of $\alpha_{residual}$ versus the transit angle (modulo 2π) was plotted for the case when the change in the transit angle is due to the change in location of the second cusp and is shown in Fig. 6. The one cycle shown is, in fact, a synthesis of snapshots of points occurring over more than one cycle seen in Fig. 3(*d*). A similar curve was obtained when the change in transit angle was due to a change in the magnetic field, B_0, while keeping the distance between the cusps constant. This corroborates the physical explanation of the cause of the cyclic variations discussed above.

Correlation between transit angle and $\alpha_{residual}$ was also seen to be good in the case of variations due to a change in ζ. However, the scatter of points was larger in the case of variations caused by changes in r_{start}. This is attributed to the fact that when r_{start} is changed, it changes not only the $\alpha_{midrange}$ and the scalloping wavelengths but also shifts the trajectories farther away from the median radius of the hollow beam. In that case, the field profiles and the effective cusp width vary. The $\alpha_{residual}$ changes cyclically with transit angle but not on an equally smooth curve.

2.7. *Variation in the range of scalloping*

The range of scalloping, as defined by the difference between the maximum and minimum radii of the trajectories, was studied in the region between the cusps and

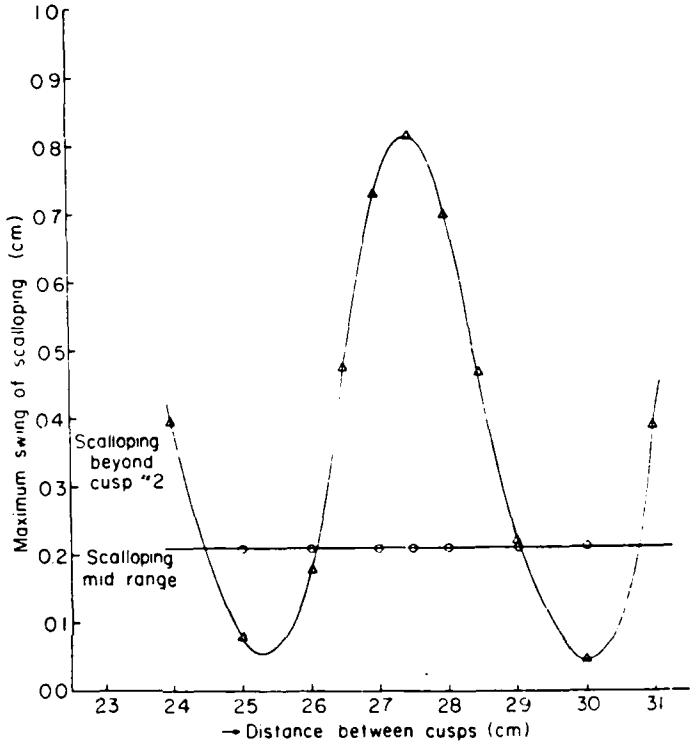

Figure 7. The range of scalloping, as defined by the difference between the maximum and minimum radii of the trajectories in the region between the cusps and beyond the second cusp. Shown is the case of variations due to distance between cusps, B_0 = 328·8 gauss, r_{start} = 1·5 cm, V_0 = 26 kV, and $\zeta_{1,2}$ = 4 mm.

beyond the second cusp. Figure 7 shows the case of variations in the range scalloping due to variation in the distance between the cusps. The cyclic variations in scalloping beyond the second cusp are seen to resemble the variations in $\alpha_{residual}$. The scalloping in the midrange region is, of course, dependent only on the parameters of the first cusp, and is therefore not a function of the distance between cusps.

2.8. *Correlation between analytical and numerical results*

The parameters $\lambda_{scalloping}$ and $\alpha_{midrange}$ can be evaluated both from numerical simulations and the analytical relationships given in eqns. (3) and (5). The results for $\alpha_{midrange}$ are shown in Figs. 8(*a*) and (*b*) and agree very closely. When the independent variable is B_0, the difference is 0·4% for B_0 = 260 gauss and 1% for B_0 = 340 gauss, with the respective values of α being 1·0 and 2·5. Where the independent variable is r_{start}, the difference is 0·4% for the median value of r_{start} and rises to 6% for r_{start} = 1·4 and 1·6 cm. Plots of the numerical and analytical values of $\lambda_{scallop}$ as a function of the starting radius are shown in Fig. 9. The difference varies from 2% near the median value of r_{start} to 6% at r_{start} = 1·6 cm. These differences are due to a combination of finite mean cusp width and variation of cusp width about the mean value.

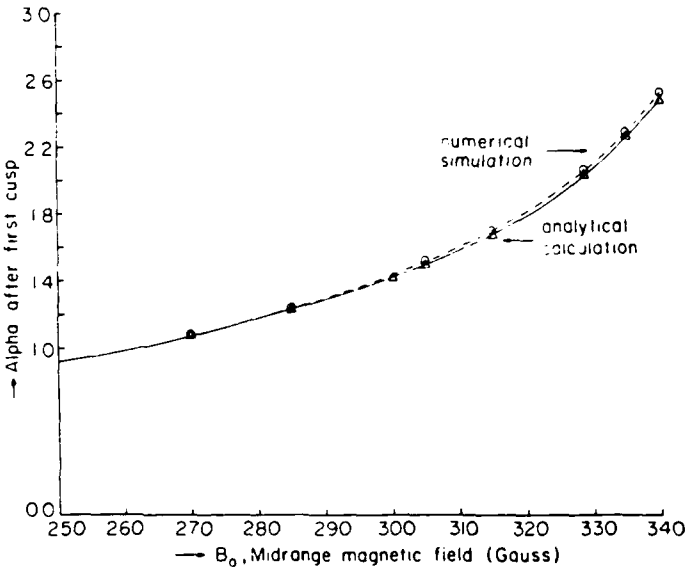

(*a*)

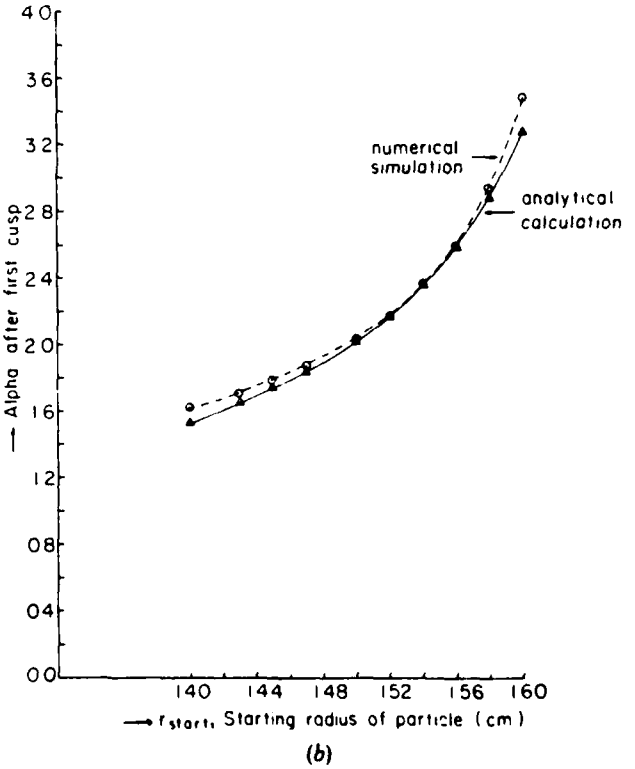

(*b*)

Figure 8. A comparison of values of $\alpha_{midrange}$ obtained from analytical and numerical techniques. (*a*) Variation of α with B_0. The difference is 0·4% at $B_0 = 260$ gauss and 1% at $B_0 = 340$ gauss; $V_0 = 26\,kV$, $r_{start} = 1{\cdot}5\,cm$, and $\zeta_1 = 4\,mm$. (*b*) Variation of α with r_{start}. The difference is 0·4% at $r_{start} = 1{\cdot}52\,cm$ and 6% at 1·40 and 1·60 cm: $B_0 = 328{\cdot}8$ gauss, $\zeta_{1,2} = 4\,mm$, and $V_0 = 26\,kV$.

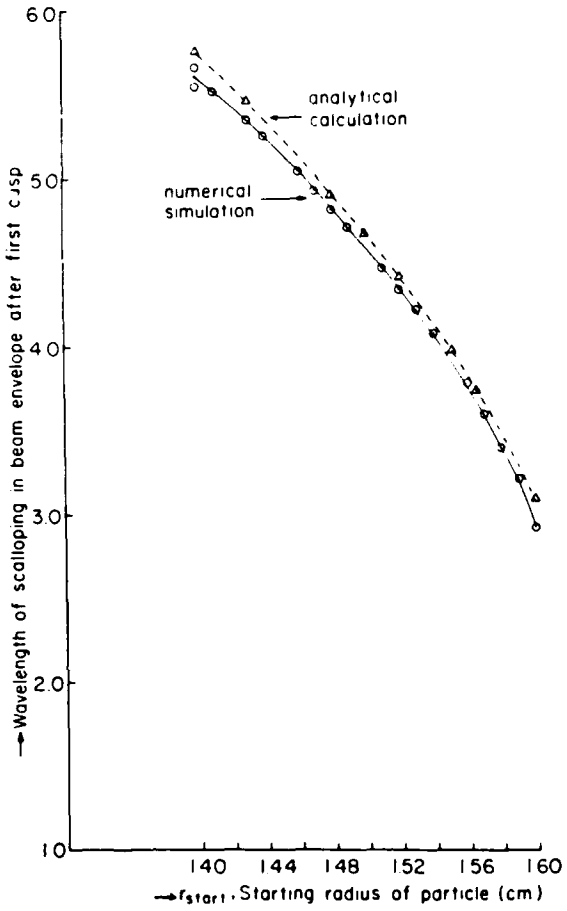

Figure 9. A comparison of the values of scalloping wavelength versus starting radius of the particle as obtained from analytical and numerical techniques. The difference varies between 2% and 6%. $B_0 = 328{\cdot}8$ gauss, $V_0 = 26$ kV, and $\zeta_1 = 4$ mm.

3. Energy sorting in the collector region

With its rotational motion converted sufficiently into axial motion, the beam would be ready to enter the region of depressed collectors. The geometry and the potentials in the collectors, as well as the magnetic field profile, have to be suitably chosen. The objective is that the combined effect of this electrostatic field and the magnetic field cause the trajectories of electrons of different energy ranges to be sorted out to different electrodes with depressed potentials as close to the energy of that group as possible. The larger the energy spread due to rf interaction and the more ambitious the target value for collector efficiency, the larger the number of depressed collectors that would be required.

In the present case, considering the fact that a large-orbit gyrotron operating in a high harmonic mode has a low efficiency, a configuration was chosen consisting of three collectors, two of which are at depressed potentials. In choosing the geometry, a consideration kept in mind is that a small component of radial electric field is

introduced in the collector region which opposes the motion of any secondary electrons emitted at the collector surfaces back toward the axis.

The Herrmannsfeldt code (Herrmannsfeldt 1979) has been used for calculating the trajectories of the particles. The magnetic field profile is also evaluated by specifying the position, the geometry, and the current through each ideal N-turn coil. The effect of the iron plate that generates the second cusp was simulated by an image of the coil nearest to the iron plate.

The potentials on the depressed collectors, as well as the parameters of the coils, were adjusted for suitable energy sorting. The electrode potentials were set at 0, $-12{\cdot}5$, and -20 kV. The magnetic field was always adjusted to make it a balanced cusp.

In fixing the parameters for trajectory studies, the energy of the electron beam entering the first cusp was initially assumed to be 26 keV, corresponding to an earlier experiment on cusptron operation at the University of Maryland (Chojnacki *et al.* 1987). In order to simulate the conversion of a part of the energy in the beam into rf in the region between the cusps, the particles were divided into five groups. Energy changes were introduced to correspond to -30%, -20%, -10%, 0%, and $+10\%$ of 26 keV. The radial location at which the particles emerged from the second cusp, as well as their angles, were noted from single particle trajectory code simulation. These were then used as inputs to the Herrmannsfeldt code simulation of trajectories in the collector region. The trajectories are shown in Fig. 10. The beam current was assumed to be one ampere, as in the earlier experiment.

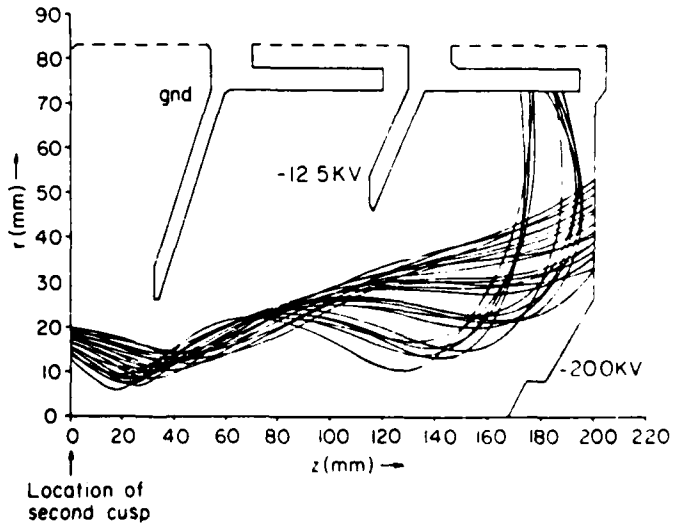

Figure 10. Electron trajectories in the collector region for electrodes at ground, $-12{\cdot}5$ kV, and -20 kV. The beamlets of energies 18·2 and 20·8 keV are collected at $-12{\cdot}5$ kV; those of energies 23·4, 26·0, and 28·6 keV are collected at -20 kV.

It is seen that the beamlets of energies 18·2 and 20·8 keV are collected at the electrode at −12·5 kV, and those of energies 23·4, 26·0 and 28·6 keV are collected at the electrode at −20 kV. These results show energy sorting in the collector region with two depressed collectors for a case of small spread in energy, arising out of relatively low electronic efficiency.

For larger electronic efficiency, it would be necessary to include a more precise model of the energy spread in the beam arising out of the rf interaction. A larger number of depressed collectors would also be desirable for the case where electronic efficiency is high.

Furthermore, trajectory simulation for 14·5 keV shows a tendency for some electrons to be reflected before touching the −12·5 kV electrode. This indicates a residual rotational energy of 2 keV for some electrons. This phenomenon is minimized by suitable profiling of the magnetic and electrostatic fields. It also points up the benefit accruing from the transformation from rotational to axial motion, failing which, for example, the collection of the 23·4 keV electrons on the −20 kV electrode would not have been possible.

Since the value of the axial magnetic field is reduced as the beam proceeds farther into the collector region, a further conversion of the rotational motion into axial motion occurs. The reduction in magnetic field here need not be slow enough to qualify for being called adiabatic.

For comparison, it may be noted that if the reduction in α were to be obtained purely by adiabatic change of magnetic field, then

$$\alpha = [(\alpha_0^{-2} + 1)f_m - 1]^{-1/2} \tag{6}$$

where α_0 and α represent the ratio of transverse to axial velocity before and after the adiabatic change, and f_m is the ratio of initial to final value of the magnetic field. Correspondingly, the Larmor radius of the orbit increases by a factor of $\sqrt{f_m}$. For instance, starting with $\alpha_0 = 2$, an adiabatic reduction of magnetic field by a factor of nine would reduce α to 0·312 and increase the Larmor radius of the orbit by a factor of three.

These considerations can be used in designing any particular system, depending upon the nature of the device and the requirements as well as the space that could be made available in the radial and axial directions in the collector region.

4. Design considerations for the experiment

The computer simulation results described in the previous sections are used to provide guidelines for the design of the experiment. These guidelines are listed below. Recall that there are limitations in the modelling of the axial magnetic field at the beam radius by the function $\tanh z/\zeta$, especially as the particles travel to radii that are well-removed from the median radius of the beam.

1. As α is a function of starting radius, the range of variation of the latter is to be restricted (e.g. to 5%). Too large a spread in α_{midrange} would reduce the efficiency of rf interaction. Furthermore, if r_{start} has a narrow range, then the other parameters, such as B_0, V_0, and the location of the second cusp, can be fine tuned so that the α_{residual} is low for all the trajectories. However, as the range of r_{start} becomes narrower, the cathode current density for a given beam current would become higher; and thus become a limiting factor.

2. In order to minimize scalloping after passage through the first cusp, its transition width is to be minimized. The limiting factor would be the saturation flux of the material used. Presently ζ_1 is set at 4 mm, keeping the existing cusp number one as a starting point (Chojnacki *et al.* 1987).
3. The median values of other parameters are chosen so that the beam is scalloping inward as it enters the second cusp, minimizing $\alpha_{residual}$.
4. The choice of the width of the second cusp is a design compromise. When the starting radius of the particles is restricted to a range less than 5% and the other parameters finely tuned, the minimum residual energy in the beam as a whole, associated with transverse motion beyond the second cusp, occurs when the two cusps are of comparable width. Increase of the width of the second cusp increases the residual energy by a few percentage points. However, this gives the advantage of an increased radial gap available for the beam to pass through. In this case, a cusp half width of 6 mm has been chosen.
5. The magnetic field profile, the electrode shapes, and their potentials are tailored to give optimum energy sorting between electrodes and soft landing of electrons with minimum residual energy.
6. The range of collection of electrons from 18·2–21 keV on the $-12{\cdot}5$ kV electrode and 22–28 keV on the -20 kV electrode is adequate for a device of electronic efficiency ≈ 10–15%. Such a typically low electronic efficiency for harmonic operation does not cause a large spread in the energies.

We are working toward an experimental confirmation of these ideas. We are also considering geometries involving larger numbers of depressed collectors.

5. Conclusions

The overall efficiency of devices employing spiralling electron beams can be raised appreciably by energy recovery from the spent beam. This can be done by 'unwinding' the beam before leading it to depressed collectors. A scheme for doing this has been proposed and analysed for the case of a large-orbit gyrotron. It involves the use of a second cusp with a reversed magnetic field for the purpose of beam-conditioning. It is seen that in this way a large fraction of the energy in the spent beam gets converted into energy of axial flow. Furthermore, the following conclusions emerge:

1. $\alpha_{residual}$ varies slowly with accelerating voltage.
2. $\alpha_{residual}$ varies cyclically with starting radius, magnetic field, and distance between cusps.
3. $\alpha_{residual}$ is a minimum when the scalloping motion of the electrons is inwards as they enter the second cusp.
4. The second cusp can be made wider than the first cusp to allow for a larger gap to let the spent electron beam through.
5. The combined action of the electrostatic field provided by depressed collectors of suitable shape and the magnetic field profile beyond the second cusp sorts the electron stream coming out of the latter onto the depressed collectors.

6. Collection at depressed potentials results in energy recovery. This enhancement of overall efficiency is feasible as well as particularly attractive for modes of operation that have low electronic efficiency.

The basic approach can be applied to other types of devices employing spiralling electron beams, for enhancing their overall efficiency.

Acknowledgments

The help rendered by Dr. E. P. Chojnacki is gratefully acknowledged. This work has been supported by the Air Force Office of Scientific Research.

References

Arnush, D., Boehmer, H., Caponi, M. Z., and Shih, C. C., 1982. Design of a high power CW free electron maser. *International Journal of Electronics*, **53**, 605–616.

Bekefi, G., Shefer, R. E., and Destler, W. W., 1986. Millimeter wave radiation from a rotating electron ring subjected to an azimuthally periodic wiggler magnetic field. *Nucl. Instrum. Methods Phys. Res.*, **A-250**, 352–356.

Chojnacki, E., Destler, W. W., Lawson, W., and Namkung, W., 1987. Studies of microwave radiation from a low-energy rotating electron beam in a multiresonator magnetron cavity. *Journal of Applied Physics*, **61**, 1268–1275.

Destler, W. W., and Rhee, M. J., 1977. Radial and axial compression of a hollow electron beam using an asymmetric magnetic cusp. *Physics of Fluids*, **20**, 1582–1584.

Destler, W. W., Chojnacki, E., Hoeberling, R. F., Lawson, W., Singh, A., and Striffler, C. D., 1988. High power microwave generation from large-orbit devices. To be published, *IEEE Trans. on Plasma Science*, April 1988.

Fix, A. Sh., *et al.*, 1984. The problems of increase in power, efficiency, and frequency of gyrotrons for plasma investigations. *International Journal of Electronics*, **57**, 821–826.

Granatstein, V. L., 1984. High average power and high peak power gyrotrons: present capabilities and future prospects. *International Journal of Electronics*, **57**, 787–799.

Granatstein, V. L., 1987. Status of high power gyrotron technology, *Proceedings of Particle Accelerator Conf.*, Washington DC, March (to be published).

Grow, R. W., and Shrivastava, U. A., 1982. Impedance calculations for travelling wave gyrotrons operating at harmonics of cyclotron frequency in magnetron type circuits operating in the π mode. *International Journal of Electronics*, **53**, 699–707.

Herrmannsfeldt, W. B., 1979. Electron trajectory program. SLAC Report 226, November.

Kosmahl, H. G., 1982. Modern multistage depressed collectors, A review. *Proc. IEEE*, **70**, 1325–1334.

Lau, Y. Y., and Barnett, L. R., 1982. Theory of a low magnetic field gyrotron (Gyromagnetron). *Int. J. Infrared Millimeter Waves*, **3**, 619–644.

Lawson, W., Destler, W. W., and Striffler, C. D., 1985. High-power microwave generation from a large-orbit gyrotron in vane and hole-and-slot conducting wall geometries. *IEEE Trans. Plasma Science*, **PS-13**, 444–453.

Lawson, W., and Latham, P. E., 1987. The design of a small-orbit/large-orbit gyroklystron experiment. *Journal of Applied Physics*, **61**, 519–528.

Rager, J. P., 1986. Gyrotron development in the framework of European fusion programme. *International Journal of Electronics*, **61**, 697–700.

Rhee, M. J., and Destler, W. W., 1974. Relativistic electron dynamics in a cusped magnetic field. *Physics of fluids*, **17**, 1574–1581.

Scheitrum, G. P., and True, R., 1981. A triple pole piece magnetic field reversal element for generation of high rotational energy beams. *Tech. Digest IEDM*, 332–334.

True, R., 1987. Emittance and the design of beam formation, transport and collection systems in periodically focussed TWT's. *IEEE Trans. Electron Devices*, **ED-34**, 473–485.

Uhm, H. S., Kim, C. M., and Namkung, W., 1984. Linear theory of cusptron microwave tube. *Physics of Fluids*, **27**, 488–498.

STUDY OF AN ENERGY RECOVERY SYSTEM FOR A LARGE-ORBIT GYROTRON

A. Singh, W.W. Destler, D. Goutos, V.L. Granatstein, W.R. Hix, W. Lawson, and C.D. Striffler

Laboratory for Plasma Research
University of Maryland, College Park, Maryland 20742

ABSTRACT

An approach towards energy recovery from the spent beam of a large-orbit gyrotron is outlined in the form of a double magnetic cusp arrangement. The first cusp produces a large rotational velocity, the second cusp serves the purpose of unwinding the axis encircling beam before it proceeds towards depressed collectors. The results of numerical simulations are summarized for beam transmission through the two cusps.

An experimental set-up for proof of principle is described. Results are presented in the form of depressed potential on a Faraday cup versus the current collected at it. Current collection is observed up to larger depressed potentials when the second cusp is introduced, compared with the case where field reversal is not introduced: thus verifying the concept. A design for multiple depressed collectors is presented along with trajectories in the collector region.

1. INTRODUCTION

The objective of this work is to demonstrate energy recovery from the spent beam by the use of depressed collectors in spiraling beam devices as a means of enhancing overall efficiency. Depressed collectors for linear beam devices have been the subject of extensive study and application.

In applying depressed collector techniques to spiraling beam devices, it is necessary in the latter case to convert the substantial rotational motion in the spent beam into axial motion before it proceeds to depressed collectors. We have proposed a scheme for studying this for a large orbit gyrotron, using a double cusp arrangement.[5] Figure 1 shows a schematic diagram of such a system. A magnetic cusp with a reversed field profile follows the rf interaction region and reconverts the rotational electron motion into axial motion.

We have examined the trajectories of electrons going through the two cusp system. [6] In this way the residual rotational motion left in the electrons due to parameters, like finite transition widths of the cusps, the distance between them, the magnetic field profile, the beam voltage and the radius at which the electrons start, has been estimated. The choice of parameters is in a range defined by the earlier cusptron experiments at the University of Maryland. [7] Illustrative data of these studies and guidelines worked out for optimization of the conversion process are presented in section 2.

We have also set up a proof-of-principle experiment. Its main features are described in section 3. The experimental results on beam transmission through the two cusps and measurements on the current collected by a Faraday cup at depressed potentials are presented in section 4. It is seen that with the field reversal at the second cusp, the current collection continues up to higher depressed potentials than without such reversal.

Furthermore, the electron trajectories of the spent beam have been simulated in the depressed collector region, under a range of conditions of collector geometry, potentials, magnetic field profiles and energy variations in the incoming beamlets. Typical trajectories and estimates of collector efficiency are given in section 5, along with the latest design. Conclusions are summarized at the end.

2. CONVERSION OF ROTATIONAL MOTION INTO AXIAL MOTION

In this study, a useful parameters is α, defined as the ratio of the perpendicular component of velocity $v_\perp$ to the parallel component of velocity $v_\parallel$. A representative example of studies of $\alpha_{residual}$, defined as $v_\perp/v_\parallel$ in the region after the second cusp, is shown in Figure 2, where it is plotted versus the starting radius of the electrons. The starting radius varies from 1.4 to 1.6 cm, the beam voltage is 26 kV, the magnitude of the magnetic field is 330 Gauss. As the particles cross the first cusp, the α is a function of the starting radius r_{st}. The finite transition width of the first cusp results in the guiding center being somewhat displaced from the axis. As a result, the particle enters the second cusp with a radial motion that is inwards or outwards depending upon the number of gyrations completed, especially the fractional part. This fractional part converted into degrees (full cycle = 360°), is also shown in Figure 2.

It is seen that $\alpha_{residual}$ has a cyclical variation with r_{st}. However, it stays generally below 0.32, representing only about 10% of the electron energy in residual rotational motion. The cyclic variation is linked with the fractional part

0-X-XX/XXXX-0155 $1.00 © 1988 IEEE

of the gyrations performed in transit between the two cusps. As discussed in detail elsewhere [6], this can be understood by recalling that the finite width of the first cusp results in an outward motion of an axially streaming particle passing through it, so that over and above the conversion of the axial to rotational velocity, the guiding center is shifted off-axis, resulting in a finite $\alpha_{residual}$. But a particle that enters the second cusp with an inward radial motion has it counteracted by the latter, and vice versa. To minimize the $\alpha_{residual}$ over the whole beam, it is desirable to reduce the range of r_{st}, consistent with the current density available from the cathode. The set of parameters can then be fine tuned to give a low average of $\alpha_{residual}$. The width of the first cusp needs to be minimized. That of the second cusp needs to be of the same order, though a somewhat greater value can be accommodated, so as to provide a larger aperture for the spent beam to pass through.

3. THE EXPERIMENTAL SET-UP

The basic arrangement is shown schematically in Figure 1. A photograph of the set-up is shown in Figure 3. In this the electron-gun is on the left hand side, followed by two iron plates which generate the magnetic cusps with the aid of coils that carry appropriate currents. There are seven of them in all.

Profiles of the magnetic field have been generated to correspond to near constant B_z field in the gun and rf regions denoted by B_0, and controlled reductions of the z component in the collector region. Profiles have been also measured for individual contributions of each coil. If the flux density is well below saturation in the iron plate, linear superposition can be assumed, and different profiles synthesized.

In the initial proof of principle, a Faraday cup is located in the collector region. It consists of copper with a coating of carbon. This coating would help to reduce the number of back-scattered electrons. It can be put at depressed potentials by a separate power supply. The pulse as well as dc components of the current collected at different potentials are measured. The wave form of the current is converted into a voltage pulse by a pick-up coil, which is then displayed on an oscilloscope. The dc component of current is measured with the help of a filter that bypasses the higher frequency components of the current. The cathode in the gun is fed with negative pulses up to 30 kV and duration of 5 microseconds, at a rate of 60 pulses per second. The duty ratio is then 0.0003. For a pulse of collector current of 0.2 ampere, the dc component of the collector current would thus be 60 microamperes.

4. COLLECTOR CHARACTERISTICS

Measured characteristics of the Faraday cup that can in a limited way function also as a depressed collector are shown in Figure 4 for one set of parameters, corresponding to an accelerating voltage of 15.5 kV and a field strength B_0 of 255 Gauss. The cusp half-width is approximately 4 mm for the first cusp and 8 mm for the second cusp. The distance between them is 32 cm.

One curve is for the case where a magnetic field reversal is produced at the location of the second iron plate. The second curve represents the case where the direction of current in the coils in the collector region is reversed, and the values so adjusted as to give the same value of B_0 beyond the second cusp, without reversal of direction. This is only an approximation to a constant field, to contrast with the case of field reversal. Actually, there is a dip in the value of the B_z component at the location of the second iron plate because the lines of field tend to fan out towards the iron. This tends to influence the beam transmission through the hole in the second iron plate. Furthermore, while the surface of the cup is treated to reduce secondary emission, it does not have a retarding field to suppress secondaries, as in the case of the design in the next section. Consequently the collector current here is diminished by some returning secondaries. However, the maximum depressed potential at which the collected current reduces to zero still remains valid.

It is seen that the maximum depressed potential up to which the Faraday cup collects current is -13 kV in the case where the second cusp is present; and -7 kV in the case where there is no second cusp. These figures demonstrate that the introduction of the second cusp has increased the depressed potential up to which the 'spent' beam can be collected, thus increasing energy recovery. The value of α after a particle passes the first cusp is given by:

$$\alpha = [(\frac{v_0}{r_{st}\omega_c})^2 - 1]^{1/2},$$

where v_0 is the axial velocity prior to reaching the first cusp, and ω_c is the angular cyclotron frequency. The α for an accelerating voltage of 15.5 kV, B_0 = 255 Gauss, and r_{st} varying from 1.4 cm to 1.6 cm, varies from 1.57 to 3.68. This implies that there is a spread in the energy of axial motion, both in the 'rf' section and beyond the second cusp. The maximum depressed potential of -13 kV corresponds to electrons which emerged from the second cusp with an α of 0.43, indicating conversion of rotational into axial motion. As discussed already, for getting conditions closer to ideal the cusp widths as well as the range of r_{st} would have to be reduced.

5. A DESIGN FOR MULTIPLE DEPRESSED COLLECTORS

When rf interaction takes place, the energy of the beam gets spread out over a narrow or wide range, depending upon the electronic efficiency. In order to have maximum energy recovery, it is necessary to sort the beam into beamlets covering smaller ranges of energy, collected on multiple collectors each depressed to a potential adjusted for collecting the beamlet with minimum loss of energy, i.e., as a soft-landing.

We have run simulations of trajectories using the Herrmannsfeldt code. [8] Systems employing three and four

...considered for primary electron trajectories. ...present study, five collectors have been used and ...steps taken towards consideration of the effect of ...secondary electrons. These secondary or reflected pri... ...reduce the collector efficiency when they end up on ...at a lesser depressed potential. They can disturb ...trajectories if they head all the way back to that re... ...trajectories for the primary particles are shown in ...the currents are at energies of 18.2, 20.8, 23.4, 26.0, ...30 keV, the scatter representing the effect of rf in... ...energy sorting is observed among the depressed ...

...choosing the geometry of the collectors and values of ...parameters, a consideration kept in mind was that any ...secondary electrons or reflected primaries released from its ...point of impact should see a retarding electrostatic field, so ...as to minimize loss of collector efficiency, or backtracking ...electrons. In the case of energetic reflected primaries ...may enter a region of acceleration by overcoming the ...initial retarding field. Thus the configuration and param... ...shown for Fig. 5 are not those which give the highest ...collector efficiency when primary electrons alone are con... ...For the instance the parameters are so adjusted that ...a few high energy particles hitting the central or flat ...part of the back plate which is at the highest depressed ...potential. Consequently almost all the back-scattered elec... ...are either reabsorbed on the same collector that they ...impact or go to another collector which is one stage lower. ...Thermal losses are thus minimized

...In the present case, the trajectories of back-scattered ...electrons are traced by re-running the Herrmannsfeldt code ...with the impacted collectors were 'cathodes'. They are ...launched just outside the surface of the electrode. Figure ...shows the trajectories of the back-scattered electrons cor... ...corresponding to the primaries shown in Figure 5. Certain ...simplifying assumptions regarding the energy and direction ...of back-scattered electrons are made, in order to obtain ...first order effects. The angle of 'reflection' is made equal ...to the angle of 'incidence' with respect to the normal to the ...surface. [10] The energy of the true secondaries is assumed ...to be 50 ev. The energy of the reflected primaries is taken to ...be 0.3 times the net energy of impact and the back-scatter ...current is taken to be 0.3 times the primary current, these ...values being approximations for average coefficients in the ...case of copper as the material for the electrodes. [11] In ...actual practice the angles and energies would have a natu... ...spread. The back-scatter coefficient would be dependent ...also upon the surface treatment or any deposited layer, such ...as carbon, as well as the angle of incidence.

The trajectories in Figure 6 show that out of 25 particles ...tracked, almost all the secondaries are suppressed. These ...are the small squiggles at the points of impact of primaries. ...Some are returned to the collector with the next highest ...depressed potential; and one returns towards the entrance ...of the collector region. Similarly all the reflected primaries ...are collected on the same electrode, with the exception of ...two that go to a less depressed collector. The exceptional trajectories happen to lie at the edges of the energy distribution curve, and have less weightage than the median particles. Thus, the effect of these back-scattered electrons in reducing the estimated collector efficiency is minimized. With the present level of approximations, the collector efficiency is estimated to lie in the rage of 70 to 80%.

6. CONCLUSIONS

Results of a proof-of-principle experiment have been presented for a double cusp system for energy recovery from spent beam in a large-orbit gyrotron. They lend support to the basic approach of unwinding the beam at the second cusp. A depressed collector system has been designed, including trajectories for primary as well as back-scattered electrons. This system has demonstrated energy sorting, with an estimated collector efficiency in the range of 70 to 80%.

ACKNOWLEDGEMENTS

The work is supported in part by the U.S. Department of Energy and AFOSR. The help rendered by Douglas Cohen and Kenneth Diller in fabrication of parts for the experiment is thankfully acknowledged.

References

[1] H.G. Kosmahl, Proc. IEEE 70, 1325-1334 (1982).

[2] P. Ramins, et al., IEEE Trans. ED-33, 1902-1914 (1986).

[3] A.N. Curren, IEEE Trans. ED-33, 473-485 (1986).

[4] R. True, IEEE Trans. ED-34, 473-485 (1987).

[5] A. Singh et al., Conference Record IEEE International Conference on Plasma Science, p. 40 (1987).

[6] A. Singh et al., Intl. Jour. of Electronics, Gyrotron special issue, to be published (1988).

[7] E. Chojnacki et al., J. Appl. Phys. 61, 1268-1275 (1987).

[8] W.B. Herrmannsfeldt, SLAC Report 226 (Nov. 1979).

[9] A. Singh, et al., Conference Digest Twelfth International Conference on Infrared and Millimeter Waves, 389-390 (1987).

[10] D.A. Force, NASA Technical Paper 2664 (Nov., 1986).

[11] A.J. Antolak et al., J. Appl. Phys. 58, 526-534 (1985).

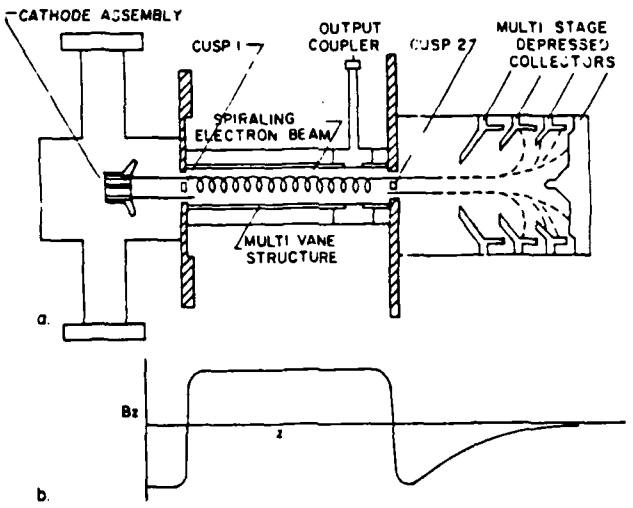

Fig. 1. a) Schematic diagram of the double-cusp system for energy recovery from spent beam in a large-orbit gyrotron, b) Typical magnetic field profile.

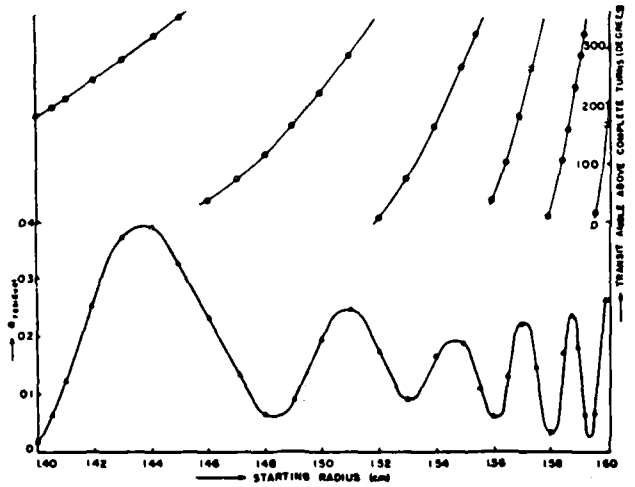

Fig. 2. Transit angle over and above complete turns, and $\alpha_{residual}$ just beyond the second cusp versus the starting radius.

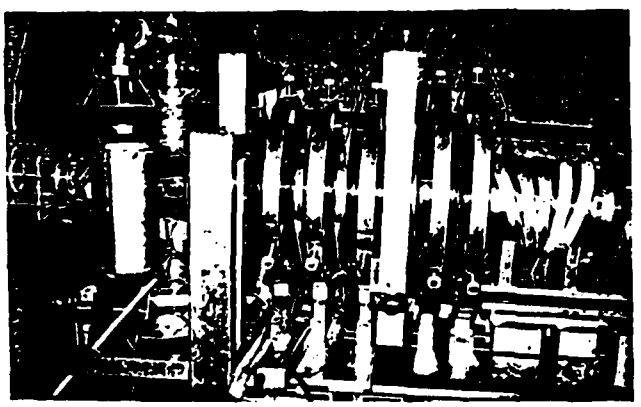

Fig. 3. A view of the experimental set-up.

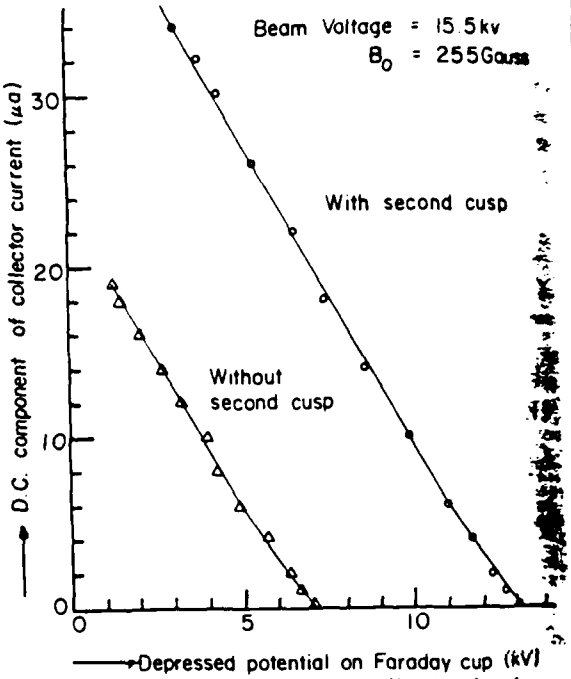

Fig. 4. Characteristics of current collection by the Faraday cup versus the depressed potential applied to it.

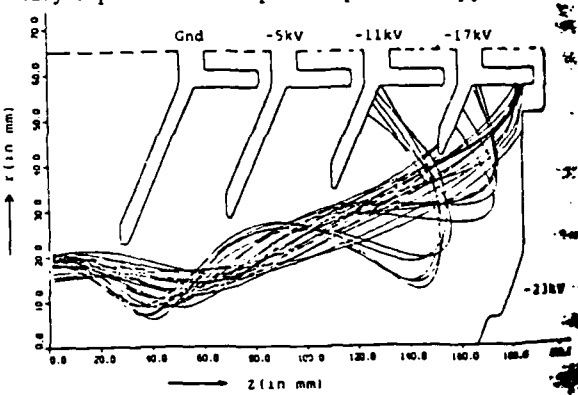

Fig. 5. Trajectories of primary electrons in a multiple depressed collector.

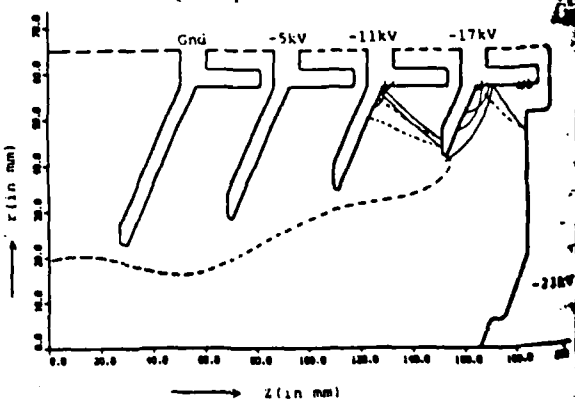

Fig. 6. Trajectories of back-scattered electrons for parameters and points of impact of primaries in Figure 5. The continuous lines are reflected primaries and the dotted lines are true secondaries.

Short-pulse high-power microwave propagation in the atmosphere

C. A. Sullivan, W. W. Destler, J. Rodgers, and Z. Segalov
Electrical Engineering Department and Laboratory for Plasma and Fusion Energy Studies, University of Maryland, College Park, Maryland 20742

(Received 12 November 1987; accepted for publication 12 February 1988)

The propagation of high-power (10–200 kW/cm^2) short-burst (3–30 ns) microwave pulses in the atmosphere has been studied experimentally. Microwave power from a large orbit gyrotron operating at 9.6 GHz is focused by a large-diameter parabolic reflector into a test cell. The ambient pressure in the test cell was varied over a wide range and the microwave power density necessary for atmospheric breakdown has been determined as a function of ambient pressure and pulse duration. Measurements of the microwave pulse duration before and after breakdown have been obtained to determine the extent to which microwave energy is absorbed or reflected by the breakdown plasma. Results are compared with available theory and previously reported experiments.

I. INTRODUCTION

Although microwave breakdown of the atmosphere has been a subject of study for many years,[1–10] considerable new interest has recently developed in the field arising from the availability of very high-power microwave sources developed for directed-energy systems and high-power radar applications. In particular, data obtained from experiments investigating microsecond-pulse rf breakdown in air have supported theoretical predictions that very high microwave power levels could be propagated in the atmosphere if the pulse duration could be made sufficiently short. It has also been proposed that at low ambient pressures a very high-power microwave pulse might accelerate free electrons to energies in excess of that associated with the peak in the ionization cross section for air in a distance short compared to a mean free path. In this manner even higher microwave powers might be propagated without breakdown.

Considerable theoretical and experimental work has been reported in this area in recent years.[11–17] Theoretical results reported by Woo and DeGroot,[11] Yee *et al.*,[12] and Ali and Coffey[13] have indicated that when breakdown occurs, an ionization front is rapidly formed which moves toward the microwave source and consequently decouples the microwaves from the initial breakdown region. In addition, the amount of energy that can be transmitted through the medium was found to be a strong function of the initial energy of the pulse and its frequency, pulse shape, and duration.

Several experiments have been reported in which the propagation of short-burst microwaves through air has been studied.[14–17] Bollen *et al.*[14] have reported studies of microsecond-pulse microwave breakdown in nitrogen by focusing the output of a 112-kW, 35-GHz gyrotron into a test cell. Breakdown was observed at microwave power densities of about 30 kW/cm^2 at ambient pressures below 75 Torr. Yee *et al.*[12] have reported studies of short-pulse (10 ns) microwave breakdown of air in a rectangular waveguide powered by a 15-MW *S*-band klystron operating at 2.856 GHz. Results of this study were found to be in good agreement with theory and simulation. Experimental results of Gould and Roberts[15] and Tetenbaum, MacDonald, and Bandel[16] employed *S*-band sources with repetition rates of 1200 and 20 pulses per second, respectively. In these cases the test cell was a resonant cavity fed by waveguide. Finally, recent work by Armstrong *et al.*[17] has been reported in which high-power microwaves from an *S*-band relativistic magnetron have been used to study breakdown thresholds. In these experiments, 6-ns microwave pulses were focused by a parabolic reflector into a test cell and the resultant breakdown observed using optical diagnostics.

In this paper, we report the results of an extensive experimental study of short-burst high-power microwave propagation through air. Data have been obtained for transverse electromagnetic (TEM) microwave pulse propagation in a test cell large enough to ensure that surface breakdown does not occur to any significant extent. Furthermore, data have been obtained over a wide range of microwave pulse power densities and pulse durations and for an equally wide range of ambient test-cell pressures. Section II contains a review of available theory relating to these experiments. Section III discusses the experimental apparatus used for the study, and results are presented in Sec. IV. Conclusions are drawn in Sec. V.

II. THEORETICAL DISCUSSION

The theory of microwave breakdown of a neutral media has been extensively treated in early work by MacDonald.[3] It is assumed that breakdown occurs when the electric field of the wave accelerates free electrons in the media to energies sufficient to ionize neutral species and initiate an avalanche process that produces a rapid increase in the plasma density. The continuity equation for electrons in the media can be written

$$\frac{\partial n}{\partial t} = \nu_i n - \nu_a n + \nabla^2(Dn), \tag{1}$$

where n is the electron density, ν_i is the ionization rate, ν_a is the attachment rate, and D is the electron diffusion coefficient. The diffusion term can be approximated as $\nabla^2(Dn) \cong n(-D/\Lambda^2)$, where Λ is the characteristic diffusion length and depends upon the system geometry. Using this approximation, the continuity equation has a solution

$$n = n_0 e^{(\nu_i - \nu_a - D/\Lambda^2)t}, \tag{2}$$

 0021-8979/88/115228-05$02.40

where n_0 is the initial free-electron density. The diffusion coefficient D was found[3] to follow the empirical relation

$$Dp = [29 + 0.9(E/p)] \times 10^4, \tag{3}$$

where p is the ambient media pressure and E is the amplitude of the wave electric field. MacDonald noted that in cw microwave breakdown phenomena steady state is reached and

$$\nu_i - \nu_a = D/\Lambda^2. \tag{4}$$

He then matched these results to data obtained from cw microwave breakdown experiments conducted in a cavity. In this manner he obtained estimates of the net ionization rate $\nu_i - \nu_a$ as a function of ambient media pressure for the given wavelength and electric field amplitude.

For pulsed microwave breakdown, Eq. (4) does not apply and the electron density grows at a rate given by

$$\nu = \nu_i - \nu_a - D/\Lambda^2. \tag{5}$$

A reasonable estimate of the time taken to achieve breakdown will be obtained if it is assumed that breakdown occurs as the plasma density approaches the critical plasma density,

$$n_p = 10^{13}/\lambda^2 \text{ cm}^{-3}. \tag{6}$$

The pulse duration τ for breakdown to occur can then be determined approximately from

$$n_p = n_0 e^{\nu\tau}. \tag{7}$$

Experimentally, the initial free-electron density is not usually known to any degree of accuracy, but the exponential nature of the rise in the electron density with time tends to minimize the effect of errors in the number assumed for n_0. In addition, studies by Rappaport, Latham, and Striffler[18] have indicated that wave propagation can be significantly affected by plasma densities considerably below the critical plasma density, although the exponential nature of the density increase with time minimizes errors resulting from this assumption as well.

In a similar approach, Ali and Coffey[13] theoretically studied breakdown by treating electrons with a Maxwellian velocity distribution. In this work the average electron energy was assumed to be linearly dependent on E/p. They assumed that the ionization in air is primarily from the oxygen molecule and used known values for the attachment frequency and estimates for the diffusion scale length Λ to determine the net ionization rate as a function of ambient pressure and pulse duration.

In addition to this analytical work, significant numerical simulation has been conducted of short-pulse microwave propagation in the atmosphere,[11,12,14] results in reasonable agreement with experiment where data are available.

III. EXPERIMENTAL APPARATUS

High-power microwave pulses used for the propagation studies were generated by a large-orbit gyrotron[17,18] operating at 10 GHz. This device, powered by a pulse line accelerator [2 MeV, 10–20 kA, 30 ns full width at half-maximum (FWHM)], produces high-power microwave radiation (100–500 MW) by the resonant interaction of the modes of an axis encircling rotating electron beam with the modes of a magnetron-type multiresonator circuit. The rotating electron beam is produced by passing a cylindrical, nonrotating beam from a field emission diode through a narrow magnetic cusp, as shown in Fig. 1. The cusp acts to convert the upstream electron axial velocity (v_{z1}) into a downstream azimuthal ($v_{\theta 2}$) and axial velocity (v_{z2}) in a manner given approximately by

$$v_{z1}^2 = v_{z2}^2 + v_{\theta 2}^2 = v_{z2}^2 + r_0^2\omega_c^2. \tag{8}$$

Here $\omega_c = eB/m\gamma$ is the relativistic electron cyclotron frequency, where e is the electronic charge, m is the electron rest mass, B is the axial magnetic field, and

$$\gamma = (1 - v^2/c^2)^{-1/2} \tag{9}$$

is the relativistic mass factor for the beam electrons (c is the speed of light in vacuum). The radius r_0 is the mean radius of the rotating electron beam, which for a symmetric cusp is approximately equal to the cathode radius. Thus for a given applied axial magnetic field, only electrons with energies greater than a value given by

$$E_{th} = [(mc^2)^2 + c^2e^2r_0^2B^2]^{1/2} - mc^2 \tag{10}$$

can pass through the cusp into the downstream drift region.

The above result allows for the use of this facility for the

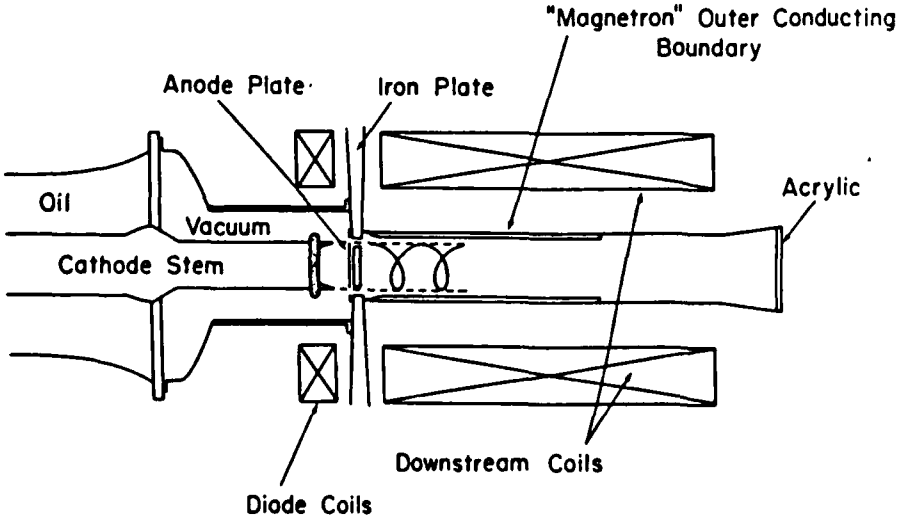

FIG. 1. Large orbit gyrotron experimental configuration.

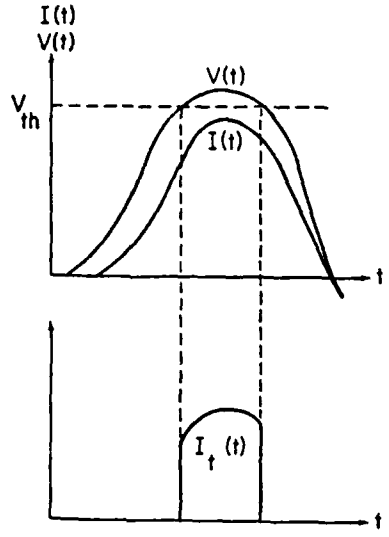

FIG. 2. Idealized upstream diode voltage and current waveforms (top) and downstream current waveform (bottom).

production of very short microwave pulses. Since the diode voltage waveform slowly rises to a maximum value and then slowly decays, the duration of the downstream electron beam pulse can be varied within certain limits by varying the applied axial magnetic field strength. In this manner all electrons with energies below that value required for transmission through the cusp are reflected and the downstream beam pulse can be considerably shorter in duration than the diode pulse, as shown in Fig. 2. Although optimum microwave production cannot be achieved over as wide a variation of magnetic field as might be desired, data have been obtained for microwave pulses of varying power in the range 3–30 ns (FWHM).

The experimental configuration used for the propagation experiments is shown in Fig. 3. Microwaves from the large-orbit gyrotron are focused by a large diameter (150 cm) parabolic reflector with a 75-cm focal length into a 30-cm-diam cylindrical acrylic vacuum chamber which served as the test cell. The test cell was fitted with a high-accuracy vacuum gauge and a calibrated leak valve that allowed maintenance of ambient pressures from atmospheric down to 0.1 Torr. Measurements of the microwave power density along the dish axis within the test cell are shown in Fig. 4. The points plotted are the averages of four shots taken at each

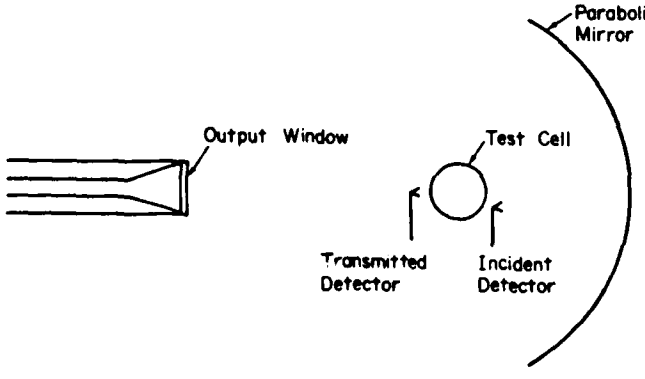

FIG. 3. Configuration used for microwave propagation studies.

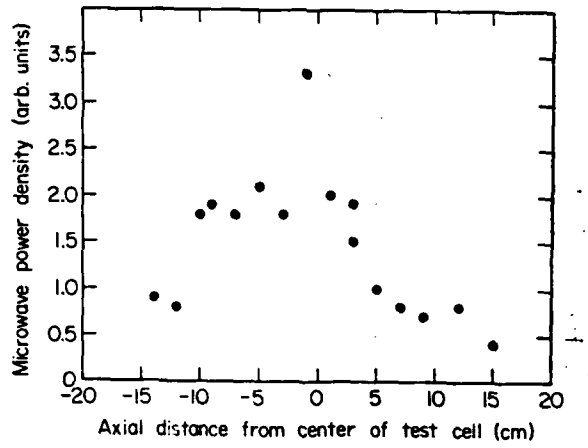

FIG. 4. Microwave power density vs axial distance from the center of the test cell. The test-cell diameter is 30 cm.

position. In this way the effects of shot-to-shot variation in the microwave output power of the device can be minimized. Although the focusing of the microwaves into the test cell was not as effective as had been expected from low-power measurements, it was sufficient to ensure that breakdown, when observed, did not initiate on the test-cell walls. Surface breakdown, which is generally easier to initiate than bulk media breakdown, must be avoided if true media breakdown limits are to be established. The superposition of the incident wave from the source with the reflected wave from the parabolic reflector results in a small-amplitude standing wave in the cell, although measurements indicate that the incident microwave power is more than a factor of 10 lower than the reflected microwave power at the focus. No seed ionization source was used for these studies.

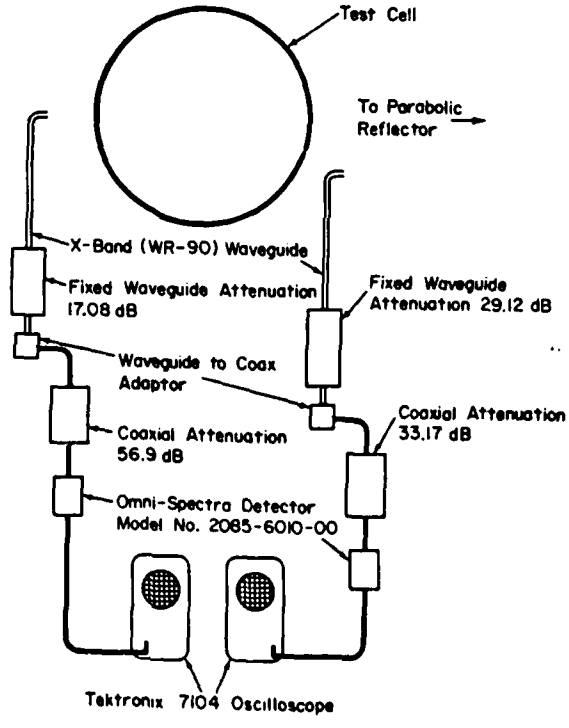

FIG. 5. Schematic of microwave diagnostic setup used in the propagation experiments.

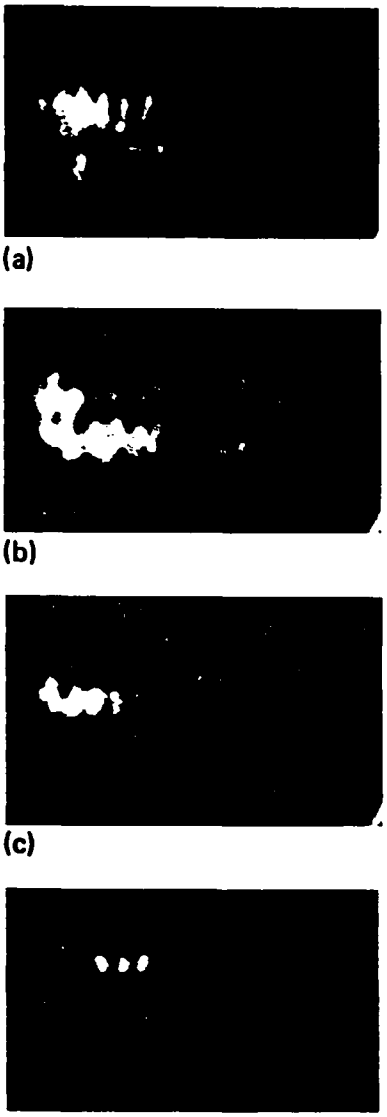

FIG. 6. Time-integrated photographs of microwave-induced breakdown in the test cell, (a) 4.8, (b) 9.5, (c) 20, and (d) 28 Torr.

Open-ended X-band (8–12 GHz) waveguide sections were used to detect the microwave signals before and after the focal point in the test cell, as shown in Fig. 5. The microwave signals were passed through calibrated fixed attenuators to calibrated detectors. All components were calibrated inhouse using standard techniques. The detectors chosen were selected on the basis of their measured transient pulse response time (rise time ~ 1 ns). Detector signals were fed directly into Tektronix 7104 fast oscilloscopes.

IV. EXPERIMENTAL RESULTS

In previous work,[12] the microwave pulse duration that could be propagated without breakdown was determined by simply measuring the duration of the post-breakdown microwave pulse. The experiments reported here were designed so that breakdown could be detected by two independent criteria. The pulse durations before and after the focal point in the test cell were compared to determine if microwave absorption and reflection by breakdown plasma had

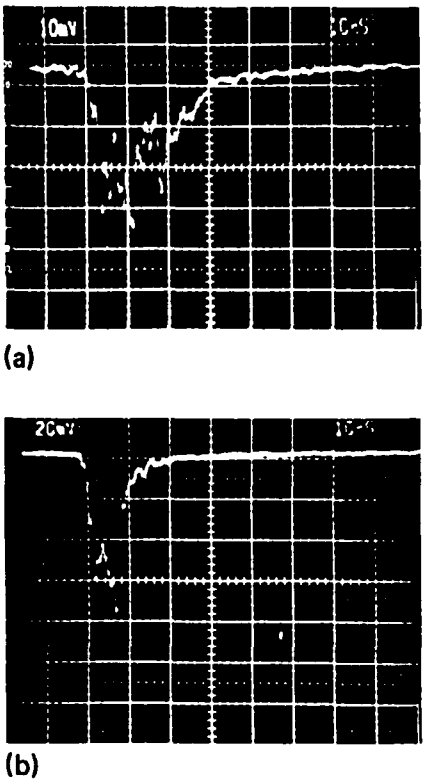

FIG. 7. Typical microwave detector waveforms, (a) incident detector, and (b) transmitted detector. Waveforms correspond to case (a) in Fig. 6.

shortened the duration of the post-focus microwave pulse significantly. In addition, time-integrated photographs of the visible light produced by ionization processes in the test cell were obtained using a still camera. A typical set of photographs of breakdown in the test cell is shown in Fig. 6, and they clearly indicate that surface breakdown at the test-cell wall is not a significant factor in the measurements. For a fixed microwave power density and pulse duration, the breakdown region becomes progressively smaller as the ambient test-cell pressure is increased. At the higher pressures evidence of the small-amplitude standing wave in the test cell can be clearly seen in the photographs. The observed wavelength of the breakdown pattern is fully consistent with

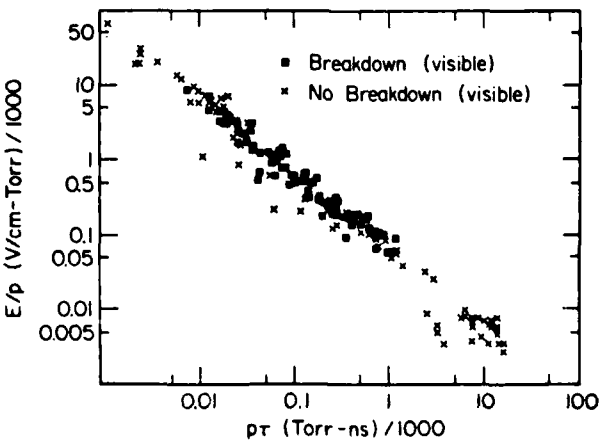

FIG. 8. Microwave propagation data plotted using the visible light criterion for breakdown.

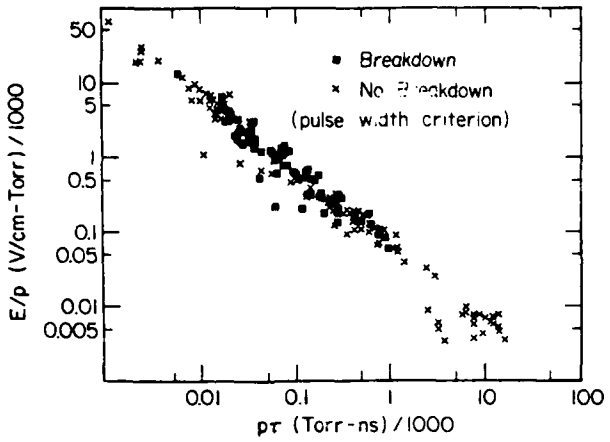

FIG. 9. Microwave propagation data plotted using the pulse width criterion for breakdown.

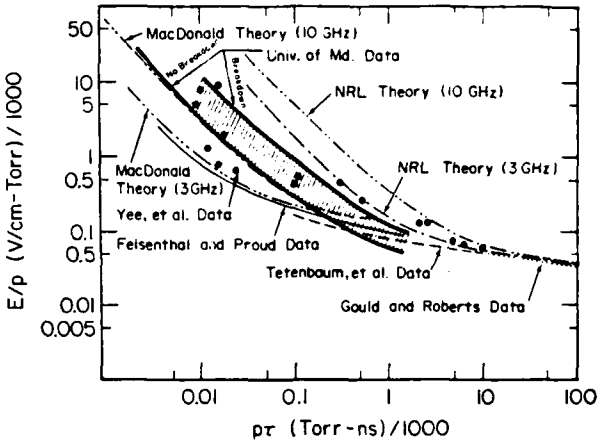

FIG. 10. Comparison of results of present study with available theory and experiment.

the operating frequency (9.6 GHz) of the large-orbit gyrotron.

A typical set of oscilloscope waveforms for the prefocus and post-focus detector systems are shown in Fig. 7. The examples shown are for a case where breakdown resulted in considerable shortening of the post-focus microwave pulse duration. Data from all experiments are plotted in the familiar E/p vs $p\tau$ format in Figs. 8 and 9. The data points in the two plots are the same, but in Fig. 8 the visible light criteria for breakdown was used to indicate on which shots breakdown occurred, and in Fig. 9 breakdown was defined by a measured post-focus pulse duration of 80% or less of the prefocus pulse duration.

V. CONCLUSIONS

From the data it is possible to draw a line on the E/p vs $p\tau$ plot above which breakdown always occurs and a second line below which breakdown never occurs. These results have been compared with data from experiments by Yee *et al.*,[12] Gould and Roberts,[15] Tetenbaum *et al.*,[16] and Felsenthal and Proud[10] in Fig. 10. Also shown are the predictions of theory by MacDonald[3] and Ali and Coffey[13] for wavelengths of 3 and 10 cm.

The data obtained in these experiments are in reasonable agreement with data obtained by Yee *et al.*,[12] for breakdown inside a waveguide at 2.85 GHz. The results are also in reasonable agreement with the theory of MacDonald.[3] Both the present data and the data of Yee *et al.* fall somewhat below the theoretical predictions of Ali and Coffey, although the qualitative agreement between theory and experiment is very good. It is interesting to note that no seed ionization source was employed in these experiments, in contrast to the experiments reported by Yee *et al.*[12] and Gould and Roberts.[15] Usually, seed ionization sources are used to provide a reliable source of small numbers of free electrons to impove reproducibility. In the experiments reported here, reproducibility was not a major problem, although it is likely that x rays produced by energetic electrons striking the drift tube walls produced sufficient free electrons to initiate the breakdown process.

Future experiments are planned to extend the range of data obtained to even higher microwave power densities and shorter pulse durations. In addition, the propagation of high-power microwave pulses through preformed plasmas is also under study.

ACKNOWLEDGMENTS

It is a pleasure to acknowledge useful discussions with Dr. C. D. Striffler and H. Rappaport. We are also grateful for the loan of several pieces of equipment by Harry Diamond Laboratories. This work was supported by the Air Force Office of Scientific Research.

[1] E. K. Smith, Radio Sci. **16**, 1455 (1982).
[2] H. J. Liebe, IEEE Trans. Antennas Propag. AP-31, 102 (1983).
[3] A. D. MacDonald, *Microwave Breakdown in Gases* (Wiley, New York, 1966), p. 160.
[4] H. W. Bandel and A. D. MacDonald, J. Appl. Phys. **41**, 2903 (1970).
[5] W. E. Scharfman, W. C. Taylor, and T. Morita, IEEE Trans. Antennas Propag. **12**, 709 (1964).
[6] D. J. Rose and S. C. Brown, J. Appl. Phys. **28**, 561 (1957).
[7] G. Bekefi, *Principles of Laser Plasmas* (Wiley, New York, 1976), p. 457.
[8] Y. A. Lupan, Sov. Phys. Tech. Phys. **21**, 1367 (1976).
[9] S. M. Flatte, Proc. IEEE **71**, 1267 (1983).
[10] P. Felsenthal and J. M. Proud, Phys. Rev. **139**, A1796 (1965).
[11] W. Woo and J. S. DeGroot, Phys. Fluids **27**, 475 (1984).
[12] J. H. Yee, R. A. Alvarez, D. J. Mayhall, D. P. Byrne, and J. Degroot, Phys. Fluids **29**, 1238 (1986).
[13] A. W. Ali and T. Coffey, Naval Research Laboratory Memorandum Report No. 4320, 1980 (unpublished).
[14] W. M. Bollen, C. L. Yee, A. W. Ali, M. J. Nagurney, and M. E. Read, J. Appl. Phys. **54**, 101 (1983).
[15] L. Gould and L. W. Roberts, J. Appl. Phys. **27**, 1162 (1956).
[16] S. J. Tetenbaum, A. D. MacDonald, and H. W. Bandel, J. Appl. Phys. **42**, 5871 (1971).
[17] W. T. Armstrong, R. A. Roussel-Dupre, R. Karl, M. I. Buchwald, and G. Graham, Bull. Am. Phys. Soc. **31**, 1615 (1986).
[18] H. Rappaport, P. E. Latham, and C. D. Striffler, Bull. Am. Phys. Soc. **31**, 1553 (1986).

Poster Presentation at 1988 APS Plasma Physics Meeting
10/31 - 11/4, 1988, Hollywood, Florida.

Propagation and Breakdown in Gases by Short Burst, High-Power Microwaves*

H.L. Rappaport, P.E. Latham, and C.D. Striffler, University of Maryland, College Park, MD. 20742

We are studying propagation of pulsed high-power microwaves in the atmosphere. Individual processes in our problem include reflection, absorption, and transmission of normally incident electromagnetic radiation onto a finite width resistive plasma and ionization of various gases by high-power RF. We examine methods to solve for propagation characteristics of a time-varying inhomogeneous plasma where the plasma density profile evolution depends on the amplitude of the transmitted electric field. The growth of a plasma in a one-dimensional gas cell using a low ionization rate, long-pulse model is found. The validity of this model is verified by fast Fourier transform methods. Also discussed is a method for solving for propagation characteristics of a time-varying plasma half-space in the critical region where geometrical optics techniques break-down.

*This work is supported by AFOSR.

STATEMENT OF PROBLEM

PURPOSE - TO UNDERSTAND THE PROPAGATION PROPERTIES OF HIGH POWER, SHORT PULSE MICROWAVES THROUGH GASES.

CONFIGURATION AND PARAMETERS OF EXPERIMENT AT MARYLAND

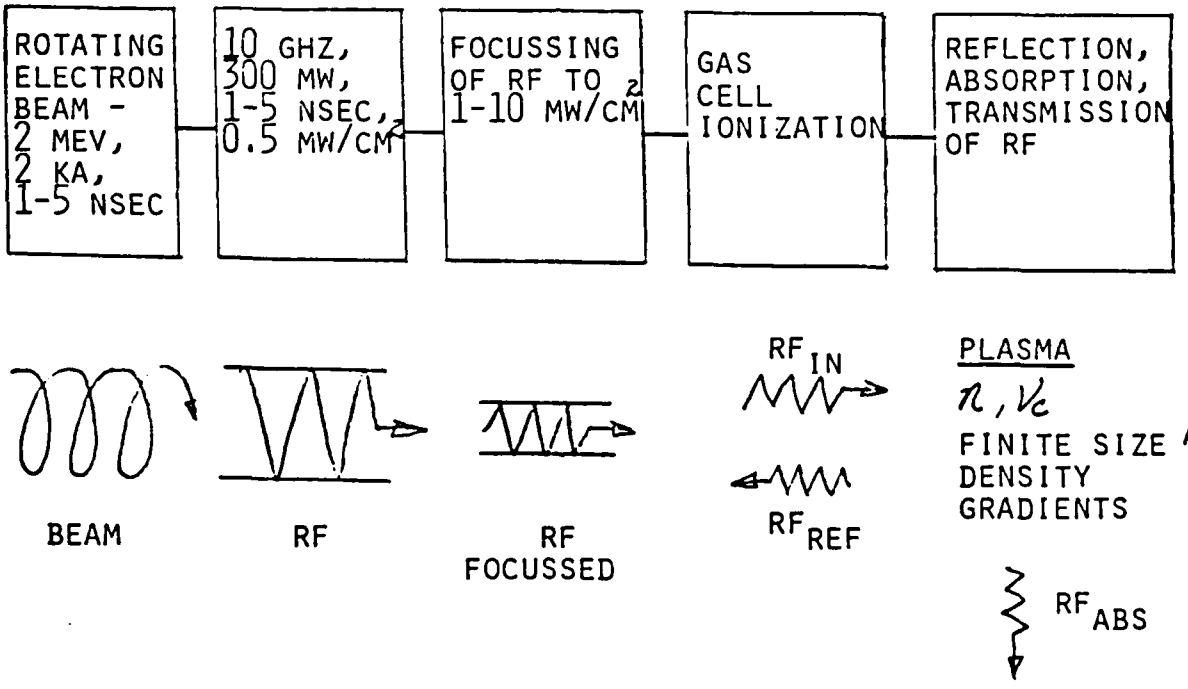

IMPORTANT ISSUES

IONIZATION OF GASES BY RF

PROPAGATION OF RF IN GASES AND PLASMAS

Problem Overview

The total problem of propagation and breakdown in gases may be divided up into the individual processes of ionization of gases by RF and propagation of RF through a time-varying inhomogeneous plasma. We take the view here that if we can solve the propagation problem we can solve the total problem by demanding self-consistency of the time-evolving inhomogeneous plasma density profile with the calculated ionizing electric field propagating through the plasma. The connection between the electric field and the plasma density is made through ionization and attachment rate equations for air.[1] The motivation for the overall approach lies in the fact that the total problem of ionization and propagation combined is a non-linear problem. By considering the propagation problem and ionization problems separately we first solve a linear wave equation with varying coefficients and then afterwards impose self-consistency on the density evolution. This might be done by trial and error, a relaxation method or an iterative technique.

In the first portion of this poster we consider a parameter regime where the ionization rate of the plasma is so low that plasma ionization and RF propagation are on different time scales. In this case methods for solving for the electric field in an inhomogeneous time-independent plasma density are used and self-consistency with the ionizing electric field is imposed.

In the second portion of this poster the propagation problem for a parameter regime where the density may not be considered static is discussed. Here the ionization rate is still held very low compared with the RF frequency and so the term medium ionization rate model seems appropriate.

In future work we may study a parameter regime where the ionization rate is of the order of the RF frequency. This would be called a high ionization rate.

[1]W. Woo and J.S. Degroot, Phys. Fluids 27, 475 (1984).

Low Ionization Rate Model for Microwave Breakdown of Air

We consider the problem of propagation of a normally incident plane wave through a 1-dimensional gas cell. To be found are transmitted and reflected field amplitudes as functions of time. Assuming that the ionization rate is much smaller than the carrier frequency ω_c and that electron momentum change due to ionization is negligible compared to momentum transfer due to elastic scattering, we model our plasma as follows:

Maxwell:

$$\nabla^2 \mathbf{E} - \frac{1}{c^2}\frac{\partial^2 \mathbf{E}}{\partial t^2} = \mu_0 \frac{\partial \mathbf{J}}{\partial t}$$

where $\mathbf{J} = qn\mathbf{v}$

Momentum balance:

$$m\frac{\partial \mathbf{v}}{\partial t} = q\mathbf{E} - m\nu_c \mathbf{v}$$

Electron continuity:

$$\frac{\partial n}{\partial t} = (\nu_i - \nu_a)n$$

Charge neutrality:

$$n = n_e(t) = \sum_{\alpha} Z'_{\alpha} n_{\alpha(ions)}(t)$$

where $Z'_{\alpha} = 1$ for singly ionized molecules, 2 for doubly ionized molecules etc.

Ionization, attachment, and elastic scattering rates for air from Woo and Degroot:

$$\nu_i = P_{\text{Torr}}\, 5.14 \times 10^{11} \exp(-73\alpha^{-.44}) \qquad 32 < \alpha < 100$$

$$\nu_a = P_{\text{Torr}}\, 7.6 \times 10^{-4} \alpha^2 (\alpha + 218)^2 \qquad 0 < \alpha < 60$$

$$\nu_c \approx P_{\text{Torr}} 5 \times 10^9 \qquad \alpha \gg 1$$

$$\alpha \equiv \frac{E_{\text{rms}}}{P_{\text{Torr}} \sqrt{1 + \omega_c^2/\nu_c^2}}$$

In this poster ν_a is taken to be zero when $60 < \alpha < 100$. Solution of the electron continuity equation yields:

$$n(t) = n(0) e^{(\nu_i - \nu_a)t}$$

The momentum balance equation is solved with an integrating factor to yield:

$$v = \frac{q}{m} \int^t d\tau\, e^{\nu_c(\tau - t)} E(\tau)$$

So the 1-dimensional wave equation becomes

$$\frac{\partial^2 E}{\partial z^2} - \frac{1}{c^2} \frac{\partial^2 E}{\partial t^2} = -\frac{\omega_p^2(t)}{c^2} \left[\nu_c \int^t d\tau\, e^{\nu_c(\tau - t)} E(\tau) - E(t) \right]$$

where $\omega_p^2(t) = n(t) q^2 / m\epsilon_0$ and again the ionization rate is taken to be much smaller than the carrier frequency. If we now further assume that the electromagnetic response time $\equiv \tau_{\text{em}}$ of the gas cell is much shorter than $1/\nu_i$ we may take solutions to the wave equation of the form

$$E = \tilde{E}(t) e^{i\omega_c t} e^{i k_z(t) z}$$

for a spatially uniform plasma. The appropriate dispersion relation is

$$\omega_c^2 = c^2 k_z^2(t) + \frac{\omega_p^2(t)}{1 - i\nu_c/\omega_c}$$

PROPAGATION OF NORMAL INCIDENT PLANE WAVE THROUGH A FINITE THICKNESS REGION OF IONIZED AIR

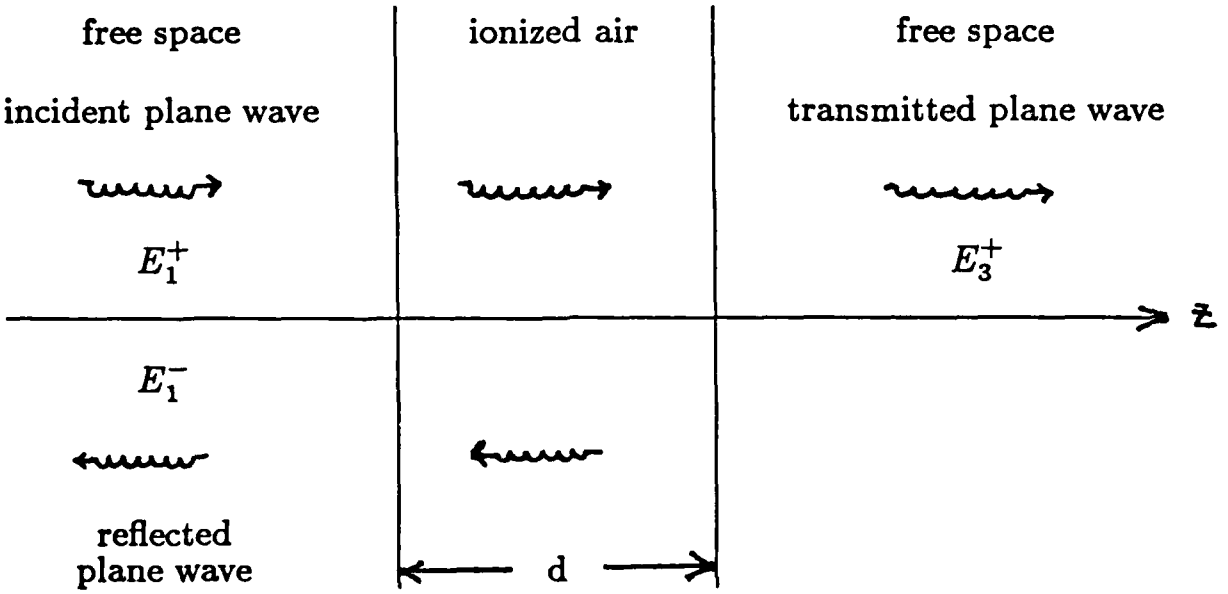

By matching boundary conditions we find

$$\frac{E_3^+}{E_1^+} = \frac{-4n_p e^{jk_z d}}{(1-n_p)^2 - (1+n_p)^2 e^{2jk_z d}}$$

$$\frac{E_1^-}{E_1^+} = \frac{(1-n_p^2)(1-e^{2jk_z d})}{(1-n_p)^2 - (1+n_p)^2 e^{2jk_z d}}$$

where

$$n_p = \sqrt{1 - \frac{n}{n_c(1 - j\nu_c/\omega)}}$$

$$k_z = \frac{\omega}{c} n_p$$

Discussion and Results

The parameters chosen for numerical computation of results in this problem are incident wave amplitude = 1100 V/cm, carrier frequency f_c = 10 Ghz, gas cell length = 4 cm, and gas cell pressure = 5 Torr. In the first set of plots a uniform density model is used, the electron density in the gas cell is assumed to be spatially uniform but increasing with time. At each time step of the calculation the transmitted field, reflected field and the field at the center of the gas cell are found. The field at the center of the gas cell is used to calculate the ionization and attachment rates for the gas which in turn are used to find the electron density for the next time step. We see that the transmitted wave falls sharply in amplitude as the density approaches the critical density $n_c \equiv \omega_c^2 m\epsilon_0/q^2$ at $t \approx 250$ ns. The initial value of $n/n_c = 10^{-9}$ corresponds to an initial electron density of 10^3 electrons/cm^3. Note that $\nu_i \sim 10^8$ and $\omega_c \sim 10^{10}$ so $\nu_i \ll \omega_c$ as required. Also $\tau_{em} \sim .3$ ns as will be discussed momentarily so $1/\nu_i \gg \tau_{em}$ as required. Duration of each time step is 1 ns.

In the next two plots a twenty step model is used and the gas cell is broken up into twenty 4 cm/20 = .2 cm regions. The density in each region is calculated separately at the beginning of each time step. A set of 42 equations in 42 unknown variables is solved numerically to find forward and reverse field amplitudes in each region as well as reflected and transmitted wave amplitudes outside the gas cell. The electric field amplitude at the

center of each region is used to calculate the ionization rate for that region at each time step. Shown is the evolution of the density profile and the evolution of the electric field amplitude across the gas cell with time. Each time step lasts 1 ns. Note that in these plots we may think of the plane wave driving the gas cell as being incident from the left. The electric field amplitude decreases across the gas cell because of elastic collisions. This in turn causes a lower ionization rate on the right side of the gas cell and plasma buildup is greatest on the left side.

The final set of plots allows us to evaluate τ_{em}. Here the Fourier spectrum of an input pulse is multiplied by the frequency response of a uniform in space, constant in time, density plasma of length 4 cm, P = 5 Torr and $n/n_{\mathrm{carrier}} = .5$. n_{carrier} is the critical plasma density at $f = f_{\mathrm{carrier}} = 10$ Ghz. The output pulse in frequency and time domains is shown. Since the input pulse starts at $t = 3$ ns and the output pulse reaches its steady state value at $t \approx 3.3$ ns, $\tau_{\mathrm{em}} \approx .3$ ns. A similiar value of τ_{em} is seen for the case of a 4 cm, 5 Torr, $n/n_{\mathrm{carrier}} = 1.0$ plasma.

Problem Parameters

Carrier frequency = 10 Ghz

Gas cell length = 4 cm

Gas cell pressure = 5 Torr

Initial electron density = 1000 electrons/cm^3

For uniform density model and twenty step model incident plane wave amplitude = 1100 V/cm

Relevant Time Scales

$1/\nu_i = 1.5 \times 10^{-8}$ seconds for $E_{\mathrm{rms}} = 1100$ V/cm

$\tau_{\mathrm{em}} \sim 3 \times 10^{-10}$ seconds

$1/\omega_c = 1.6 \times 10^{-11}$ seconds

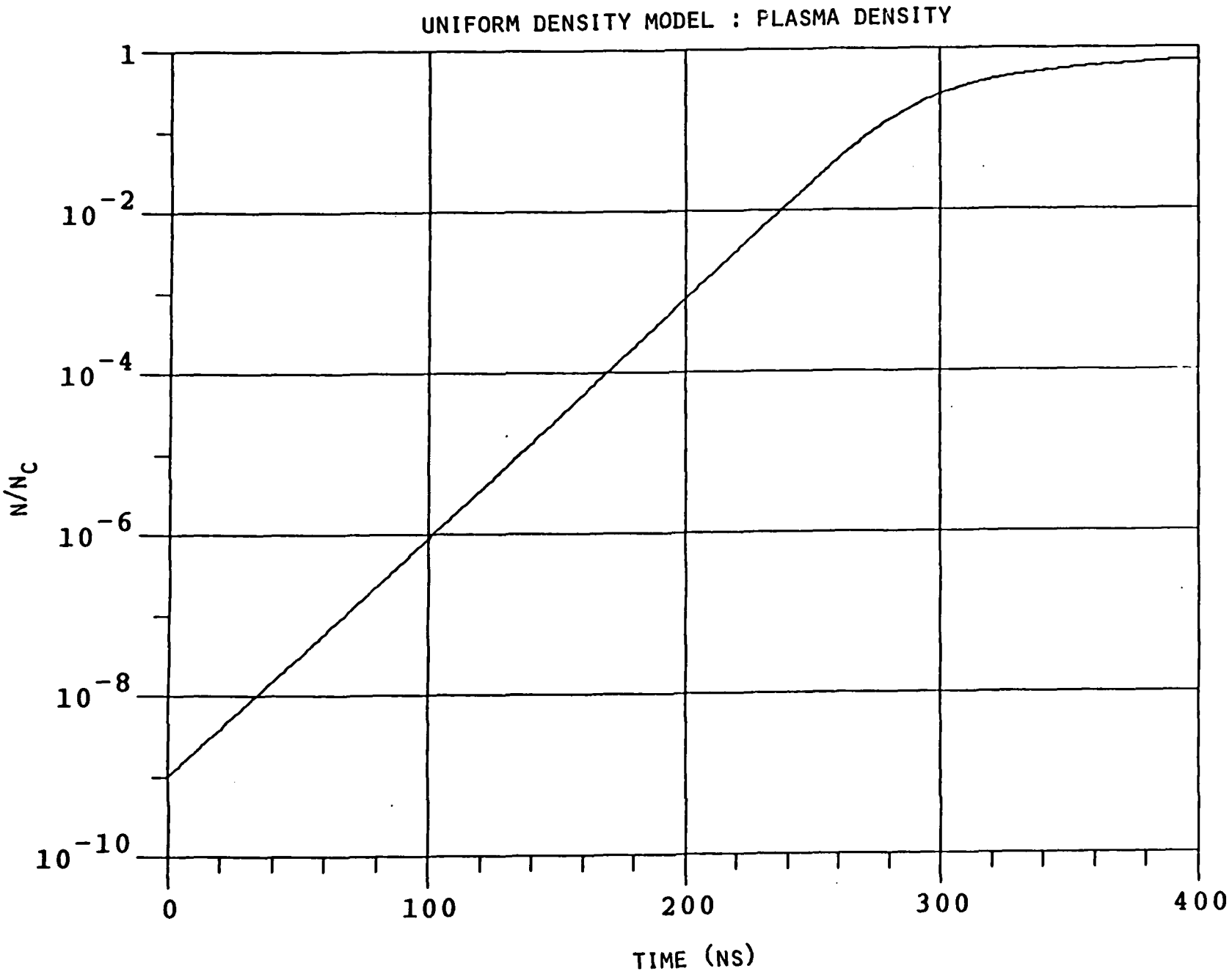
UNIFORM DENSITY MODEL : PLASMA DENSITY
1
10^{-2}
10^{-4}
10^{-6}
10^{-8}
10^{-10}
N/N_C
0
100
200
300
400
TIME (NS)

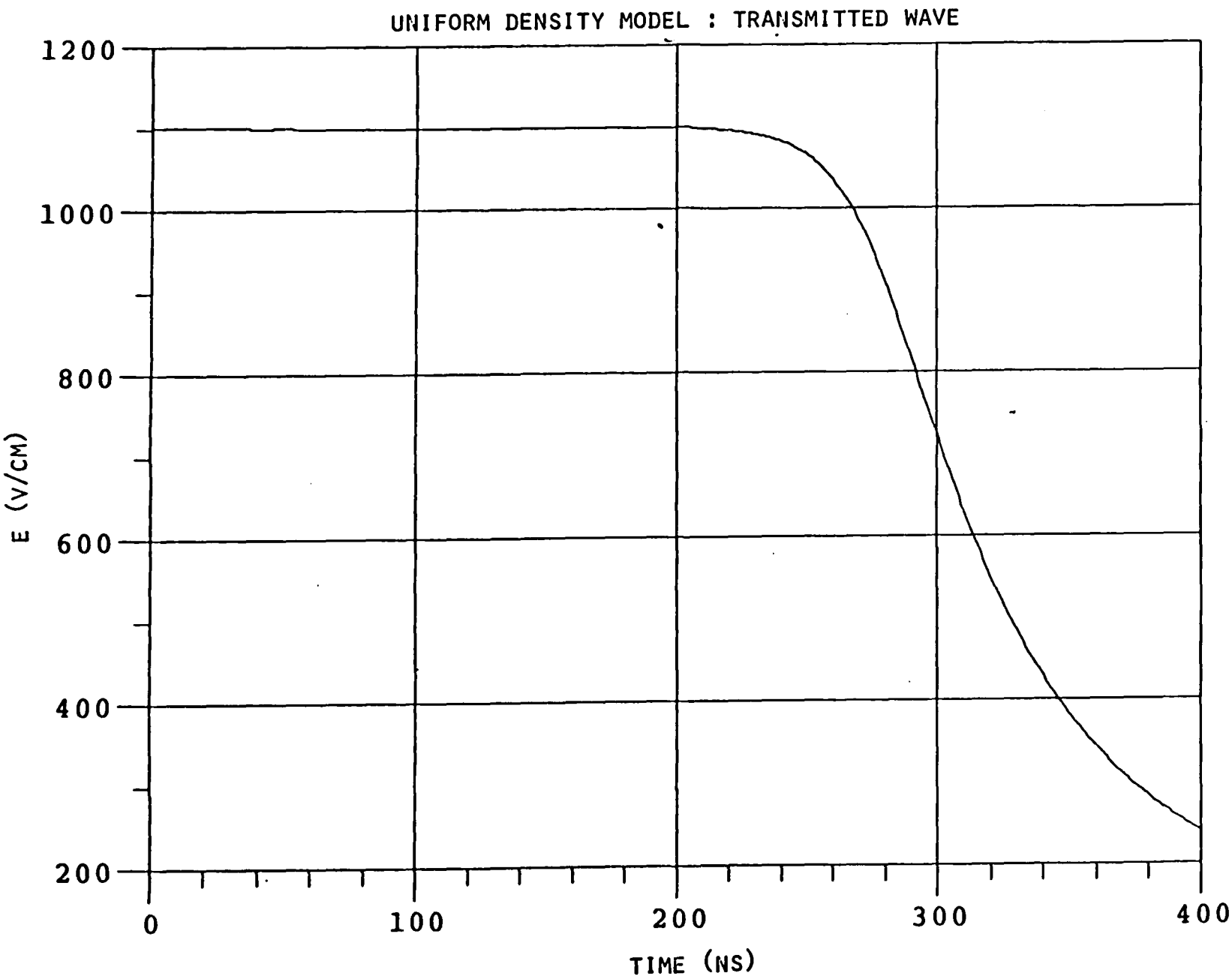
UNIFORM DENSITY MODEL : TRANSMITTED WAVE
1200
1000
800
600
400
200
E (V/CM)
0
100
200
300
400
TIME (NS)

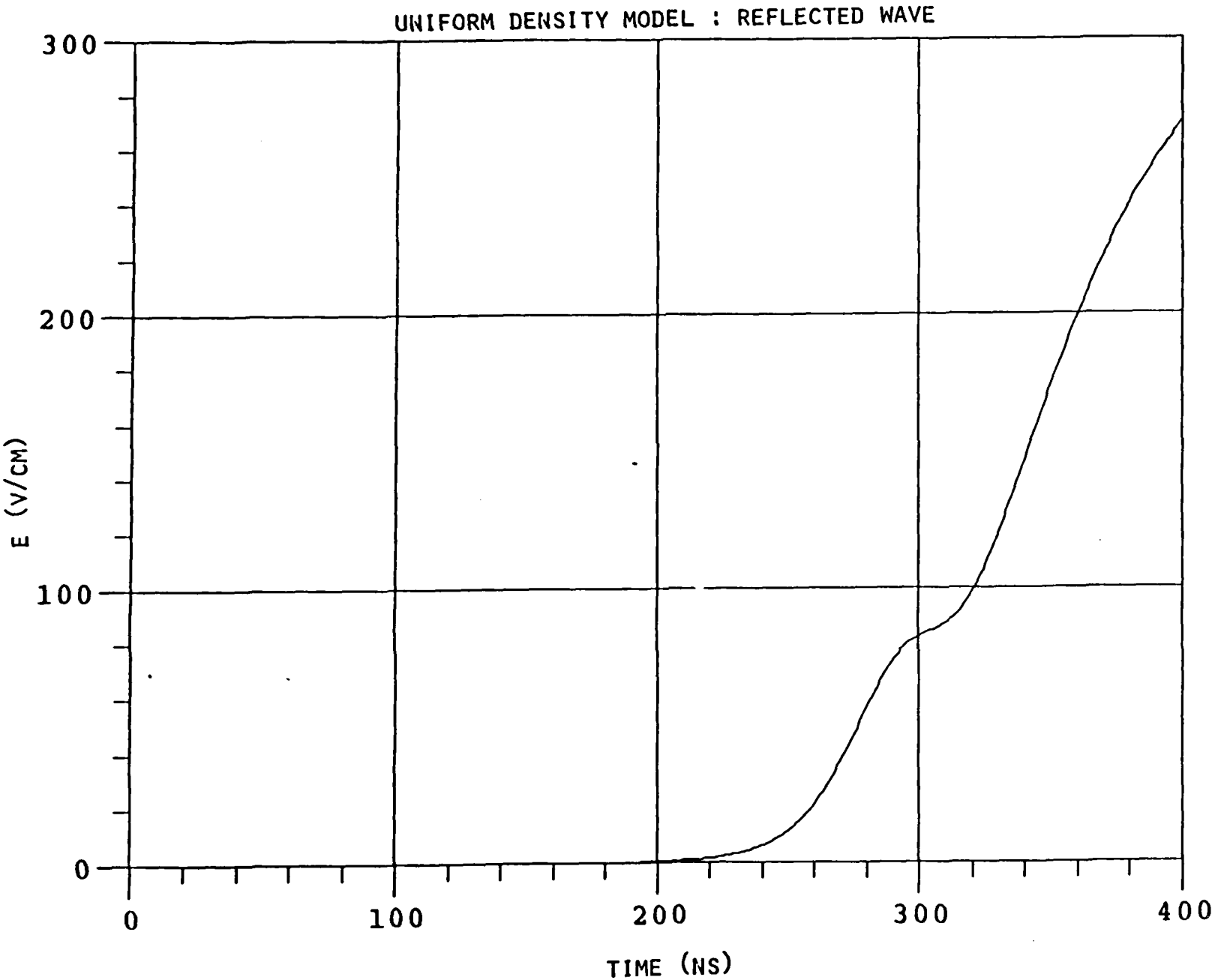
UNIFORM DENSITY MODEL : REFLECTED WAVE
300
200
100
0
E (V/CM)
0
100
200
300
400
TIME (NS)

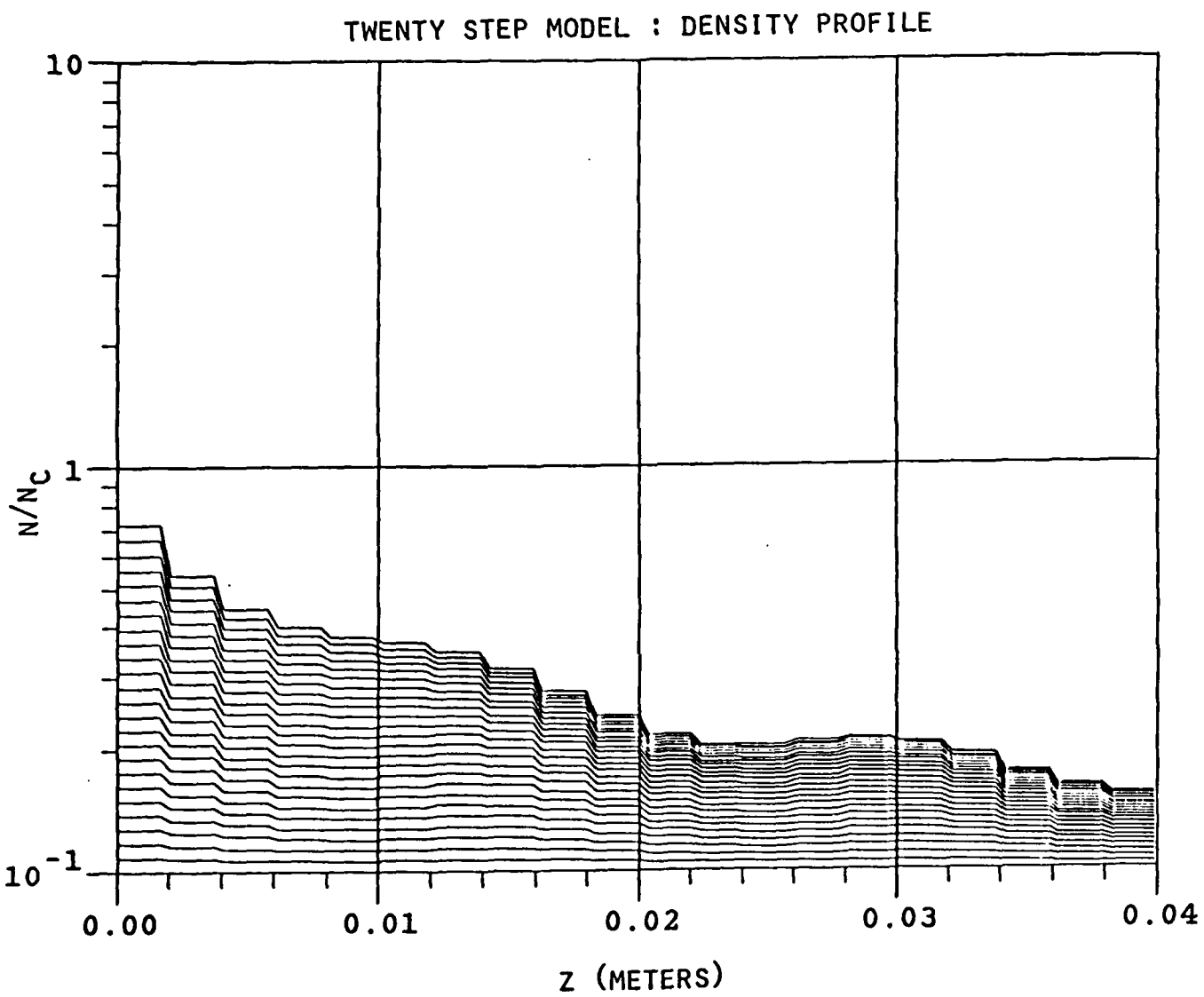
TWENTY STEP MODEL : DENSITY PROFILE
10
1
10^{-1}
N/N_C
0.00
0.01
0.02
0.03
0.04
Z (METERS)

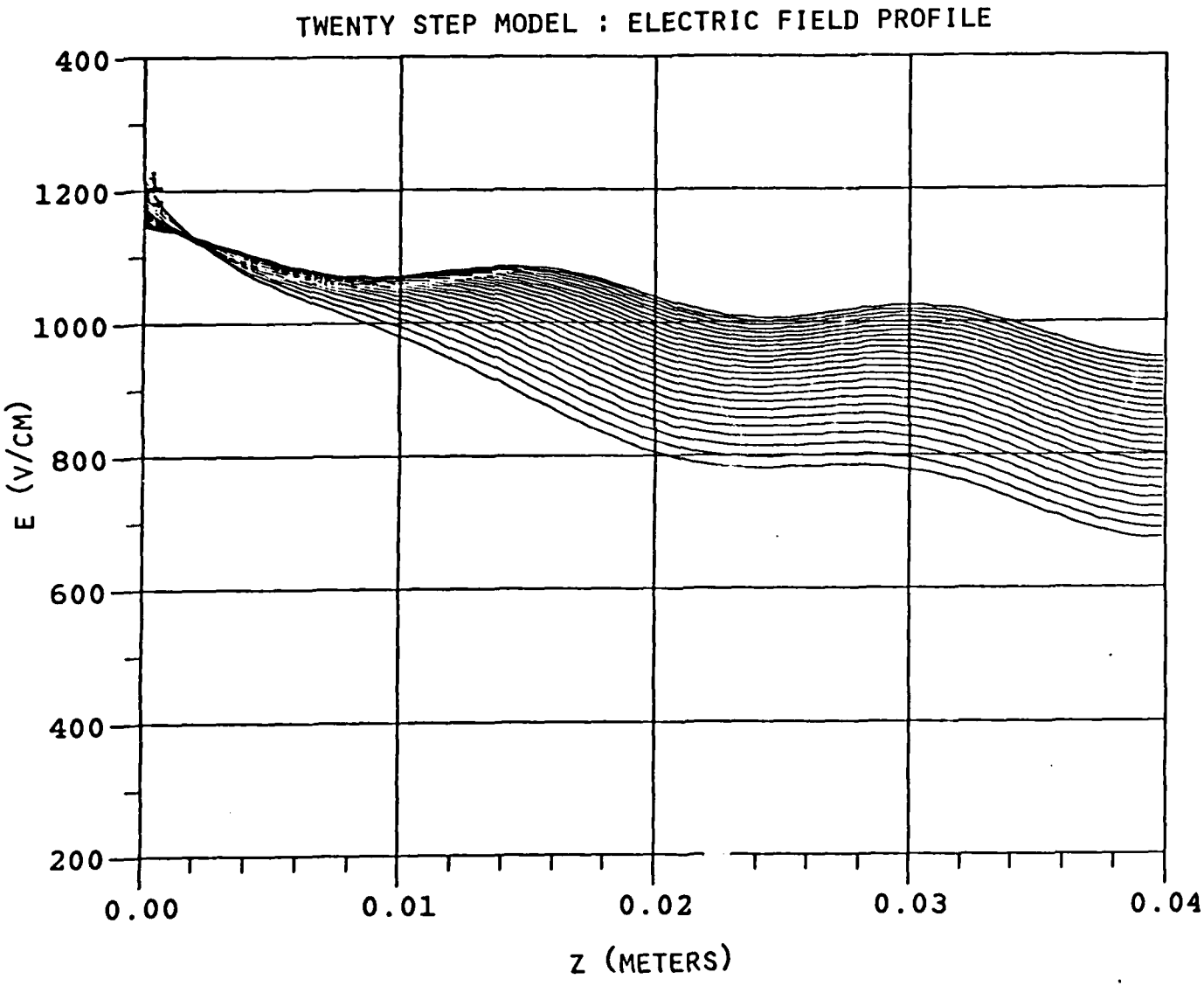
TWENTY STEP MODEL : ELECTRIC FIELD PROFILE
400
1200
1000
800
600
400
200
E (V/CM)
0.00
0.01
0.02
0.03
0.04
Z (METERS)

FAST

FOURIER

TRANSFORM

CODE

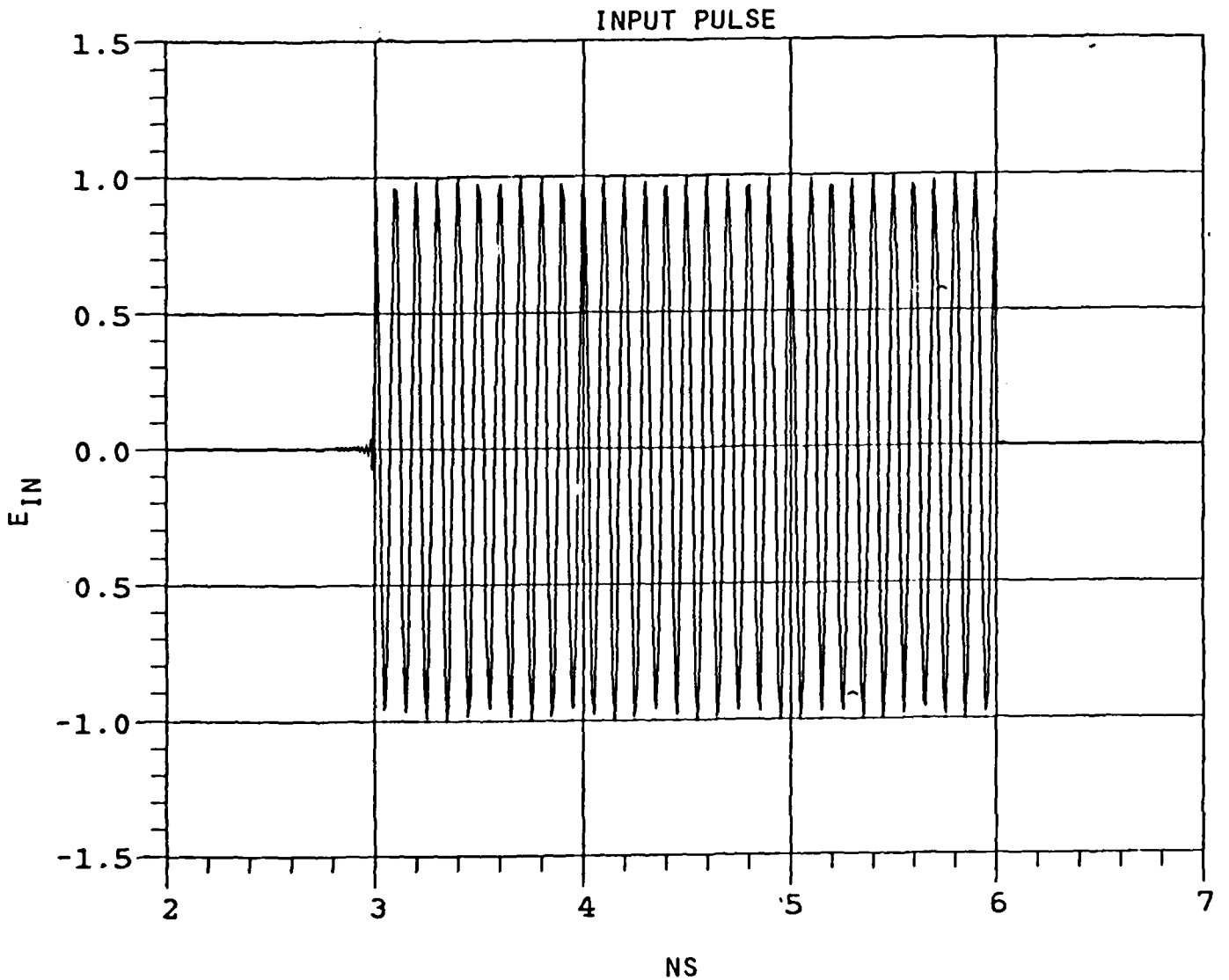
INPUT PULSE
1.5
1.0
0.5
0.0
0.5
-1.0
-1.5
E_{IN}
2
3
4
5
6
7
NS

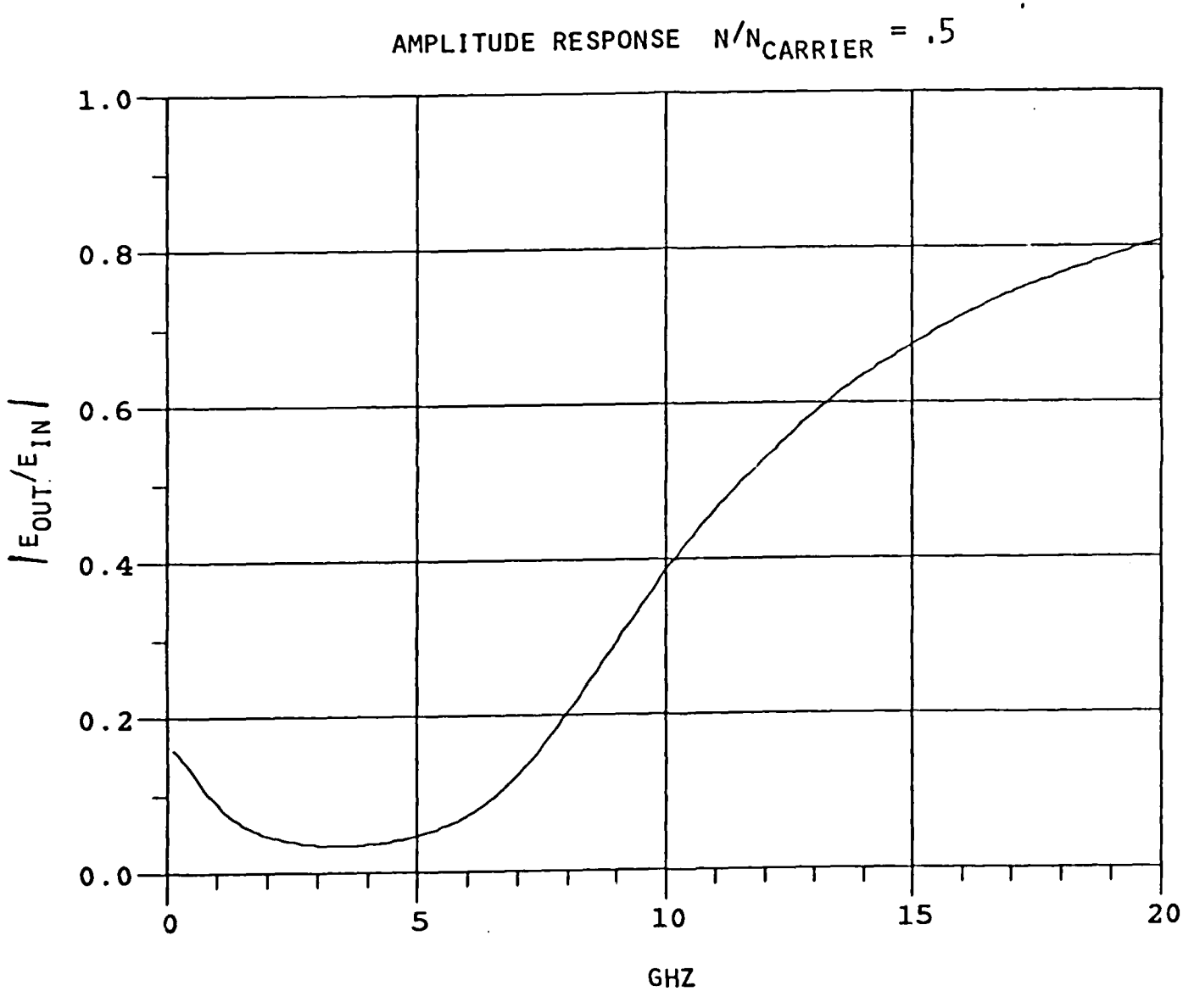
AMPLITUDE RESPONSE N/N CARRIER = .5
1.0
0.8
0.6
0.4
0.2
0.0
|EOUT/EIN|
0
5
10
15
20
GHZ

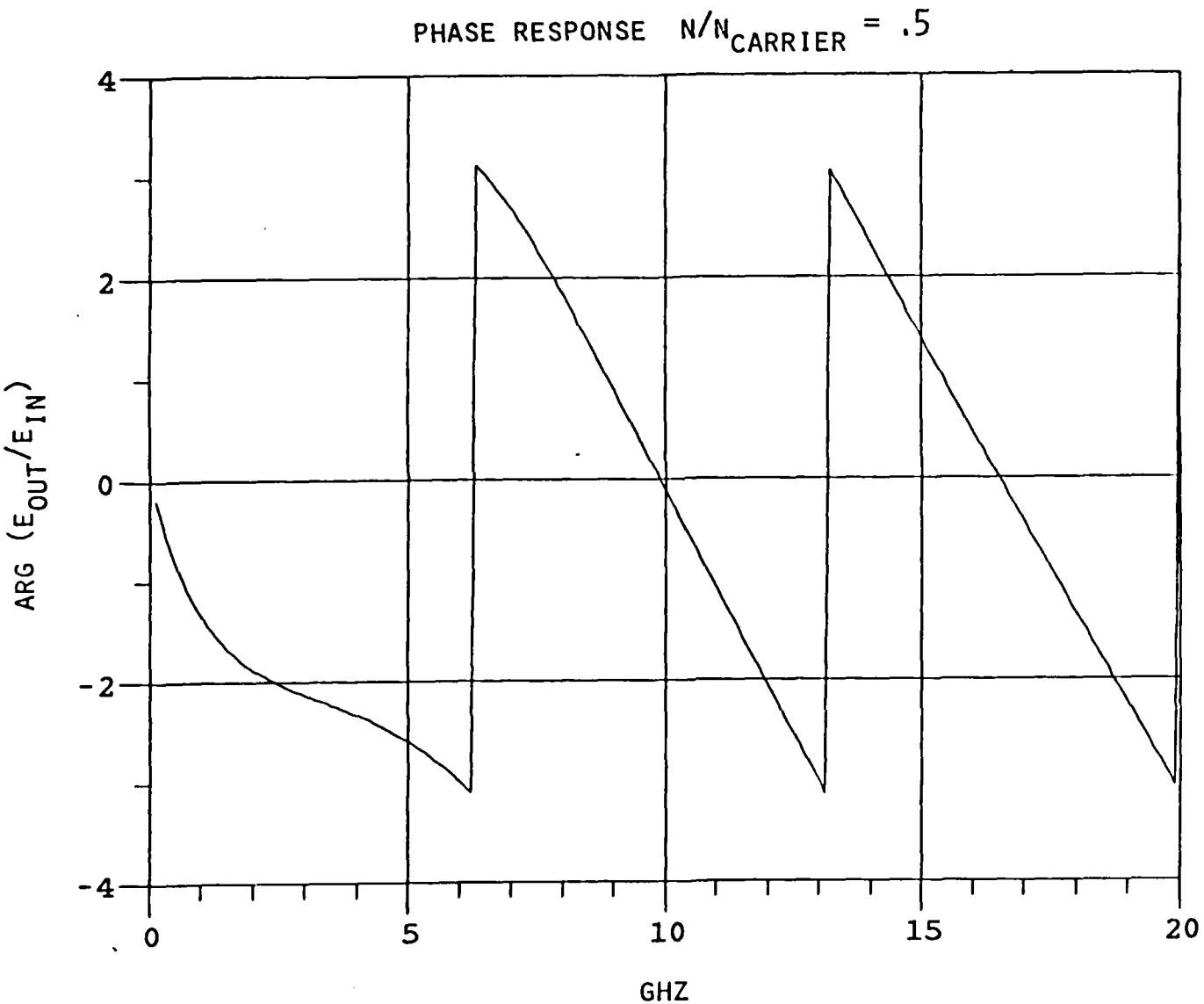
PHASE RESPONSE N/N$_{CARRIER}$ = .5
ARG (E$_{OUT}$/E$_{IN}$)
4
2
0
-2
-4
0
5
10
15
20
GHZ

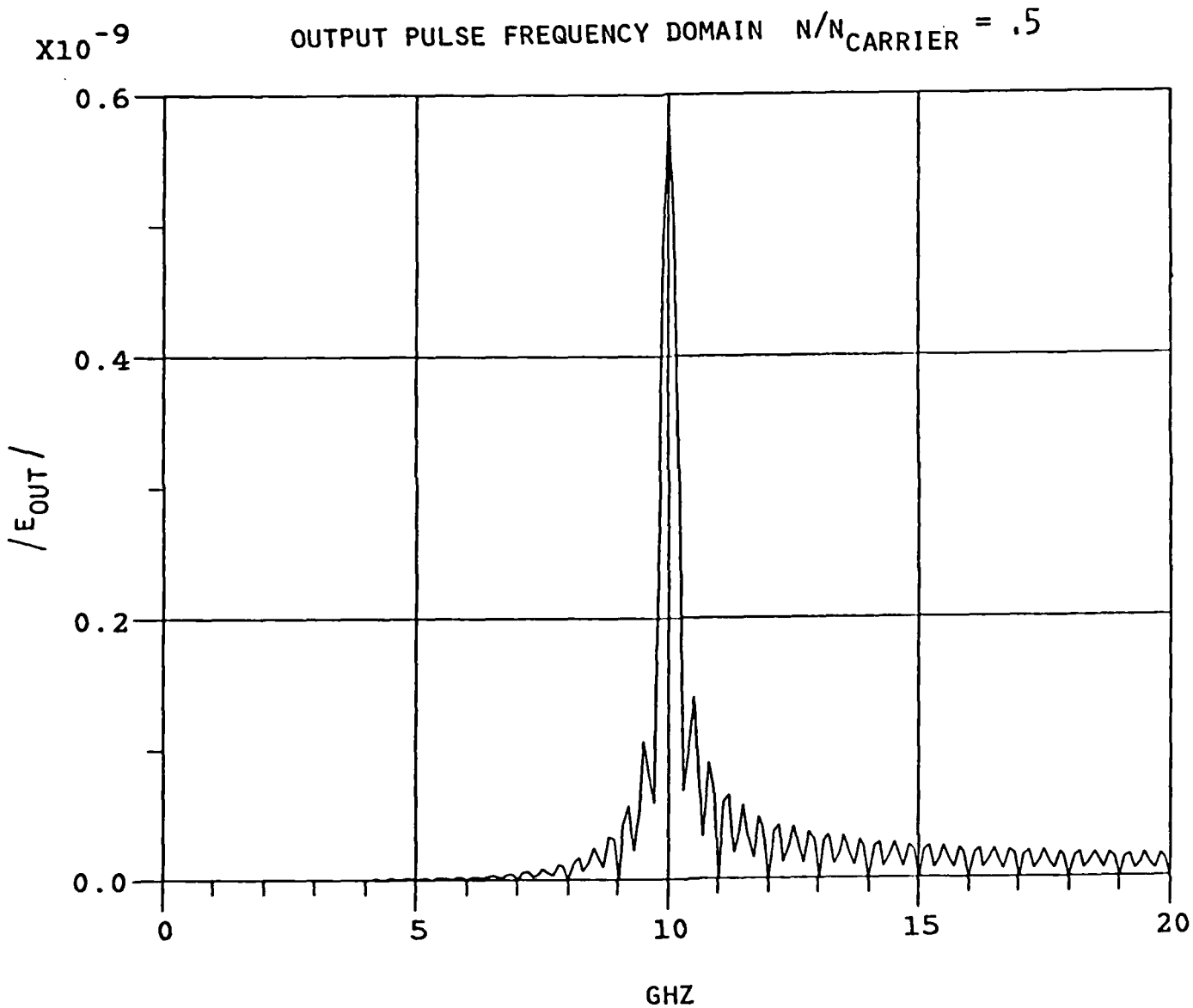
X10^{-9}
OUTPUT PULSE FREQUENCY DOMAIN $N/N_{CARRIER}$ = .5
0.6
0.4
0.2
0.0
$/E_{OUT}/$
0
5
10
15
20
GHZ

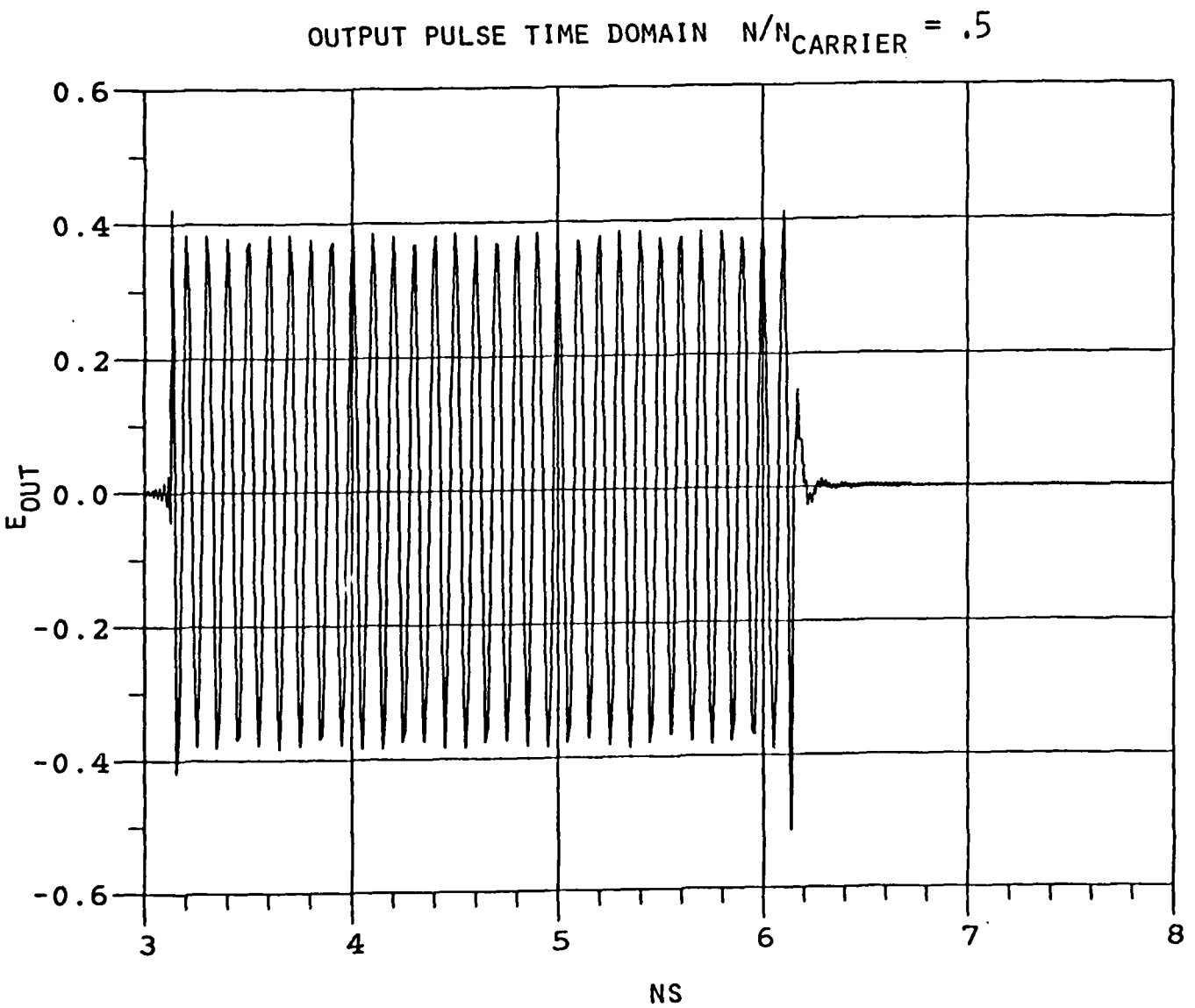
OUTPUT PULSE TIME DOMAIN N/N CARRIER = .5
0.6
0.4
0.2
0.0
-0.2
-0.4
-0.6
E OUT
3
4
5
6
7
8
NS

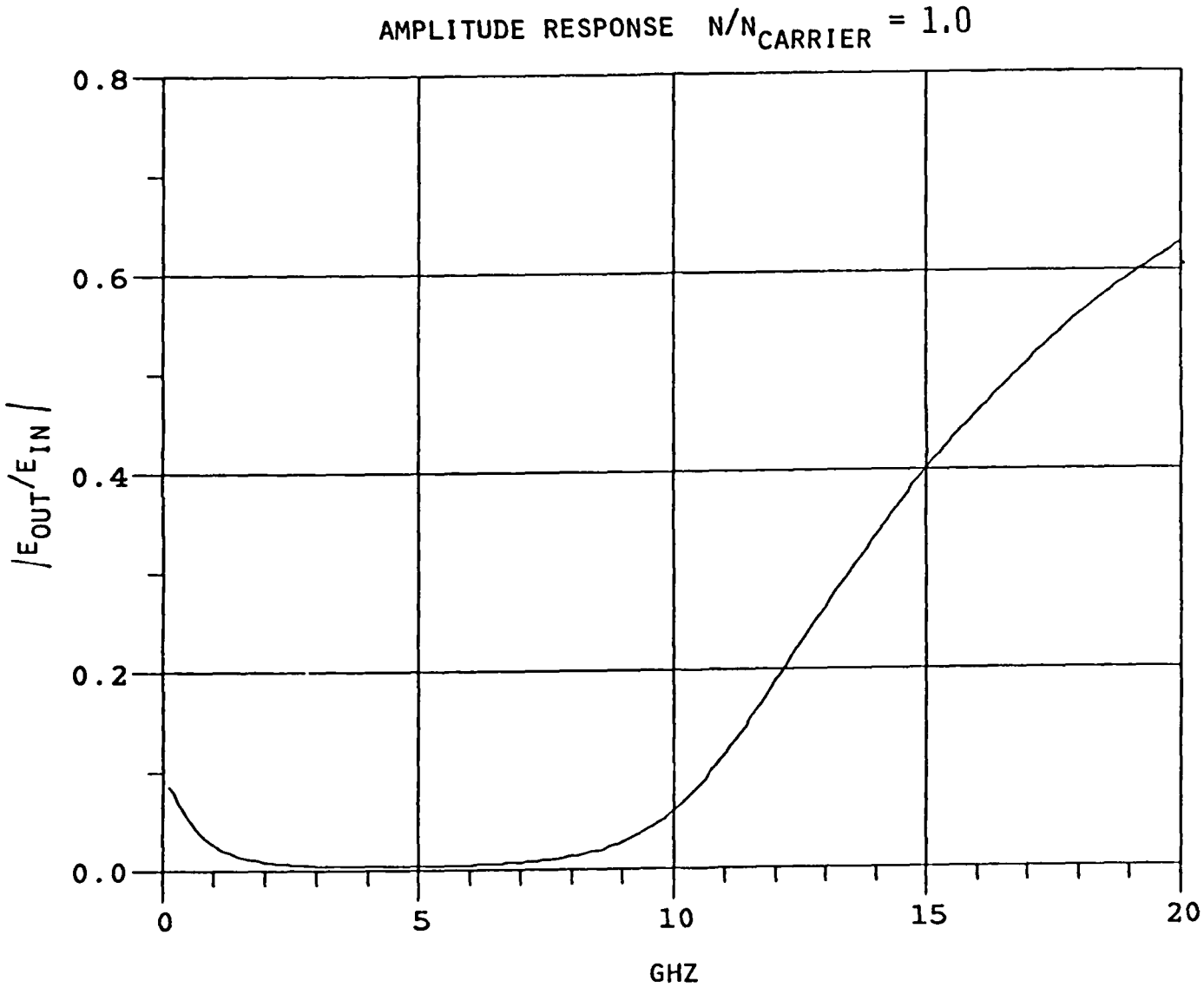
AMPLITUDE RESPONSE N/N CARRIER = 1.0
0.8
0.6
0.4
0.2
0.0
/E OUT /E IN /
0
5
10
15
20
GHZ

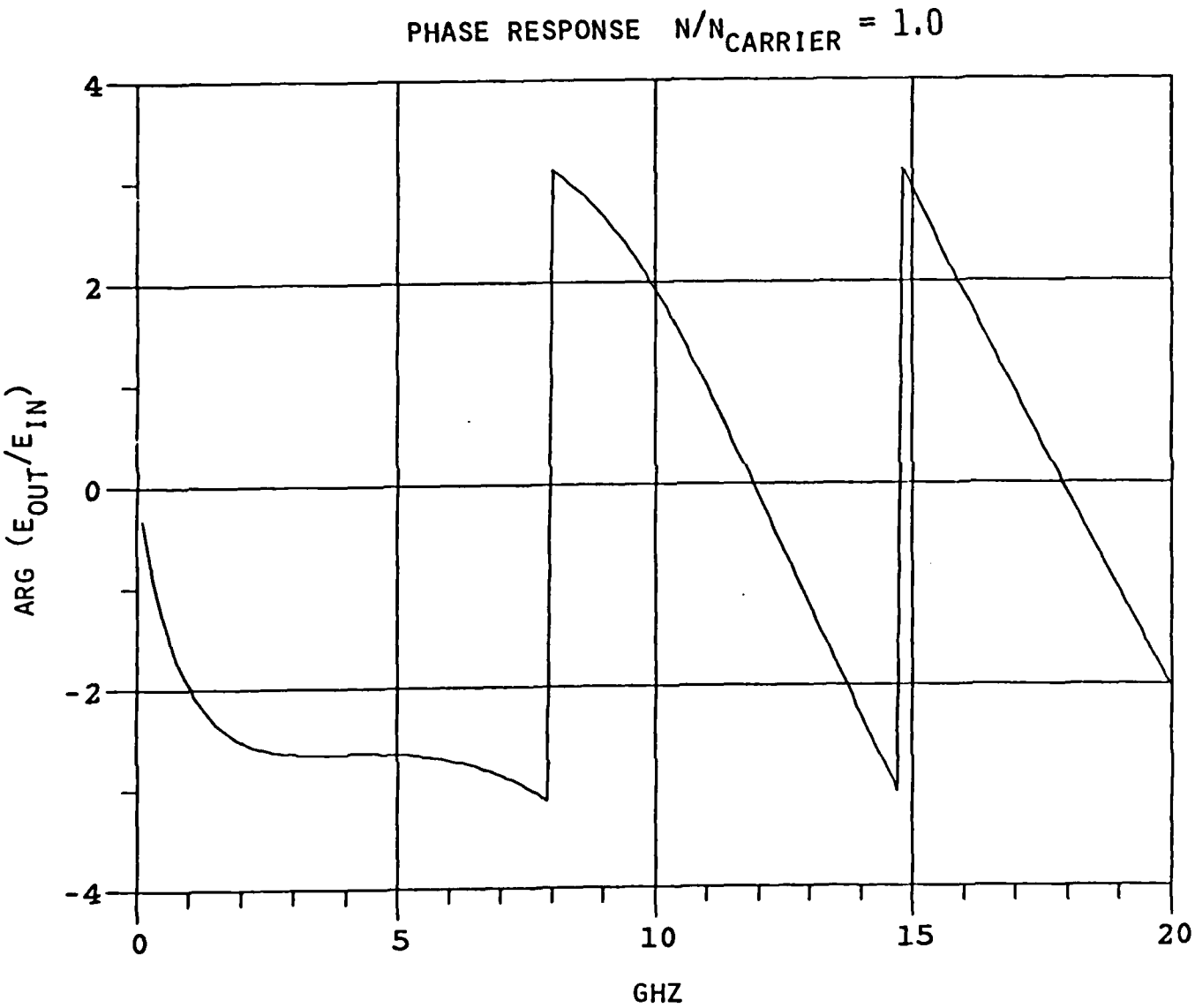
PHASE RESPONSE N/N$_{CARRIER}$ = 1.0
ARG (E$_{OUT}$/E$_{IN}$)
4
2
0
-2
-4
0
5
10
15
20
GHZ

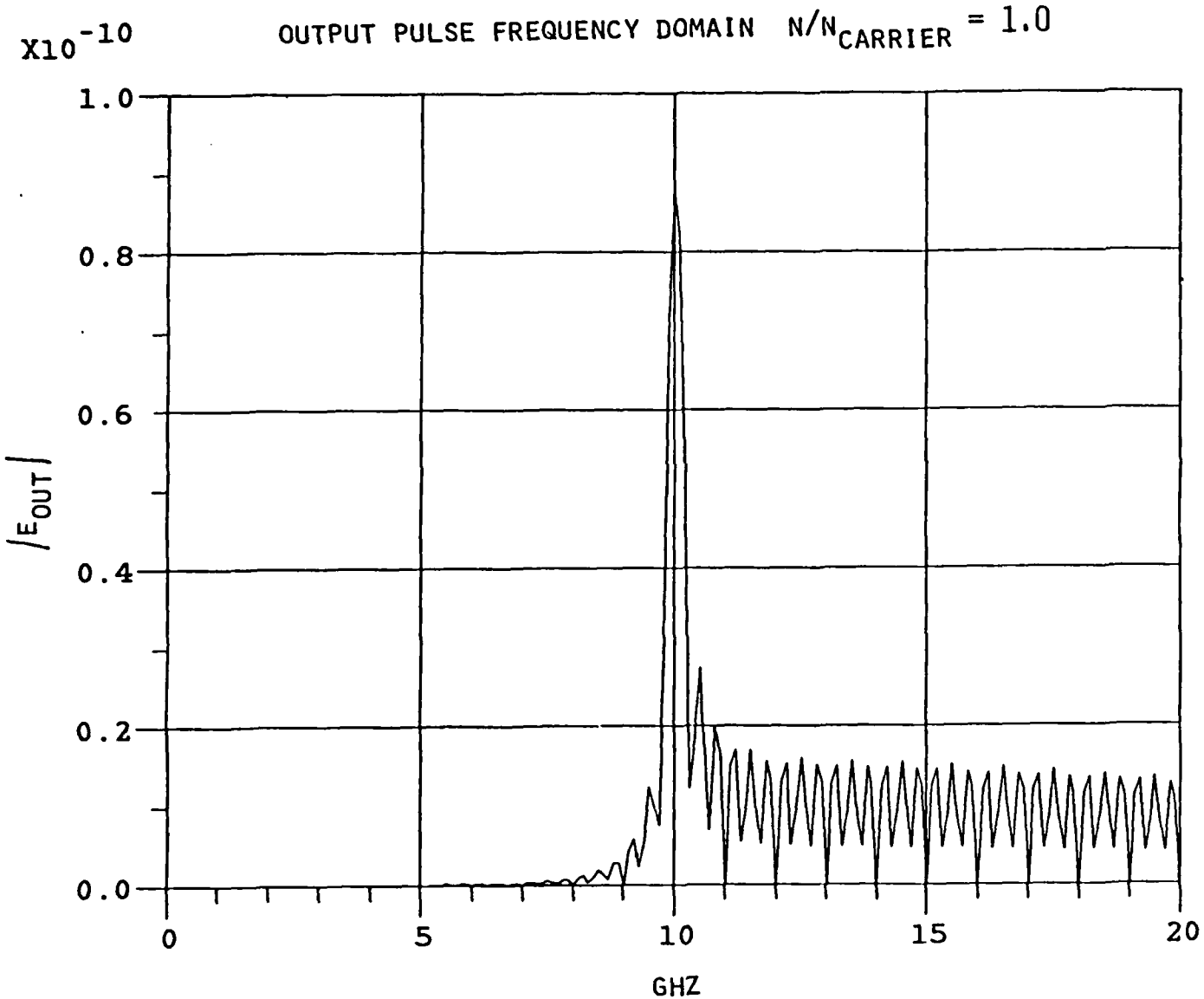
X10-10
OUTPUT PULSE FREQUENCY DOMAIN N/N CARRIER = 1.0
1.0
0.8
0.6
0.4
0.2
0.0
/EOUT/
0
5
10
15
20
GHZ

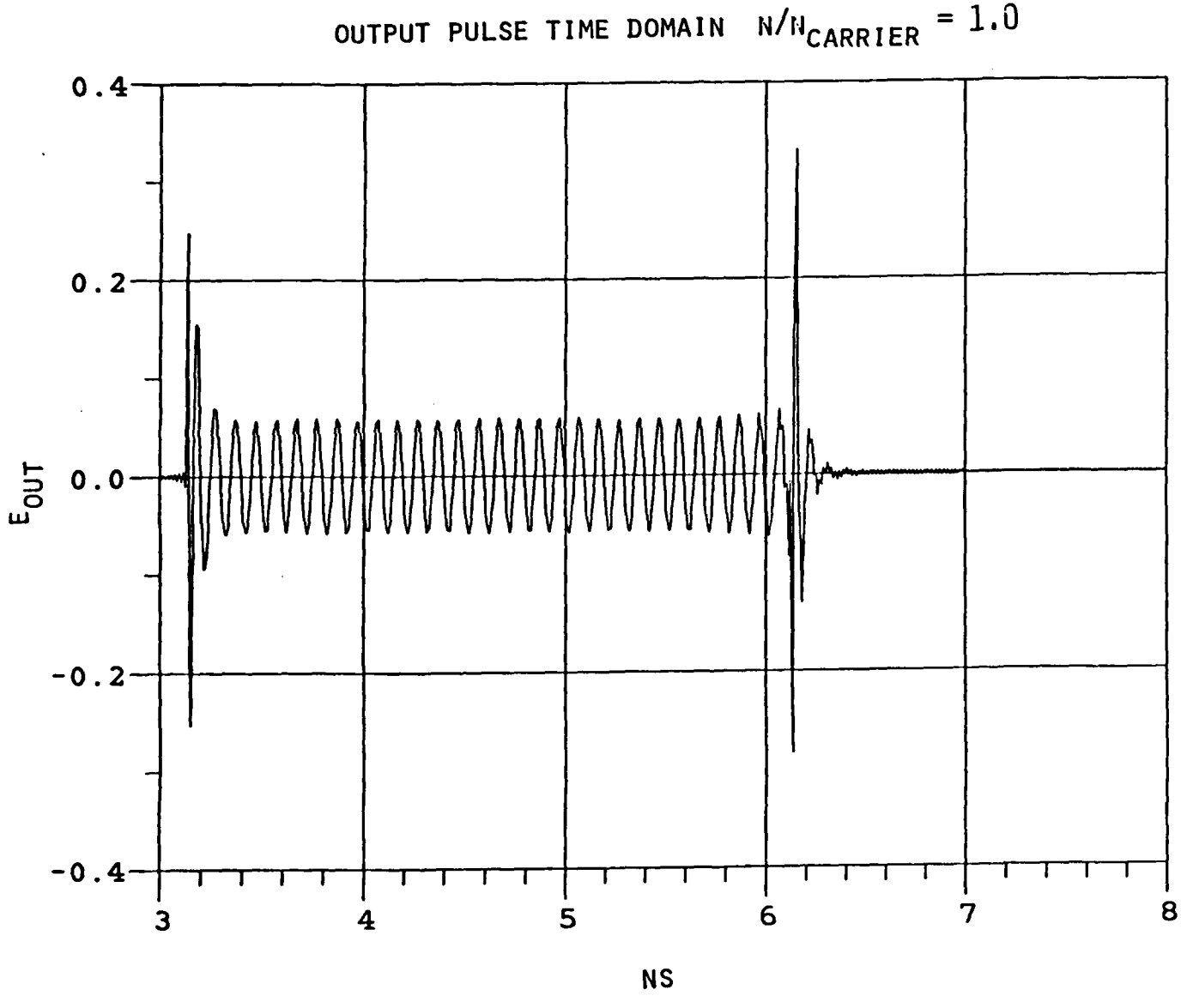
OUTPUT PULSE TIME DOMAIN N/N$_{CARRIER}$ = 1.0
0.4
0.2
0.0
-0.2
-0.4
E$_{OUT}$
3
4
5
6
7
8
NS

Medium Ionization Rate Model for Microwave Propagation through Plasma

In the low ionization rate model we assumed that the ionization rate $\nu_i \ll 1/\tau_{\text{em}}$ where τ_{em} is the electromagnetic response time of the system under consideration. In the medium ionization rate model we remove this restriction and require only that $\nu_i \ll \omega_c$. The geometrical optics method[2] permits solution of the wave amplitude in a time-varying inhomogeneous plasma. This method converges fastest as $\lambda \to 0$. In a static homogeneous collisionless plasma where $\omega_p \approx \omega_c$ (at critical density) $\lambda \to \infty$ and geometrical optics breaks down. Thus another method is needed.

Motivation for Power Series Method

In a static collisionless 1-dimensional plasma the wave equation

$$\frac{\partial^2 E}{\partial z^2} = \frac{1}{c^2}\frac{\partial^2 E}{\partial t^2} + \frac{\omega_p^2}{c^2}E$$

becomes in a critical density region

$$\frac{\partial^2 E}{\partial z^2} \approx 0$$

This suggests a perturbation expansion about the critical density

$$E = E_0 + E_1 + E_2 + \cdots$$

where

$$\frac{\partial^2 E_0}{\partial z^2} = 0$$

and

$$E_0(z,t) = A(t)z + B(t)$$

Consideration of the first order equation

$$\frac{\partial^2 E_1}{\partial z^2} = \frac{1}{c^2}\frac{\partial^2 E_0}{\partial t^2} + \frac{\omega_p^2}{c^2}E_0$$

shows us that to first order the solution for E is a cubic in z with coefficients that are functions of t. To second order the solution for E is a fifth degree polynomial in z with coefficients that are functions of t. Thus expanding to all orders we have a solution for E which is a power series in z with coefficients that are functions of t. Convergence is expected to be best in regions where $\omega_p \approx \omega_c$, i.e. the region where geometrical optics fails.

[2]I.B. Bernstein, Phys. Fluids 18, 320 (1975).

Propagation of Normal Incident Plane Wave

Onto Time Varying Plasma Half-Space

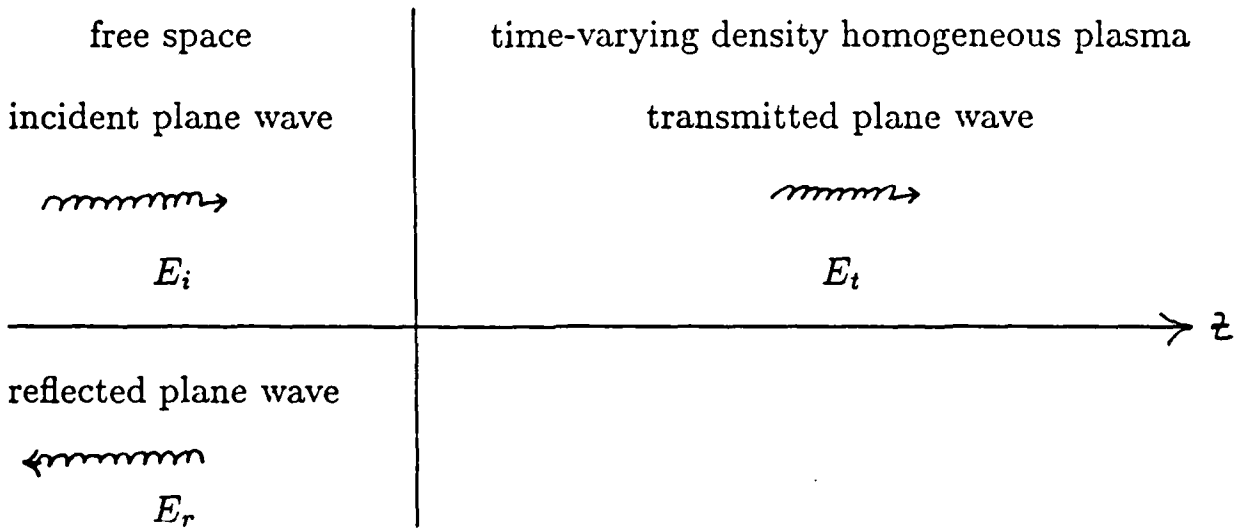

Wave equation

$$\frac{\partial^2 E}{\partial z^2} - \frac{1}{c^2}\frac{\partial^2 E}{\partial t^2} = \frac{\omega_p^2}{c^2}\frac{m}{q}\frac{\partial v}{\partial t}$$

Momentum balance

$$\frac{m}{q}\frac{\partial v}{\partial t} = E - \nu_c \frac{m}{q} v$$

Introduce power series expansions for E and $\frac{m}{q}v$

$$E = \sum_{n=0}^{\infty} a_n(t) z^n \qquad z > 0$$

$$\frac{m}{q} v = \sum_{n=0}^{\infty} b_n(t) z^n \qquad z > 0$$

plugging into wave and momentum balance equations and equating like powers of z gives us a pair of recursion relations for the $a_n(t)$ and $b_n(t)$

$$a_{n+2}(t)(n+1)(n+2) = \frac{1}{c^2}\frac{d^2 a_n}{dt^2} + \frac{\omega_p^2}{c^2}(a_n - \nu_c b_n)$$

$$\frac{db_n}{dt} = a_n - \nu_c b_n$$

By truncating the series after $N+1$ terms where N is the degree of the resulting polynomial a set of $2(N+1)$ coupled second order O.D.E.'s result. These are easily solved numerically by a Runge-Kutta code provided suitable initial conditions $a_n(0)$,$a_n'(0)$,$b_n(0)$,$b_n'(0)$ are found. An exponentially increasing density is of interest:

$$n_e(z,t) = n_e(0)\theta(z)\exp\left(\nu_i t\,\theta(t)\right)$$

where the θ function is defined

$$\theta(\eta) = 1 \qquad \eta > 0$$

$$\theta(\eta) = 0 \qquad \eta < 0$$

For this case the $a_n(0)$ are easily found since the plasma is in steady state condition for $t < 0$.

$$E(z, t=0) = \sum_{n=0}^{\infty} a_n(0) z^n = E_t e^{-ikz} = \sum_{n=0}^{\infty} E_t \frac{(-ikz)^n}{n!}$$

$$a_n(0) = E_t \frac{(-ik)^n}{n!}$$

where

$$E_t = E_i \frac{2k_0}{k + k_0}$$

and

$$k = \sqrt{\frac{\omega_c^2}{c^2} - \frac{\omega_p^2}{c^2} \frac{1}{1 - i\nu_c/\omega_c}}$$

Find $b_n(0)$

$$\frac{m}{q} v(z, t = 0) = \sum_{n=0}^{\infty} b_n(0) z^n$$

In steady state ($t < 0$)

$$\frac{i\omega_c m}{q} v = E - \frac{\nu_c m}{q} v$$

$$(i\omega_c + \nu_c) \frac{m}{q} v = E$$

Therefore

$$\sum_{n=0}^{\infty} b_n(0) z^n = \sum_{n=0}^{\infty} \frac{a_n(0)}{i\omega_c + \nu_c} z^n$$

$$b_n(0) = \frac{a_n(0)}{i\omega_c + \nu_c}$$

The $b_n'(0)$ are given by

$$b_n'(0) = a_n(0) - \nu_c b_n(0)$$

Find the $a_n'(0)$ from the following boundary conditions for the electric field

$$\frac{\partial E}{\partial t}\Big)_{z=0-} = \frac{\partial E}{\partial t}\Big)_{z=0+}$$

$$\frac{\partial E}{\partial z}\Big)_{z=0-} = \frac{\partial E}{\partial z}\Big)_{z=0+}$$

Write the electric field for $z = 0^-$ as the sum of an incident term and a reflected term F_r

$$E(z,t) = E_i e^{-i\frac{\omega_c}{c}z} e^{i\omega_c t} + F_r(z+ct) \qquad z < 0$$

$$\frac{\partial E}{\partial z}\Big)_{z=0^-} = -i\frac{\omega_c}{c}E_i e^{i\omega_c t} + F_r'(ct)$$

$$\frac{\partial E}{\partial t}\Big)_{z=0^-} = i\omega_c E_i e^{i\omega_c t} + cF_r'(ct)$$

combining and using the boundary condition produces

$$\frac{\partial E}{\partial t}\Big)_{z=0+} - c\frac{\partial E}{\partial z}\Big)_{z=0+} = 2i\omega_c E_i e^{i\omega_c t}$$

Introduce the power series

$$E = \sum_{n=0}^{\infty} a_n(t) z^n \qquad z > 0$$

and we have

$$a_0'(t) - ca_1(t) = 2i\omega_c E_i e^{i\omega_c t} \qquad (*)$$

This relationship produces $a_0'(0)$ immediately from $a_1(0)$

$$a_0'(0) = 2i\omega_c E_i + ca_1(0)$$

repeated differentiation of equation * and liberal use of the recursion relations for the a_n and b_n permit finding all of the $a_n'(0)$. This repeated differentiation process also allows us to find the $a_n''(0)$, $a_n'''(0)$ etc.

The above method finds the $a_n(0)$,$b_n(0)$,$a'_n(0)$,$b'_n(0)$ which permits a Runge-Kutta code to find the electric field as a function of z for $z > 0$ at any time step. Plots shown of E versus z are made from this method.

Alternatively if we wish only to find the electric field for $z = 0^+$ (and from the boundary conditions the electric field for $z = 0^-$) as a function of time we may use the derivatives of $a_0(t)$

$$E(z = 0^+, t) = \sum_{i=0}^{\infty} \frac{a_0^{(i)} t^i}{i!}$$

Plots shown of E versus t are made from this method.

Parameters Used in Plotting

E versus z plot

1. $n/n_c)_{t=0} = .5$
2. $\nu_i = .1\omega_c$
3. $\nu_c = 0$
4. Runge-Kutta time step $= .5/\omega_c$
5. Output is after 1 time step $\rightarrow t = .5/\omega_c$
6. $n/n_c = n/n_c)_{t=0} \exp(\nu_i t) = .5 \exp(.05) = .526$
7. Degree of approximating polynomial = 20.

E versus t plot

1. $n/n_c)_{t=0} = .5$
2. $\nu_i = .1\omega_c$
3. $\nu_c = 0$
4. Curve labeled actual is a plot of $a_0(t)$ with 32 terms kept in the taylor series.
5. Curve labeled static is a plot of

$$E_{t\,\mathrm{static}} = \mathrm{Re}\left(E_i e^{i\omega_c t} \frac{2k_0}{k_0 + k(t)} \right)$$

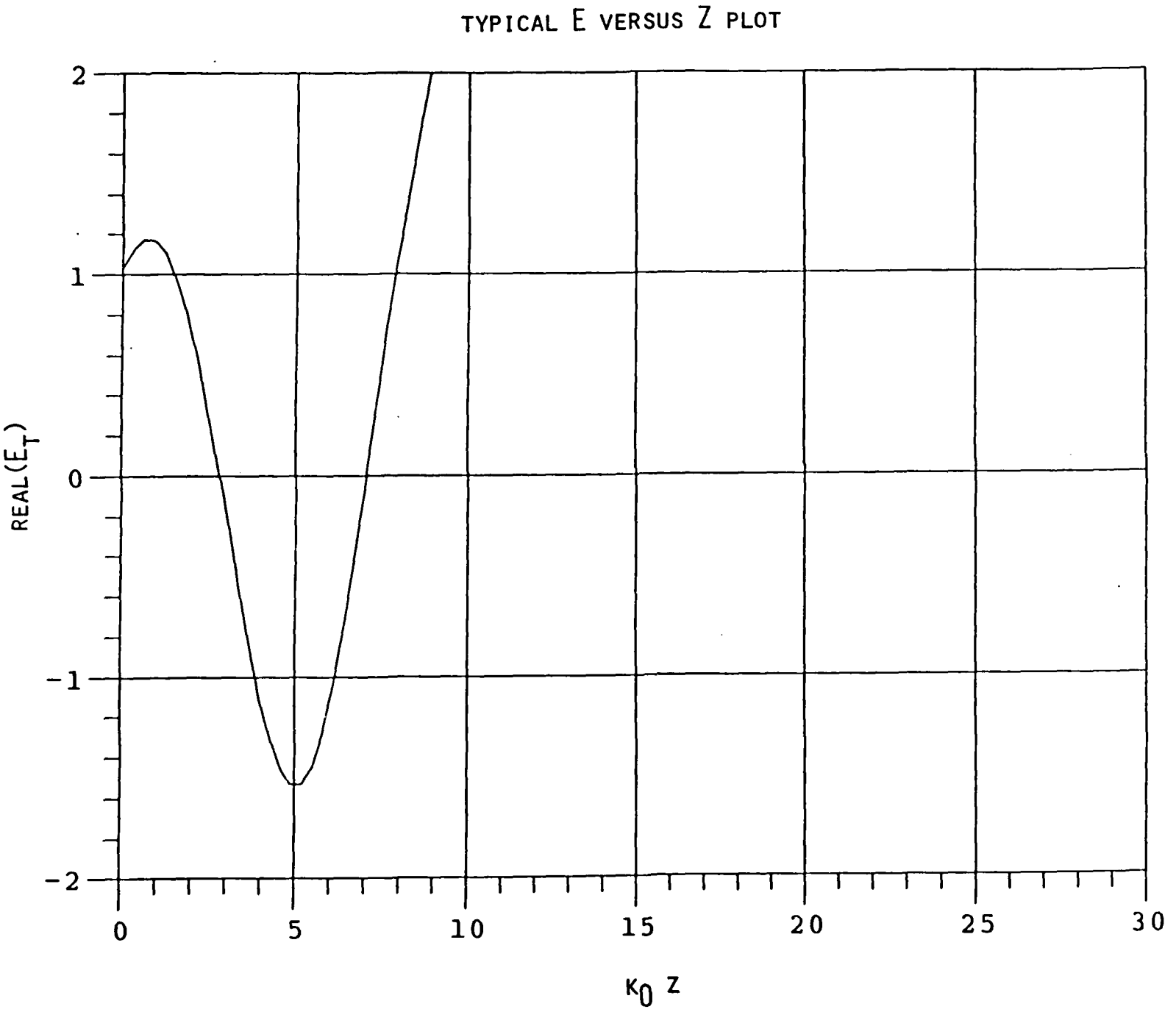
TYPICAL E VERSUS Z PLOT
2
1
0
-1
-2
REAL(E_T)
0
5
10
15
20
25
30
K_0 Z

TYPICAL E VERSUS T PLOT

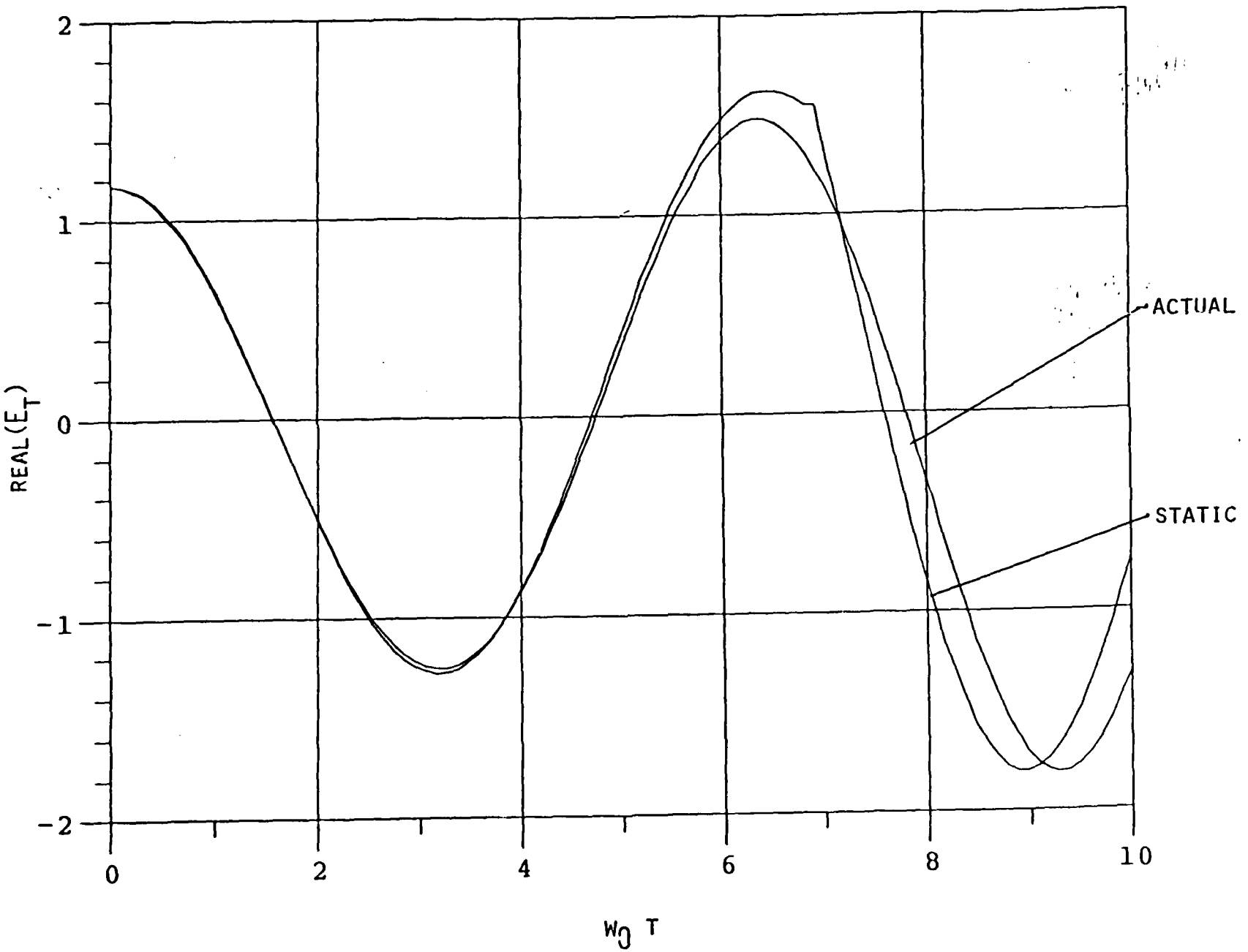

Future Work

1. Study convergence properti·s of power series solution for the electric field in a time-varying plasma.
2. Investigate the physics of propagation of RF through a time-varying plasma which has density increasing beyond critial density.
3. Consider alternative expansions for the electric field in a time-varying plasma and their convergence properties.
4. Impose self-consistency on a plasma density profile with an ionizing propagating electric field for a plasma half-space and other geometries.
5. Study high ionization rate breakdown where the ionization rate is of the order of the RF carrier frequency.

Shielded-Source, Short-Pulse Microwave Propagation Experiments

W. W. Destler, Z. Segalov, and J. Rodgers
Electrical Engineering Department
University of Maryland, College Park MD 20742

Abstract

The propagation of short-pulse, high power microwaves through a neutral gas has been studied and breakdown limits determined in an experimental configuration in which the neutral gas test cell was carefully shielded from x-rays emanating from the high power microwave tube. In this manner the possible x-ray generation of free electrons in the test cell was minimized. Results are compared with previous experiments in which the test cell was not shielded from the source.

I. Introduction

Renewed interest in the propagation of high power microwave pulses in the atmosphere[1-6] has resulted from the availability of very high power microwave sources with pulse durations in the range 2-1000 ns.[7] It has been suggested that extremely high levels of microwave power can be propagated in the atmosphere if the microwave pulse duration is significantly shorter than the time required to build up electron densities sufficient to absorb or reflect significant microwave energy.

In previous work[8], our group has reported studies of the propagation of high power (50-300 kW/cm^2), short-pulse (2-35 ns) microwaves through an air filled test cell. In these experiments, microwaves from a high power Large Orbit Gyrotron were focused into a test cell using a large diameter parabolic reflector, and microwave breakdown thresholds were determined over a wide range of test cell pressure and microwave power density and pulse duration. These free space microwave breakdown thresholds were found to be comparable to previous data obtained on breakdown limits in waveguides, and shorter pulse durations did allow higher microwave power densities to propagate without breakdown, as expected.

It has been suggested[9], however, that x-radiation produced by the energetic electrons in the Large Orbit Gyrotron could be responsible for generating a number of free electrons in the test cell, and that breakdown might therefore have been observed at artificially low values of microwave power density. In the experiments reported herein, the test cell was carefully screened from the Large Orbit Gyrotron x-radiation by a concrete and lead shield wall, and breakdown limits were determined in the manner reported previously. Thus a ready comparison between breakdown limits with and without source x-ray shielding is now possible.

In this paper, related theoretical considerations are discussed in section II. The experiments conducted are detailed in section III, and results are compared with previously obtained unshielded source breakdown limits in section IV.

II. Theoretical Discussion

The theory of microwave breakdown of a neutral media is treated extensively in

early work by MacDonald[10]. This treatment assumes that breakdown occurs when the electric field of the microwaves accelerates any free electrons in the media to energies sufficient to cause ionizing collisions with neutrals. The resulting production of additional electrons drives an avalanche process that results in a rapid rise in the plasma density and eventual microwave absorption or reflection. The continuity equation for electrons in the media is written

$$\frac{\partial n}{\partial t} = \nu_i n - \nu_a n + \nabla^2(Dn) \tag{1}$$

where n is the electron density, ν_i is the ionization rate, ν_a is the attachment rate, and D is the electron diffusion coefficient. Usually the diffusion term is approximated as $\nabla^2(Dn) \cong n(-D/\Lambda^2)$, where Λ is the characteristic diffusion length and is dependent upon the particular system geometry. Under this approximation, the continuity equation yields

$$n = n_o e^{(\nu_i - \nu_a - D/\Lambda^2)t} = n_o e^{\nu t} \tag{2}$$

where ν is a net rate for electron production. A reasonable estimate of the time required to reach breakdown is obtained if it is assumed that breakdown occurs when the plasma density reaches the critical plasma density for wave propagation

$$n_p = 10^{13}/\lambda^2 \ (cm^{-3}) \tag{3}$$

The pulse duration τ for breakdown to occur is then given by

$$n_p = n_o e^{\nu t} \tag{4}$$

Although the initial free electron density is not known to any degree of accuracy in most experiments, the exponential nature of the rise in electron density with time tends to minimize the effects of errors in the number assumed for n_o. Nevertheless, this effect can be significant. For 3 cm microwaves, for example, the difference between $n_o = 1$ and $n_o = 1000$ cm^{-3} represents about a 25% change in the breakdown pulse duration assuming other quantities remain fixed. Of course, if a media can be found in which $n_o = 0$, breakdown will not occur for any pulse length unless the wave electric field is large enough to directly strip an electron from a neutral.

III. Experiments

High power microwave pulses used for the propagation experiments were generated by a large-orbit gyrotron operating at 10 GHz, as reported previously[8]. This device produces high power microwave radiation (100-500 MW) by the resonant interaction of a rotating electron beam with the modes of a multiresonator magnetron circuit. The experimental configuration used for the propagation experiments is shown in Fig. 1. Microwaves from the large-orbit gyrotron are reflected 90° by a plane reflector toward a 150 cm diameter parabolic reflector. The parabolic reflector serves to focus the microwaves into the test cell. The test cell, a 30 cm diameter cylindrical acrylic vacuum chamber, is fitted with a high accuracy vacuum gauge and a calibrated leak valve that allowed maintenance of ambient pressures from atmosphere down to 0.1 Torr. Measurements of the microwave power density along the dish axis (Fig. 2) and across a cell diameter (Fig. 3) indicate that a reasonable focus was achieved away from the test cell walls (surface breakdown on the test cell walls must be avoided if true media breakdown limits are to be established).

The shield wall between the large-orbit gyrotron and the test cell was constructed of 20 cm thick high-density concrete block augmented by 1 cm of lead sheet. Measurements of the x-radiation observed at the test cell indicate that the shield wall reduced x-radiation by more than two orders of magnitude, with typical TLD detector dosage recordings of 50 mR/shot observed without the shield wall and 0.5 MR/shot after the shield wall was constructed. Because of reflections, it was not possible to completely eliminate all x-radiation from the test cell area.

Open ended X-Band (8-12 GHz) waveguide sections were used to detect the microwave signals before and after the focal point in the test cell, as shown in Fig. 4. Microwave signals were passed through calibrated attenuators to calibrated detectors selected for their measured transient response time (rise time $\sim$ 1 ns). Detector signals were fed directly into Tektronix 7104 oscilloscopes.

In this work, breakdown of the media was said to occur if either visible light from ionization processes was observed in time-integrated photographs of the test cell or if significant shortening of the post-focus microwave pulse was observed due

to reflection and/or absorption of the microwaves by the breakdown plasma. The criteria for pulse shortening to indicate breakdown was if the transmitted pulse duration was 80% or less of the incident pulse duration. Microwave power density was varied over the range 50-300 kW/cm^3 and pulse duration was varied over the range 3-20 ns. Data for the experiments are plotted in the familiar E/p vs pτ format in Fig. 5.

IV. Conclusions

From the data shown in Fig. 4 and previously reported data[8], it appears that a significant reduction in background radiation does increase the wave electric field required for breakdown, at least at high (> 1000) and low (< 10) values of pτ. This increase in the breakdown electric field, about a factor of two over the previously reported data, is small but nevertheless large enough to ensure that statistical fluctuations alone cannot account for the increase.

Unfortunately, it is nearly impossible to measure accurately the actual free electron density in the test cell at the time these measurements were made, due primarily to the unavailability of diagnostics sensitive enough to yield quantitative estimates of such low electron densities. Even a theoretical estimate would require a very careful measurement of the x-ray energy spectrum and information on x-ray induced ionization cross sections over the entire spectrum. Nevertheless, the data, and the theoretical discussion in section II, suggests that breakdown thresholds as reported here and in the previous report[8] are reasonably reliable as long as at least a few free electrons are present in the media. Natural radioactivity and cosmic radiation are probably sufficient to ensure that this is the case.

Acknowledgements

It is a pleasure to acknowledge the technical assistance of J. Pyle and useful discussions with Dr. C. D. Striffler and H. Rappaport. We are also grateful for the loan of several pieces of experimental equipment from Harry Diamond Laboratories. This work was supported by the Air Force Office of Scientific Research.

References

1. W. Woo and J. S. DeGroot, Phys. Fluids 27, 475 (1984).

2. J. H. Yee, R. A. Alvarez, D. J. Mayhall, D. P. Byrne, and J. Degroot, Phys. Fluids 29, 1238 (1986).

3. A. W. Ali and T. Coffey, Naval Research Laboratory Memorandum Report No. 4320, 1980 (unpublished).

4. W. M. Bollen, C. L. Yee, A. W. Ali, M. J. Nagurney, and M. E. Read, J. Appl. Phys. 54, 101 (1983).

5. S. M. Flatte, Proc. IEEE 71, 1267 (1983).

6. V. L. Granatstein and I. Alexeff, Eds, High Power Microwave Sources, (Artech House, MA 1987), and references therein.

7. C. A. Sullivan, W. W. Destler, J. Rodgers, and Z. Segalov, J. Appl. Phys. 63, 5228 (1988).

8. W. M. Bollen, private communication

9. A. D. MacDonald, Microwave Breakdown in Gases (Wiley, NY, 1966), p. 160.

Figure Captions

1. Experimental configuration used for shielded-source microwave propagation experiments.

2. Schematic of microwave diagnostic setup used in the propagation experiments.

3. Microwave power density vs distance along the axis of the parabolic reflector.

4. Microwave power density vs distance across a diameter of the test cell.

5. Microwave propagation data.

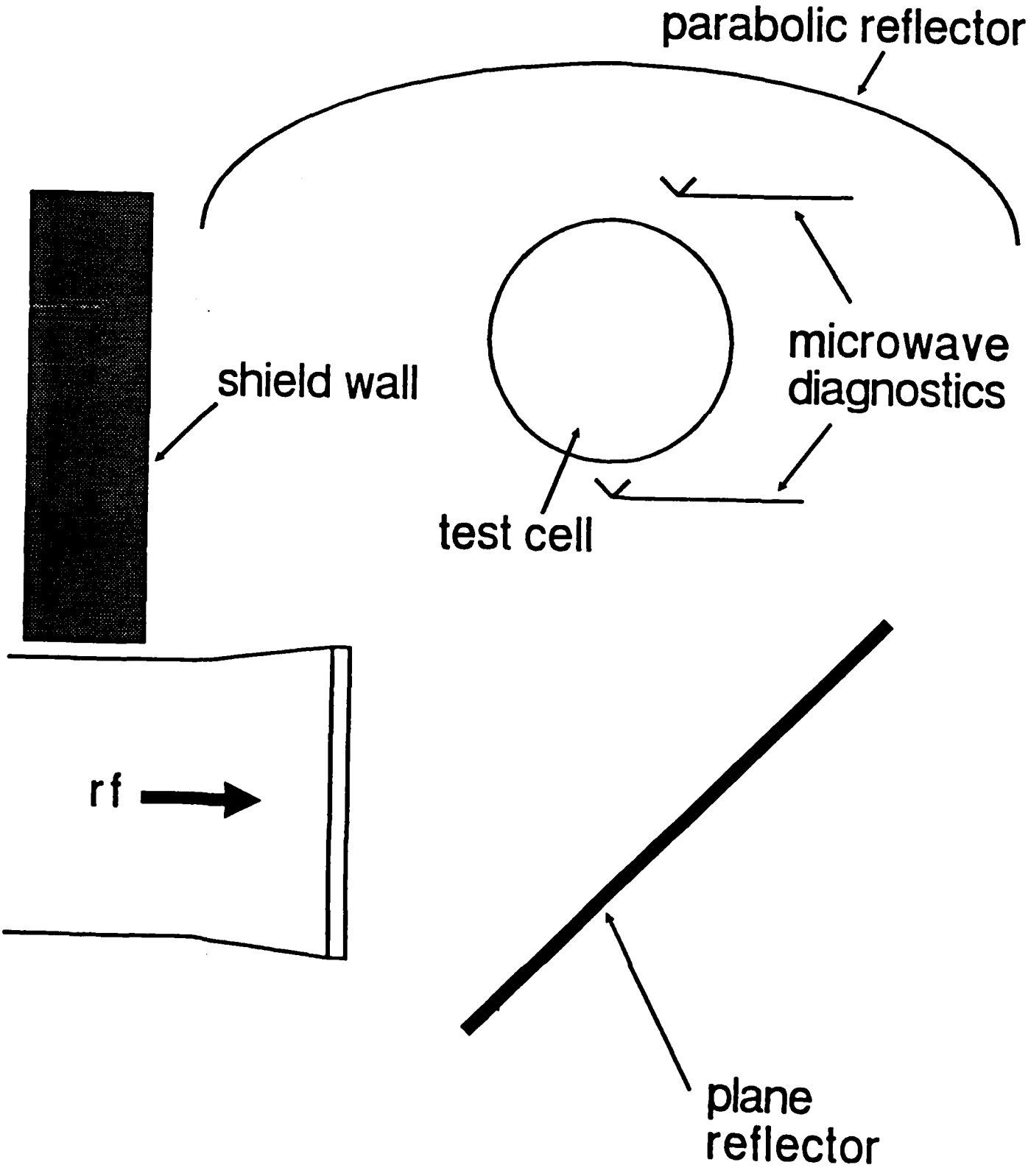
parabolic reflector
shield wall
microwave
diagnostics
test cell
rf
plane
reflector

FIGURE 1

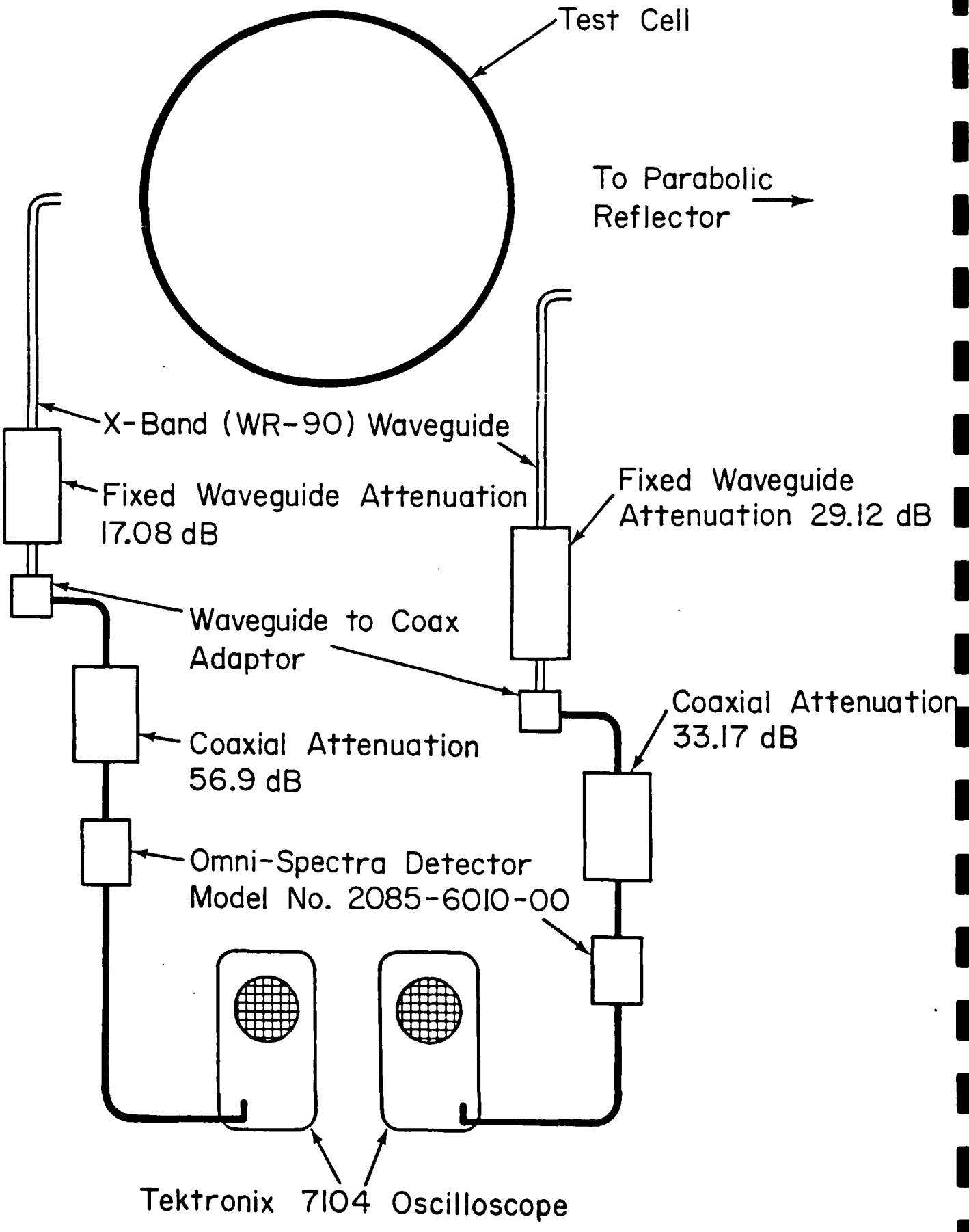
Test Cell
To Parabolic Reflector
X-Band (WR-90) Waveguide
Fixed Waveguide Attenuation 17.08 dB
Fixed Waveguide Attenuation 29.12 dB
Waveguide to Coax Adaptor
Coaxial Attenuation 33.17 dB
Coaxial Attenuation 56.9 dB
Omni-Spectra Detector Model No. 2085-6010-00
Tektronix 7104 Oscilloscope

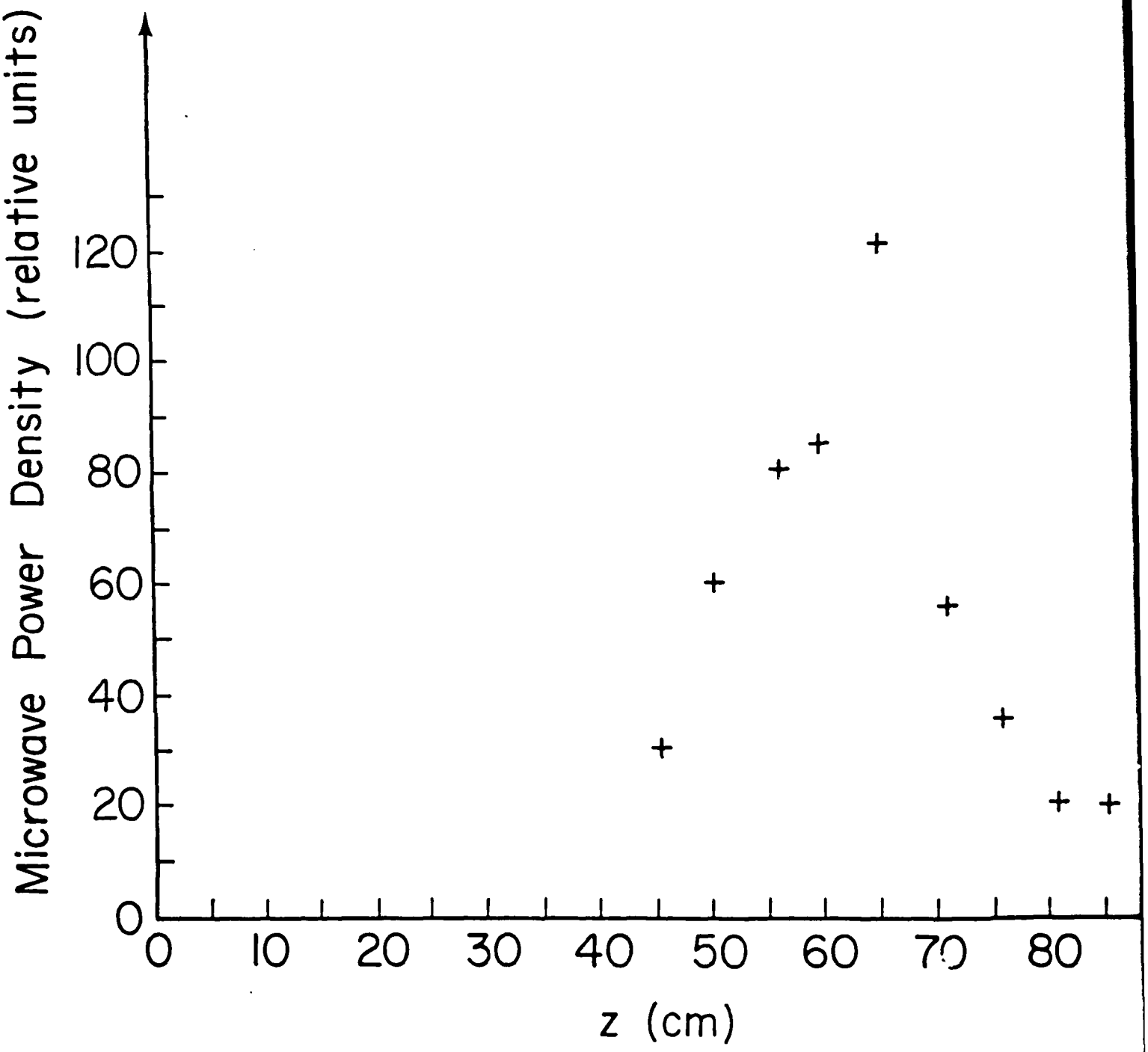
Microwave Power Density (relative units)
120
100
80
60
40
20
0
0
10
20
30
40
50
60
70
80
z (cm)

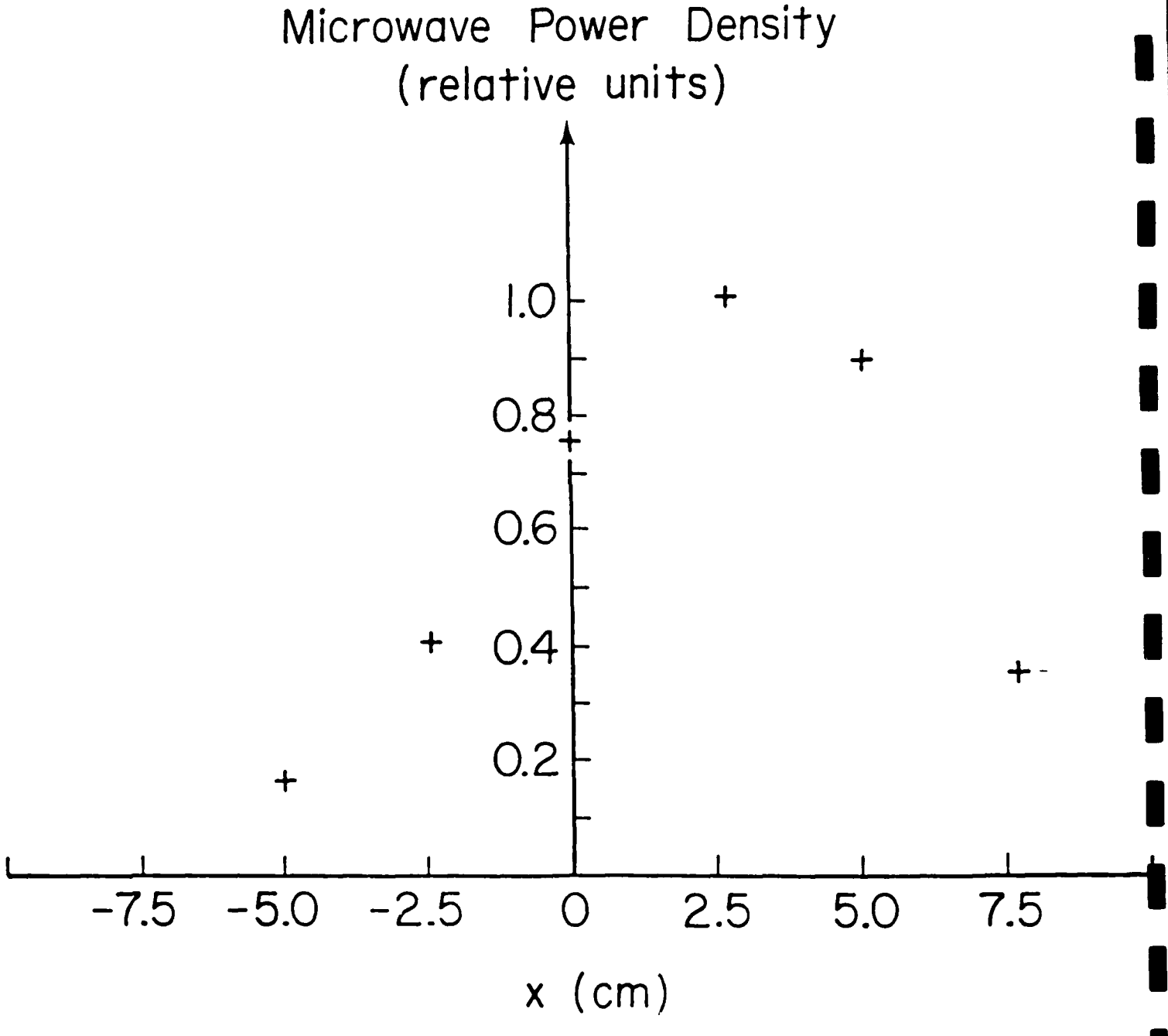
Microwave Power Density
(relative units)
1.0
0.8
0.6
0.4
0.2
-7.5
-5.0
-2.5
0
2.5
5.0
7.5
x (cm)

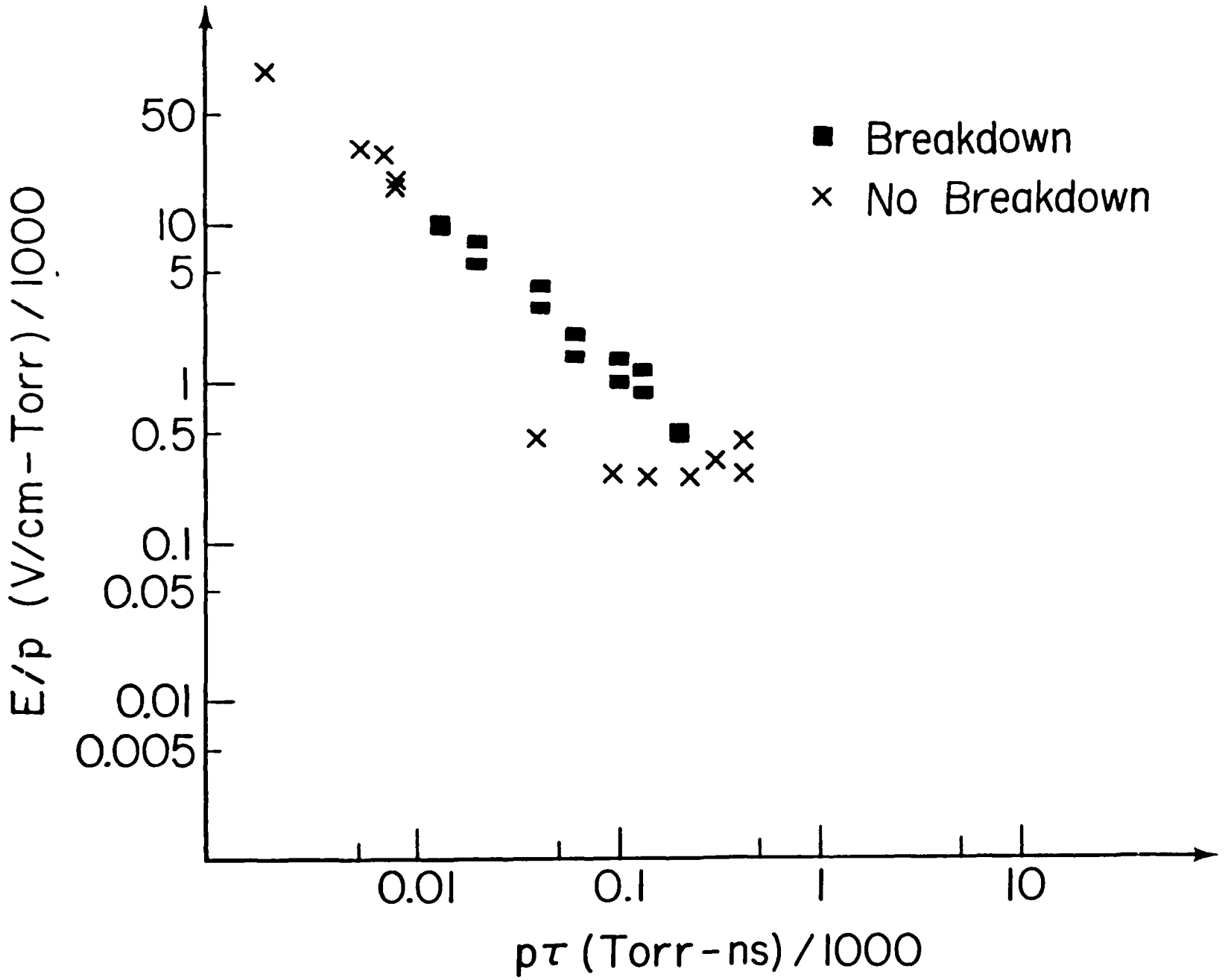
Breakdown
No Breakdown
E/p (V/cm-Torr) / 1000
50
10
5
1
0.5
0.1
0.05
0.01
0.005
0.01
0.1
1
10
pτ (Torr-ns) / 1000

FIGURE 5